Structure, Function, and Inhibition of Protein Depalmitoylases

by

Sang Joon Won

A dissertation submitted in partial fulfillment
of the requirements for the degree of
Doctor of Philosophy
(Chemical Biology)
in the University of Michigan
2018

Doctoral Committee:

Assistant Professor Brent R. Martin, Chair
Professor Philip C. Andrews
Associate Professor Jolanta Grembecka
Professor John J. G. Tesmer

Sang Joon Won

sjwon@umich.edu

ORCID iD: 0000-0002-8148-7652

Dedication

I dedicate this dissertation to all my teachers and mentors.

Acknowledgements

First, I would like to thank my family for their continuous support throughout my journey so far. They are the best mentors who will always listen to me and give honest advice. I would not have arrived in America without their support and trust in my abilities. Thanks to them, I always felt confident in challenging the new chapters in my life so far.

I would like to thank my mentors and teachers at the University of Wisconsin-Madison, who first introduced me to the real science. Professor Michael Cox and Dr. Marielle Gruenig are the people I always admired as scientists and as human being. They became my role models and inspired me to continue my study in graduate school

I also thank Dr. Venki Ramakrishnan and Dr. Alexey Amunts for supervising me at the MRC-Laboratory of Molecular Biology, Cambridge. They are the first ones to introduce me to the structural biology. From my two months of experience, I have learned the true dedication of the top-level scientists.

I would like to thank my committee members Prof. Philip Andrews, Prof. Jolanta Grembecka, and Prof. John Tesmer for their critical feedback and putting me on the right path to graduation. I rotated in Prof. Tesmer's lab and with Dr. Alisa Glukhova's help, I really enjoyed my first lab experience here in Michigan. I have learned a lot from Prof. Tesmer with his ability to provide critical insight into problems.

I would like to thank Prof. Brent Martin for being my mentor and advisor. He has impressed me with his knowledge across diverse disciplines in science. His ability to think critically with open-minded attitude has always had positive influence on me. I feel I got trained as a scientist who can be critical of my own data and reach out beyond the comfort-zone of my current abilities. Thanks to him, I got my first experience in many disciplines in science as this dissertation will show. I am very fortunate to be in his lab. I got to experience the true chemical biology, which was my primary reason for coming to this university.

I would like to thank the Rackham Graduate school providing me with the pre-doctoral fellowship and travel grants.

Finally, I would like to acknowledge the past and present lab members of the Martin lab for providing wonderful support. To mention a few, I would like to thank Dr. David Davda for teaching me technical skills in biochemistry and Dr. Chris Tom for the organic synthesis. Dr. Jaimeen Mujmudar for very helpful advice on chemical synthesis as well as proteomic analysis. Melanie Cheng See Kit and Sarah Haynes for their support. These people made my journey in Michigan easier and it will never be forgotten.

Table of Contents

List of Figures

FIGURE

List of Tables

TABLE

List of Appendices

APPENDIX

Abstract

Proteins are often regulated through the addition of chemical modifications that modulate localization, activity, and interactions. Protein *S*-palmitoylation describes the attachment of long-chain fatty acids to cysteine residues in proteins to promote membrane association, which contributes to the regulation of a number of cellular processes. Altered *S*-palmitoylation contributes to the pathogenesis of neurological disorders, cancer, and many other diseases. Importantly, dynamic *S*-palmitoylation is required to modulate the activity of proteins in response to various extracellular signaling events. This includes various membrane-associated or membrane proteins such as G proteins, small GTPases, receptors, scaffold proteins, cytoskeletal proteins, and kinases. These observations suggest that enzymes catalyzing the removal of palmitate must also play a critical role in modulating the activity of hundreds of essential proteins. Therefore, it is important to characterize how *S*-palmitoylation is regulated, which will provide a more complete molecular picture of how cells adjust to various signaling events. Over the last decade, potent inhibitors of depalmitoylases have been developed, yet the basic mechanisms and the cellular functions of depalmitoylases remain poorly characterized. Since depalmitoylation can modulate select cell signaling events, I hypothesized that depalmitoylase enzymes have dedicated substrates and differentially contribute to the global dynamic *S*-palmitoylation regulation. My dissertation addresses this hypothesis by focusing on the structure, function, and inhibition of the depalmitoylating enzymes APT1 and APT2. The first chapter of this thesis provides an overview of depalmitoylating enzymes. Second, I used isoform-selective inhibitors to understand the structure, substrate engagement and selectivity of APT1 and APT2. Third, I validated the selectivity of the APT2 inhibitor ML349 by affinity enrichment and proteomics. Finally, I explore the dynamic rate of palmitoylation regulated by depalmitoylases in cells. Overall, my research has clarified the mechanism and function of protein de-palmitoylation in cell regulation.

Chapter 1 : Protein Depalmitoylases*

Abstract

Protein depalmitoylation describes the removal of thioester-linked long chain fatty acids from cysteine residues in proteins. For many *S*-palmitoylated proteins, this process is promoted by acyl protein thioesterase enzymes, which catalyze thioester hydrolysis to solubilize and displace substrate proteins from membranes (**Figure 1.1**). The closely related enzymes acyl protein thioesterase 1 (APT1; LYPLA1) and acyl protein thioesterase 2 (APT2; LYPLA2) were initially identified from biochemical assays as G protein depalmitoylases, yet later were shown to accept a number of *S*-palmitoylated protein and phospholipid substrates. Leveraging the development of isoform-selective APT inhibitors, several studies report distinct roles for APT enzymes in growth factor and hormonal signaling. Recent crystal structures of APT1 and APT2 reveal convergent acyl binding channels, suggesting additional factors beyond acyl chain recognition mediate substrate selection. In addition to APT enzymes, the ABHD17 family of hydrolases contributes to the depalmitoylation of Ras-family GTPases and synaptic proteins. Overall, enzymatic depalmitoylation ensures efficient membrane targeting by balancing the palmitoylation cycle, and may play additional roles in signaling, growth, and cell organization. In this chapter, we provide a perspective on the biochemical, structural, and cellular analysis of protein depalmitoylases, and outline opportunities for future studies of systems-wide analysis of protein depalmitoylation.

* This chapter presents a published peer-reviewed review article. Won S. J. et al *Crit Rev Biochem Mol Biol*. 2018 53(1):83-98

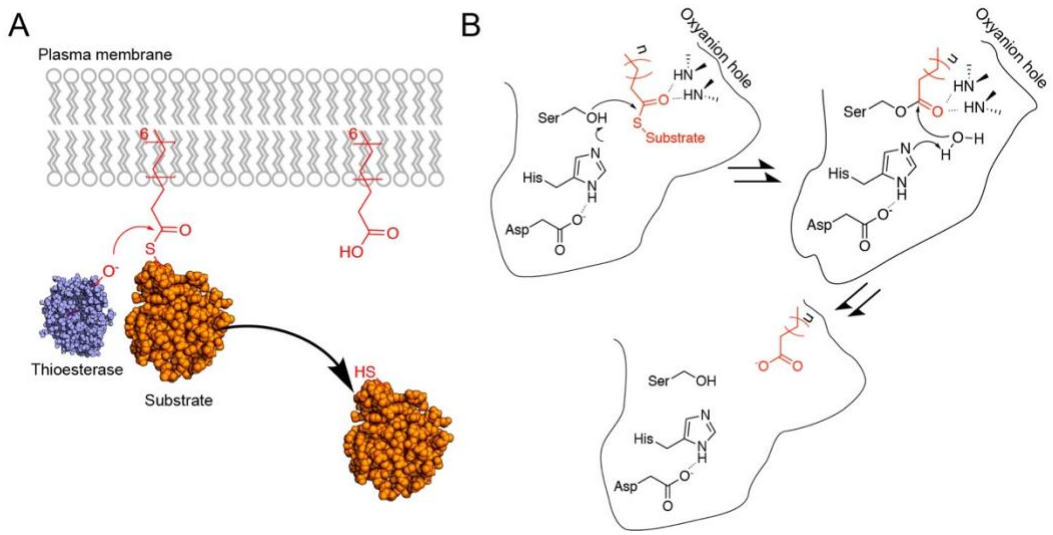

Figure 1.1 Graphical abstract showing depalmitoylation event mediated by a thioesterase.

(A) A cartoon showing localization of palmitoylated substrate before and after hydrolysis by a thioesterase. (B) A generic chemical mechanism of serine hydrolase in action.

Introduction

S-Palmitoylation describes the addition of a long-chain fatty acid to a cysteine residue via a thioester linkage.[1] This hydrophobic post-translational modification promotes the membrane tethering, trafficking, and localization of a significant fraction of membrane-associated proteins. While the term "*S*-palmitoylation" implies exclusive modification by 16:0 fatty acids, the cellular profile of fatty acylated cysteine residues likely includes a variety of long chain fatty acids with differing unsaturation,[2-4] and is interchangeably used with the term "*S*-acylation". Protein *S*-palmitoylation is catalyzed by a family of protein acyl transferases, termed zDHHC enzymes due to their predicted Zn^{2+}-binding and conserved Asp-His-His-Cys motif.[5-7] These multipass transmembrane proteins catalyze acyl transfer from long chain fatty acyl-CoAs to cysteine residues in proteins. Humans express 23 zDHHC enzymes that influence many diverse cellular pathways. For example, zDHHC5 deletion blocks neuronal stem cell differentiation,[8] and along with its close homologue zDHHC8, localize to synapses in neurons[9] where they influence activity-dependent endocytic trafficking, excitability, and synaptic connectivity.[10] In addition, zDHHC2 palmitoylates Src-family kinases,[11] while inhibition of close homologue zDHHC20 prevents EGFR *S*-palmitoylation and enhances the action of EGFR inhibitors.[12] zDHHC9 is reported to *S*-palmitoylate Ras,[13, 14] and is

genetically linked to X-linked mental retardation.[15] Across dozens of publications, zDHHC enzymes have emerged as critical regulators of protein *S*-palmitoylation and membrane targeting.[1, 16]

Perhaps the most intriguing aspect *S*-palmitoylation is its reversibility, since thioester hydrolysis eliminates the fatty acyl anchor to modulate membrane localization and/or function. For example, cycles of acylation and deacylation are required for the plasma membrane association of Ras-family small GTPases and G proteins,[17-19] establishing a distinct mode of peripheral membrane protein directionality dependent on a continuous palmitoylation cycle.[20, 21] Indeed, pharmacological inhibition with promiscuous inhibitors of either zDHHC PATs or depalmitoylases block the plasma membrane targeting of Ras and G proteins.[20, 22, 23] Microinjection of semi-synthetic fluorescently-labeled *S*-palmitoylated Ras rapidly redistributes to the golgi, which is established as the destination of depalmitoylated Ras.[21] Based on these findings, peripheral membrane protein *S*-palmitoylation requires a balanced cycle of both zDHHC enzymes and depalmitoylating enzymes for efficient transport along the flux of the secretory pathway towards the plasma membrane.[20] Furthermore, both Ras and G proteins are rapidly depalmitoylated in their GTP-bound state,[24-26] which coincides, but is not required for agonist dependent-internalization to internal membranes.[23] Based on these examples, constitutive protein *S*-palmitoylation is required for proper trafficking of many peripheral membrane proteins, but may also function as a reversible signal analogous to protein phosphorylation (**Figure 1.2**). For example, serum, growth factor, or phorbol ester addition triggers deacylation of a 64 kD protein in [^{3}H]-palmitate labeled mouse BH_3C1 cells,[27] which in light of more recent proteomics studies,[28] likely corresponds to depalmitoylation of Metadherin, a major driver of cancer and metastasis.[29] Therefore, external stimuli trigger either direct activation of depalmitoylases, or facilitate conformational changes that enhance depalmitoylase accessibility, which then tip the balance of the palmitoylation cycle to reorganize membrane distribution and signaling outputs.

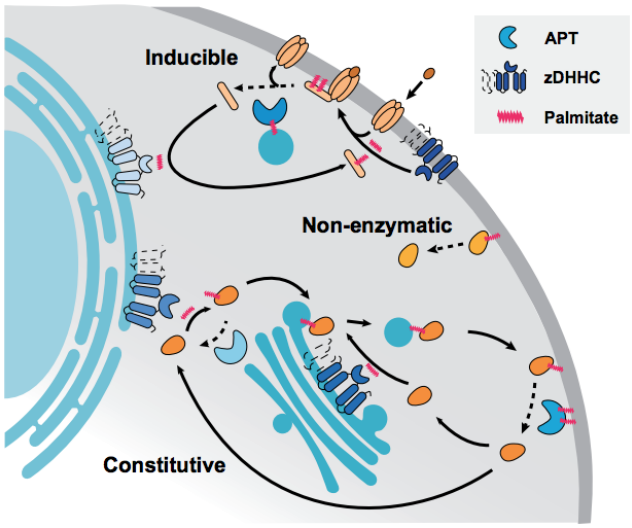

Figure 1.2 Cellular pathways of protein depalmitoylation.

Protein depalmitoylation can proceed by either non-enzymatic hydrolysis, inducible depalmitoylation, or constitutive depalmitoylation during trafficking. zDHHC enzymes are shown as transmembrane proteins.

While this model is appealing, a number of fundamental questions remain, such as 1) what enzymes catalyze depalmitoylation of different *S*-palmitoylated proteins, 2) what, if anything, triggers their activation, and 3) is there a coincident dysregulation of protein acyl transferase enzymes to block re-palmitoylation? In addition to peripheral membrane proteins, many integral membrane proteins such as channels, receptors, and adhesion proteins also require *S*-palmitoylation for proper activation, sensitization, or microdomain localization. Given the ever-expanding number of bona fide *S*-palmitoylated proteins,[30] how broad is the role for depalmitoylases in regulating *S*-palmitoylation stability? What is the scope of enzymatic depalmitoylation compared with the intrinsic hydrolysis of the high-energy thioester linkage? Through the development of new methods and model systems, these questions are central to understanding the role of dynamic *S*-palmitoylation in physiological systems.

Assays for depalmitoylation

Protein *S*-palmitoylation was first reported nearly 40 years ago,[31] but even the most basic experiments were hindered by the limitations of [^{3}H]-palmitate labeling. The low radioactivity and incorporation efficiency typically required weeks to return results for a single experiment.[32] Furthermore, assaying [^{3}H]-palmitate incorporation requires immunoprecipitation of a single protein, limiting the scope of the analysis to only specific

hypotheses. Nonetheless, [^{3}H]-palmitate metabolic labeling is the most accepted method for studying *S*-palmitoylation, particularly for measuring stability in pulse-chase assays. In this approach, cells are labeled with [^{3}H]-palmitate for a fixed amount of time, followed by washes and incubation in media supplemented with excess unlabeled palmitic acid.[32] After immunoprecipitation and SDS-PAGE, the rate of palmitate turnover on a specific protein can be quantified by autoradiography. Through such analysis, the rate of protein *S*-palmitoylation turnover is generally faster than the rate of protein turnover, establishing that multiple *S*-palmitoylation and depalmitoylation events occur throughout the lifetime of an *S*-palmitoylated protein.[28] Thus, different PATs and APT enzymes may function at different stages of protein trafficking to promote plasma membrane delivery and residency.

The recent development of non-radioactive detection methods has rejuvenated interest in *S*-palmitoylation, providing simple methods that accelerate the identification and quantitation of *S*-palmitoylated proteins.[33, 34] The primary method for biochemical analysis of *S*-palmitoylation uses hydroxylamine to hydrolyze all thioesters across the proteome, followed by capture of the newly liberated thiols.[35-37] These hydroxylamine-switch methods begin with reduction of disulfides with tris(2-carboxyethyl)phosphine (TCEP), followed by treatment with maleimide to alkylate all reduced thiols. Next, neutral hydroxylamine is added to hydrolyze thioesters, which coincidentally hydrolyzes other mechanistic protein-linked thioesters including ubiquitin ligases and lipoamide-dependent dehydrogenases. Any hydroxylamine sensitive thiols are then captured using a pyridyl-disulfide biotin conjugate for streptavidin-resin enrichment (biotin-exchange) or captured directly with pyridyl-disulfide resin (Acyl-resin assisted capture; Acyl-RAC) for further analysis.[38] Pyridyl-disulfide resin capture has at least three advantages. First, it limits capture to hydroxylamine-sensitive thioesters, and does not capture products from other ester or other functional groups. Second, the captured disulfide adduct is easily reversible by TCEP, allowing simple elution for gel-based or proteomic analysis of site-specific *S*-palmitoylation. Finally, since these methods avoid metabolic labeling, primary tissues can be readily analyzed to provide a snapshot of the steady state levels of *S*-palmitoylation. Most importantly, biotin-exchange and acyl-RAC have enabled mass spectrometry-based discovery and analysis across hundreds of *S*-palmitoylated

proteins, allowing correlated annotation of the exact sites of *S*-palmitoylation.[38] Such large-scale profiling efforts provide long lists of putative *S*-palmitoylated proteins, which warrant additional biochemical validation. This is somewhat mitigated by the *S*-palmitoylation database SwissPalm,[30] which provides a searchable platform to qualify candidates across published datasets and compare data from distinct experimental systems, enrichment methods, and laboratories.

The commercially available alkynyl fatty acid derivative 17-octadecynoic acid (17-ODYA) provides a second non-radioactive approach for detecting *S*-palmitoylation.[34, 39, 40] After addition to the cell culture media, cells process the free alkynyl fatty acid to form the coenzyme A (CoA) conjugate, which then serves as a substrate for enzymatic transfer to endogenous sites of *S*-palmitoylation. Cells collected at different time points are then lysed and conjugated by copper-catalyzed azide alkyne cycloaddition (CuAAC) to reporter-linked azides (fluorophores or biotin) for gel-based or mass spectrometry analysis. Saturated incorporation typically occurs in a few hours, although shorter time points can probe more rapid acylation events. For mass spectrometry-based analysis, lysates are conjugated to biotin-azide for streptavidin enrichment, and comparative mass spectrometry is performed using hydroxylamine-treated or palmitic acid treated samples as controls. Additional precautions are necessary to prevent thioesterase hydrolysis during sample preparation, including addition of generic esterase inhibitors, limited total sample processing time, and careful monitoring of the pH of all reagents.[41] Several proteomic studies report bioorthogonal alkynyl-fatty acid labeling for profiling *S*-palmitoylation, including analyses in immune cells,[8, 28, 42] epithelial cells,[43] and protozoa.[44, 45] Importantly, alkynyl-fatty acid labeling provides a natural complement to hydroxylamine-switch methods, establishing two distinct enrichment methods for more confident analysis.

Alkynyl-fatty acid metabolic labeling has opened new opportunities for non-radioactive profiling of dynamic changes in *S*-palmitoylation. For example, Lck *S*-palmitoylation turnover in Jurkat T-cells was assayed using alkynyl-fatty acid pulse-chase methods and quantified by in-gel fluorescence.[46] Surprisingly, Lck depalmitoylation was accelerated after treatment with the phosphatase inhibitor pervanadate, yet stabilized by incubation with the non-selective hydrolase inhibitor

methyl arachidonyl fluorophosphonate (MAFP). Thus, activated T-cells increase Lck *S*-palmitoylation cycling, which is dependent on one or more MAFP-sensitive thioesterase enzymes.

Using similar pulse-chase methods, proteome-wide *S*-palmitoylation dynamics were profiled by quantitative proteomics in a mouse B-cell line.[28] Using stable isotope labeling with amino acids in cell culture (SILAC) methods, matched “light” and “heavy” replicates were labeled with 17-ODYA over a 2 hr pulse. One of the samples was then further incubated with 10-fold excess palmitic acid in the presence of the translation inhibitor cycloheximide. After combining the two samples together, the pooled lysates were conjugated to biotin-azide for enrichment and quantitative proteomic analysis. While most *S*-palmitoylated proteins cycled palmitate at a uniform rate in the pulse-chase assay, a subset of proteins demonstrated accelerated turnover, including G proteins, Ras-family GTPases, and a number of cell polarity proteins. Furthermore, treatment with the non-selective lipase inhibitor hexadecylfluorophosphonate (HDFP) stabilized the same subset of dynamically *S*-palmitoylated proteins, confirming direct enzymatic contribution to *S*-palmitoylation dynamics on key signaling and polarity scaffolding proteins. Based on these results, the majority of *S*-palmitoylated proteins undergo basal hydrolysis, while a small subset of *S*-palmitoylated proteins are rapidly depalmitoylated by HDFP-sensitive lipases.

Alkynyl fatty acid labeling has several inherent limitations, primarily the direct incorporation of the labeled fatty acid across a variety of phospholipids. Longer incubation times lead to more extensive alkynyl-fatty acid incorporation into phospholipid pools,[47] reducing the effectiveness of any later chase with free palmitate. This pulse-chase suppression potentially excludes a number of proteins from dynamic analyses. Furthermore, addition of palmitate has major effects on cellular metabolism. For instance, addition of 500 μM palmitate to human primary melanocytes expressing the variants of the melanocortin 1 receptor (MC1R) increased cAMP levels by almost 3-fold, potentially through direct enhancement of GPCR *S*-palmitoylation.[48] Exogenous fatty acids also increase cellular acyl-CoA levels,[4] which may enhance *S*-palmitoylation levels by driving zDHHC activity or by non-enzymatic thioester exchange with accessible cysteine residues. For example, 17-ODYA in the presence of 2-

bromopalmitate (a non-selective palmitoylation inhibitor) only partially reduces incorporation of the 17-ODYA.[49] Therefore, non-enzymatic palmitoylation levels may be enhanced by 17-ODYA incubation, elevating acyl-CoA pools to driving non-physiological thioester exchange to enhance levels of *S*-acylation.

Another major caveat is metabolic labeling can only occur at accessible, reduced cysteines. Thus, stable *S*-palmitoylated cysteines are essentially invisible, since they do not turnover to present a free thiol substrate for zDHHC PAT enzymes. Accordingly, the more stable *S*-palmitoylation site, the more challenging it is to assay by metabolic labeling. In addition, high palmitate levels can induce oxidative stress,[50] which may trap depalmitoylated thiols as oxidized disulfides or glutathione adducts. Different zDHHC enzymes have also been shown to prefer different fatty acyl-CoAs,[4] suggesting an additional level of diversity that could select against a single alkynyl fatty acid species to bias probe incorporation. Varying the acyl length of the alkynyl reporter revealed different acyl preferences, particularly since terminal azide conjugates surprisingly have little influence on zDHHC acyl specificity.[4] Moreover, any differential turnover rates between distinct sites in the same protein are effectively averaged in shotgun proteomics experiments, since there are no robust mass spectrometry methods to broadly profile fatty *S*-acylated peptides. [^{3}H]-palmitate can be elongated or shortened by ß-oxidation, further diversifying the labeled acyl species. This is particularly problematic when 17-ODYA is shortened to 15-pentadecynoic acid, which is enzymatically incorporated into *N*-myristoylation sites.[34] Despite these pitfalls, metabolic labeling remains the only approach to profile *S*-palmitoylation dynamics, on select proteins or across the proteome.

Palmitoyl protein thioesterase 1

Several early reports demonstrated enhanced depalmitoylation upon hormonal stimulation, suggesting activation of specific depalmitoylases might regulate intracellular signaling pathways.[25, 26, 51] For example, both Ras and G proteins are more rapidly depalmitoylated after activation, which was believed to contribute to more efficient internalization. Several candidate depalmitoylating enzymes were later identified by activity-guided fractionation and purification from soluble tissue homogenates.[52, 53]

While technically feasible, this approach ignored the presence of any membrane-bound depalmitoylating enzymes.

Nonetheless, the lysosomal hydrolase PPT1 was identified as the most robust H-Ras depalmitoylase *in vitro.*[52] PPT1 was later found to localize exclusively in lysosomes and late endosomes,[54] functionally separating PPT1 from depalmitoylase activity in the cytosol or on plasma membrane. PPT1 is one of 14 genes genetically linked to the family of human neuronal ceroid lipofuscinosis (NCL) lysosomal storage diseases, characterized by accumulation of lysosomal autofluorescent storage material, neurodegeneration, and childhood mortality.[55] Interestingly, while not localized in the lysosome, mutations in cysteine string protein alpha gene (CSPα) also lead to NCL.[56] CSPα is multiply *S*-palmitoylated, and functions as a HSC70 interacting J-protein important for protein folding and synaptic vesicle function. In CSPα mutant cells, PPT1 is highly over-expressed.[57] Furthermore, PPT1 can depalmitoylate CSPα *in vitro*, which is reported to lead to the formation of insoluble aggregates. Acyl-RAC analysis of CSPα mutant cells revealed decreased *S*-palmitoylation of several synaptic proteins and neuronal signaling proteins. Overall, PPT1 is likely not contributing to plasma membrane depalmitoylation, but could play a role in vesicular depalmitoylation and lysosomal degradation of *S*-palmitoylated proteins.

Acyl protein thioesterases

The reported lysophospholipase LYPLA1 was identified by screening soluble tissue homogenates for G protein depalmitoylase activity,[53] and subsequently renamed acyl protein thioesterase 1 (APT1). In addition to its depalmitoylase activity, APT1 hydrolyzes a broad profile of lysophospholipids and other long-chain mono-acyl glycerol esters, albeit at a lower catalytic efficiency than high-energy *S*-palmitoylated substrates.[58, 59] Since APT1 was first reported before the development of RNAi methods, much of the first decade of depalmitoylase research relied on *in vitro* biochemistry or over-expression studies. Over-expression of APT1 enhances the depalmitoylation of small GTPases,[60, 61] endothelial nitric oxide synthase,[62] and a number of other peripheral membrane proteins in transfected cells. Such over-expression could lead to a number of potential artifacts, either by disruptive fusion of epitope tags or fluorescent proteins, or through saturation of binding partners at non-

physiological expression levels. If the enzyme concentration increases much beyond physiological levels, the rate of substrate hydrolysis will also increase, and potentially promote depalmitoylation of non-physiological substrates. In addition, over-expression could also impart non-physiological depalmitoylase activity to otherwise dedicated lipid modifying enzymes, particularly since thioesters are high energy bonds readily hydrolyzed by even weak nucleophiles. Over-expressing candidate *S*-palmitoylated substrates is also problematic, since high expression levels can approach the enzyme K_m, further promoting APT1-dependent depalmitoylation of non-native substrates. Even so, APT1 can depalmitoylate a number of proteins in cells. In fact, the neuronal microRNA mi138 modulates APT1 levels in synaptic spines, reportedly affecting spine volume through modulation of $G\alpha_{13}$ *S*-palmitoylation.[63]

In addition to APT1, vertebrates express the highly similar depalmitoylase APT2, (68% identical, 81% similar). APT2 also hydrolyzes lysophospholipids,[64] but in contrast to APT1, it also hydrolyzes prostaglandin glycerol esters.[65] Both APT1 and APT2 act as efficient depalmitoylases *in vitro*,[59] and are presumed to broadly regulate *S*-palmitoylation and trafficking of peripheral membrane proteins in cells. Unfortunately, there are no quality commercial sources of APT1 and APT2 antibodies, since they are likely poorly immunogenic due to nearly exact conservation across most mammals, including mice, rabbits, and humans. Thus, most studies on APT1 and APT2 localization have used GFP or epitope fusions for subcellular analysis. The literature consensus reveals both enzymes are primarily cytoplasmic, although partially localized on internal membranes[66] or in some instances on the plasma membrane.[60, 67] Both APT1 and APT2 share a cysteine at the second position immediately following the initiator methionine, and are reportedly both *S*-palmitoylated.[60, 66, 68] After removal of the initiator methionine, if the N-terminus is not acetylated, it may readily undergo *N*-acyl transfer to form a stable amide linkage. Interestingly, APT1 *S*-palmitoylation has been reported in only one proteomics experiments using hydroxylamine switch methods, but never by alkynyl fatty acid labeling.[30, 68] APT1 and APT2 are expressed and active across nearly all tissues,[69, 70] yet their absence in most large-scale profiling efforts suggests they may not be stoichiometrically *S*-palmitoylated. This low-level *S*-palmitoylation could be caused by an alternative translational start site (potentially Met-

6) or through auto-depalmitoylation. Nonetheless, knockdown of either APT1 or APT2 promotes plasma membrane association of the other APT enzyme, suggesting an interdependent *S*-palmitoylation cycle.[60]

Based on their predicted role in regulating peripheral membrane protein localization, peptidomimetic inhibitors of APT1 were developed that upon microinjection could mislocalize N-Ras away from the plasma membrane.[71] Based on these studies, derivatives of the generic natural product lipase inhibitor tetrahydrolipstatin were identified that potently inhibited both APT1 and APT2.[61] The β-lactone mechanism-based inhibitors Palmostatin B and the choline-derivative Palmostatin M [59] were developed as dual inhibitors of both APT enzymes. Palmostatin B treatment led to accumulation of N-Ras on internal membranes, as well as partial rescue of E-Cadherin membrane localization.[61] Interestingly, knockdown of APT1 was not sufficient to reproduce the pharmacological effects to statistical significance, demonstrating possible compensatory mechanisms, either by APT2 or by other unannotated depalmitoylating enzymes. Single cell studies revealed altered trafficking dynamics of over-expressed N-Ras fluorescent protein fusions and microinjection of semi-synthetic, fluorescently labeled N-Ras. Upon growth factor stimulation, Palmostatin B treated cells showed reduced Ras activation on the golgi. Later studies demonstrated selective growth inhibition of N-Ras, but not K-Ras driven growth of myeloid progenitors.[72] Accordingly, Palmostatin B directly modulates N-Ras localization and activity by disrupting the Ras palmitoylation cycle.[73]

While Palmostatin B demonstrates high potency against both APTs (IC_{50} < 5 nM),[59] phenotypic effects typically require > 20 μM.[61, 74, 75] Early studies suggested that Palmostatin derivatives are highly unstable in serum, requiring repeated cycles of inhibitor addition to maintain inactivation.[63] Nevertheless, this compound has been used in numerous studies to profile APT1 and APT2 function. For instance, Palmostatin B addition accelerated the incorporation of the 17-ODYA in Lck in unstimulated T-cells.[76] However, the compound failed to block depalmitoylation once the cells were stimulated with Fas ligand. The authors suggested that there may be distinct pools of depalmitoylases once the receptors are activated. In addition, the neuronal RGS-binding protein R7BP accelerates the deactivation of $G_{i/o}$ proteins. Inhibition with

Palmostatin B or HDFP both redistributed R7BP from the plasma membrane to endomembranes, disrupted association with G protein-regulated inwardly rectifying potassium (GIRK) channels, and slowed GIRK channel closure.[77] Importantly, knockdown of both APT1 and APT2 had no effect on GIRK inactivation, suggesting the presence of additional depalmitoylated enzymes. Chronic lymphocytic leukemia (CLL) B-cells express nearly 10-fold more APT2 and 2-fold more APT1. Palmostatin B treatment or APT knockdown increased CD95-mediated apoptosis.[78] Activity-based protein profiling (ABPP) studies later demonstrated that Palmostatin B is not exclusive for APT1/APT2, and inactivates a number of other lipid processing serine hydrolases with somewhat weaker potency, including ABHD6, ABHD16A, ABHD17A-C, PNPLA6, and FASN.[79] Accordingly, Palmostatin B should be used only as a generic depalmitoylase inhibitor, with a clear understanding that multiple enzymes are blocked at concentrations required for sustainable depalmitoylase inhibition, and the biological outcomes may reflect polypharmacology summed across many enzymes.

Despite these issues, Palmostatin B remains a popular tool for blocking depalmitoylase activity, and even attenuates depalmitoylation *in vivo* after intraperitoneal injection.[48] The MC1R G-protein-coupled receptor triggers melanin production and enhances DNA repair after ultraviolet irradiation. Mice with red hair MC1R variants have reduced MC1R *S*-palmitoylation, weaker cAMP stimulation, and are more susceptible to developing melanoma. Remarkably, intraperitoneal injection of Palmostatin B (10 mg kg^{-1}) prior to UV irradiation increased MC1R *S*-palmitoylation and clearance of DNA photoproducts while reducing tumor growth. While Palmostatin B is promiscuous, at this relatively low-dose, APTs are likely to be the primary targets. APT inhibition also prevents melanoma tumor cell invasion by regulating the *S*-palmitoylation of the polarity organizing protein MCAM.[51] Wnt5a stimulation promotes APT1-dependent depalmitoylation of MCAM, inducing asymmetric MCAM localization to promote a more invasive state. Taken together, APT inhibitors may be valuable prophylactics in topical sunscreens to prevent melanoma. Nonetheless, the APT1 and APT2 inhibitors ML348 and ML349 had no effect on MAPK signaling or growth across several N-Ras-dependent melanoma cell lines,[80] demonstrating APT activity is not essential across all cancers types or stages.

A number of more selective APT inhibitors have been developed with more drug-like properties. Isoform-selective inhibitors of APT1 (ML348, K_i = 280 nM) and APT2 (ML349, K_i = 120 nM) were identified by high throughput screening in a competitive fluorescence polarization assay.[81-83] These inhibitors share a common piperazine-amide scaffold, but diverge through additional modifications to impart isoform selectivity. For example, APT1 inhibitor, ML348 has piperazine amide adjacent to a furanyl group but APT2 inhibitor, ML349 has a thiophene conjugated to thiochromane 1,1-dioxide. These isoform-selective inhibitors are active *in vivo* following intraperitoneal injection, and engage their respective targets across all major tissues.[83] Furthermore, chemical proteomics analysis of biotin-conjugated ML349 confirmed largely selective inhibition across the proteome at low micromolar concentrations.[84] Other covalent APT1/APT2 dual inhibitors have been reported, including the commercially available triazole urea ML211[85, 86] and the commercially available *N*-hydroxyhydantoin carbamate ML378.[87, 88] ML211 is more potent, yet the higher reactivity reflects a smaller selectivity window limiting *in vivo* applications. ML378 also inhibits ABHD6 and FAAH in mouse brain homogenates, yet selective inhibitors to ABHD6 and FAAH can be used as anti-target controls. Based on our studies, we highly recommend ML348 and ML349 as probes for exploring APT function in cells and model organisms (**Figure 1.3**).

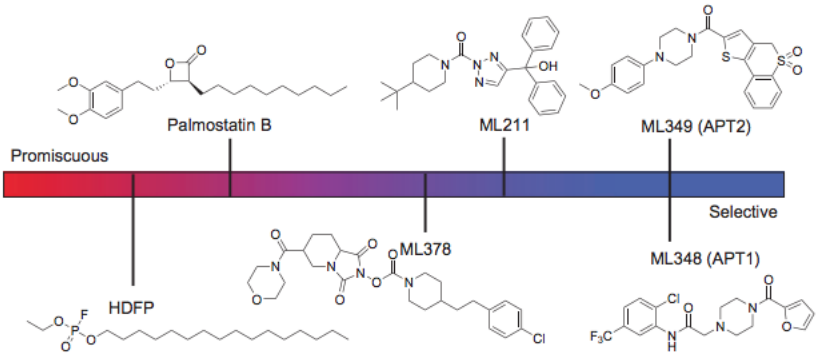

Figure 1.3 APT inhibitor selectivity index.

All listed inhibitors are commercially available, except the promiscuous lipase inhibitor HDFP. HDFP (fluorophosphonate), Palmostatin B (b-lactone), ML378 (*N*-hydroxyhydantoin carbamate), and ML211 (triazole urea) are covalent inhibitors, although the covalent Palmostatin B adduct is slowly reversible. ML211 inhibits ABHD11[86] and PPT1 (unpublished). ML378 inhibits ABHD6, FAAH, and PPT1 at higher doses.[87]

Arguably, the development of APT inhibitors has outpaced detailed biochemical analysis of APT function in cells. According to pulse-chase *S*-palmitoylation proteomics studies, the

tumor suppressor Scribble (Scrib) demonstrated the fastest *S*-palmitoylated turnover in aggressive B-cell hybridoma cells.[28] Importantly, this turnover was completely blocked by treatment with the non-selective lipase inhibitor HDFP. Originally identified in *Drosophila*, the cell polarity tumor suppressor Scrib has emerged as a central regulator of cell growth, invasion, and malignancy.[89-91] While Scrib is not widely mutated in cancers, its mislocalization and amplification are clinically correlated with high-grade cervical carcinomas,[92, 93] as well as malignant colon,[94] prostate,[95] breast cancers,[95, 96] and other epithelial cancers [97] (**Figure 1.4A-B**). In addition, Scrib$^{+/-}$ heterozygous male mice develop widespread epithelial hyperplasia,[95] and MMTV-driven conditional knockout of Scrib in female mice induces breast hyperplasia and widespread tumor formation.[91]

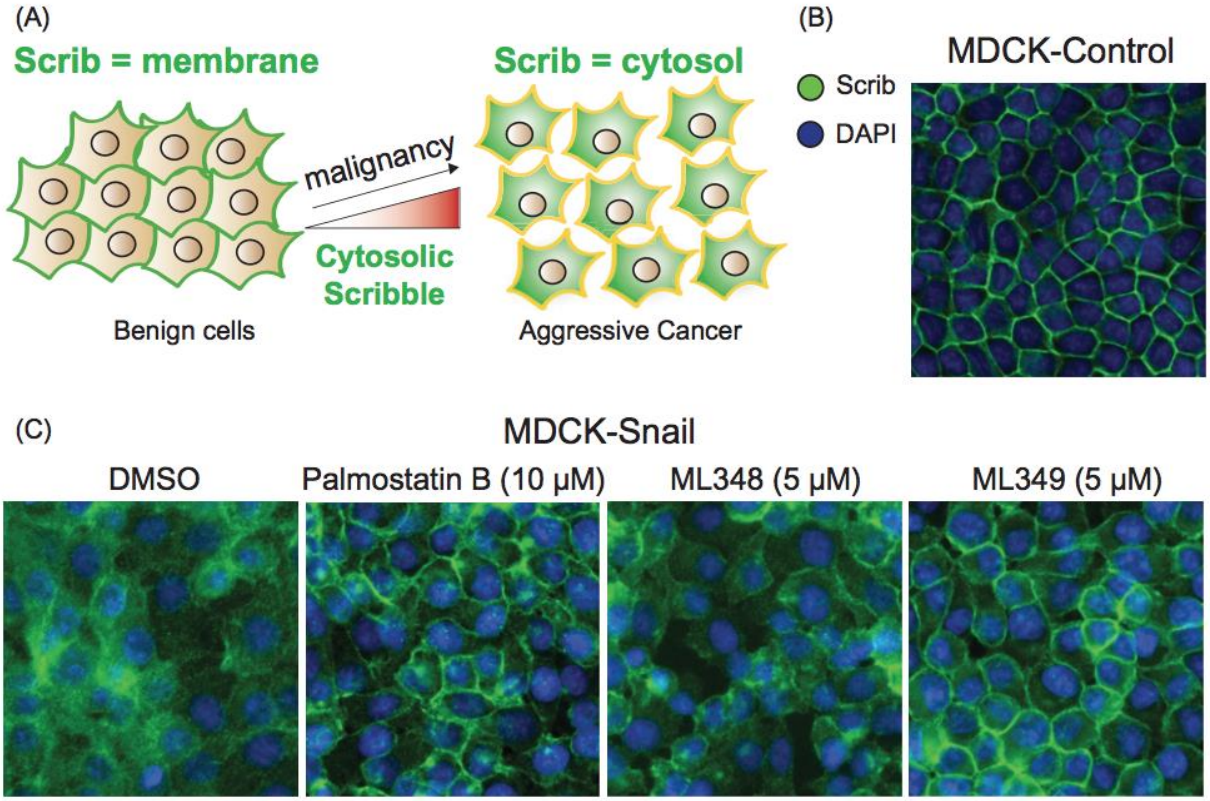

Figure 1.4 APT2 inhibition restores Scribble plasma membrane localization in Snail-expressing cells.

(A) Scribble (Scrib) moves from the plasma membrane to the cytosol in the more malignant cells. (B) Scrib is localized at the plasma membrane in MDCK polarized epithelial cells. (C) APT2 inhibition significantly rescues Scrib plasma membrane localization in Snail expressing MDCK cells. Adapted from Hernandez et al.[75]

In order to explore the mechanism of Scrib membrane mislocalization in cancer, we engineered cells to over-express the epithelial to mesenchymal transition transcription factor (EMT-TF) Snail. Snail reprograms cells to transform to a more stem

cell-like state, which eliminates basolateral polarity and leads to Scrib translocation from membrane to the cytosol [98] (**Figure 1.4C**). Importantly, Scrib fusion to a C-terminal CAAX prenylation motif is reported to rescue plasma membrane localization and reduces levels of activated TAZ,[98] the central transducer of the Hippo signaling pathway. Without its plasma membrane localization, Scrib no longer represses Ras/MAPK-driven cell invasion and EMT phenotypes, yet retains the ability to suppress anchorage-independent growth.[99] Interestingly, Snail expression in either MDCK or MCF10A cells led to the repression of select zDHHC protein acyl transferases and increased expression of the depalmitoylase APT2, suggesting Snail initiates a transcriptional program that directly targets the *S*-palmitoylation cycle.[43, 75] When Snail over-expressing cells are treated with the APT2 inhibitor ML349 or APT2 siRNAs, Scrib localization is largely restored to the plasma membrane, rescuing markers of cell polarity and suppressing MAPK signaling [75] (**Figure 1.4C**). ML349 had no effect on Ras-GTP levels, but markedly reduced Raf and MEK activation, suggesting *S*-palmitoylated Scrib organizes a signaling complex that regulates Raf activation downstream of Ras. Importantly, overnight incubation with Palmostatin B also rescued Scrib membrane localization, but required 100-times higher concentrations than ML349. Surprisingly, the APT1 inhibitor ML348 had no effect on Scrib localization, confirming isoform-selective depalmitoylase regulation of *S*-palmitoylation. Altogether, this data demonstrates that APT2, but not APT1, participates in an altered *S*-palmitoylation cycle that becomes imbalanced to promote pathways that drive malignancy. Furthermore, this work established a unique biochemical pathway that reverts certain malignant phenotypes in cancer through pharmacological perturbation of the Scrib palmitoylation cycle, without directly affecting Ras activation or signaling.

Beyond their role as protein depalmitoylases, APT enzymes can also hydrolyze a variety of other esters and thioester metabolites.[100] APT1 and APT2 were originally characterized as lysophospholipase enzymes, yet later studies demonstrated enhanced catalytic efficiency towards acyl-thioester-linked proteins. Interestingly, APT2 was identified as the primary prostaglandin glycerol esterase, while APT1 had no significant activity.[65] Both APT1 and APT2 accelerate the deacylation of octanoyl-ghrelin in serum, suggesting these enzymes may also be secreted from cells.[101] Lipopolysaccharide

treatment increased in APT1 serum levels, potentially through release from liver. Furthermore, the intracellular APT1 mRNA and protein levels were reduced after LPS stimulation, yet APT2 levels were unaffected. Overall, APTs likely hydrolyze a number of more soluble acyl-esters and thioesters, and may have broader functional roles *in vivo* beyond depalmitoylation.

To add spatial and temporal resolution to depalmitoylation enzymes, a series of mechanism-based octanoyl-thioester fluorogenic probes were developed for live cell imaging.[102] Approximately half of the probe fluorescence in HEK293T cells was blocked by ML348 or Palmostatin B, and APT1 siRNA knockdown reduced probe fluorescence by 25%. Interestingly, EGF stimulation reduced probe fluorescenbce by about 10% in live cells, suggesting some growth factor regulation of deacylase activity. While intriguing, further evidence is needed to establish if such reductions affect steady-state cellular *S*-palmitoylation levels, particularly of S-palmitoylated growth signaling mediators. Given the large number of candidate octanoyl-thioesterases, these probes provide a useful cell-based platform to explore deacylase activity in live cells, and measure contributions across different candidate enzymes.

Structural insights to APT enzymes

In order to explain the functional differences between APT1 and APT2, the first high-resolution structures bound to their respective inhibitors[103] were recently solved. The structures of these enzymes will be further discussed in the next chapter. While the structure of apo-APT1 was reported,[104] there were no additional studies to analyze the structure of APT1 or any structures of APT2 for comparison. Before solving the structures of each enzyme, we profiled the thermostability of APT1 and APT2 bound to different ligands. APT1 was more thermostable than APT2 (5ºC), suggesting previous efforts to crystalize APT2 were likely stymied by additional flexibility or disorder. Compared to free enzyme, APT1 binding to ML348 or APT2 binding to ML349 increased the thermostability by 4ºC, which confirms thermodynamically favorable inhibitor engagement. Furthermore, incubation with HDFP led to a surprising 10ºC stabilization. Accordingly, APT enzymes were predicted to harbor an acyl-binding pocket to stabilize the enzyme upon substrate binding. Based on these observations, we identified co-crystallization conditions and solved the structures of both

APT1•ML348 (1.55 Å; 5SYM) and APT2•ML349 (1.64 Å; 5SYN) by x-ray crystallography (**Figure 1.5**).

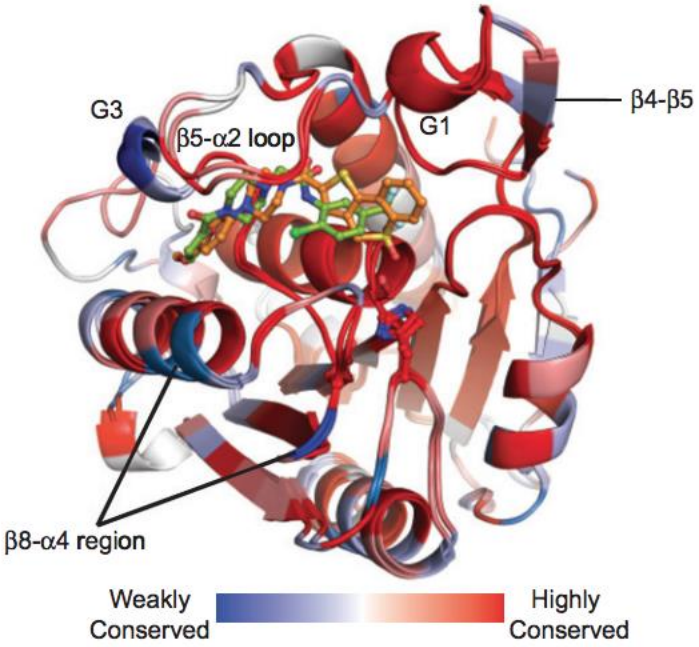

Figure 1.5 Divergence in APT1 and APT2 structures.

Blue regions signify divergence between APT1 and APT2. Adapted from Won et al., 2016.[103]

APT1 and APT2 feature unusual α/β serine hydrolase fold where the first β1 strand in the 'canonical' fold is missing and the fourth α-helix is replaced by a short α-helical segment termed G3. These enzymes include unique insertions, which add the short β4-β5 sheet and the β5-α2 loop. This loop contributes to forming a relatively long channel flanking the catalytic triad of both enzymes. Comparison of apoAPT1, APT1•ML348, and APT2•ML349 revealed this loop has varying degrees of openness, suggesting dynamic movement may engage various substrates. This feature functionally replaces the 'cap' or 'lid' domain found in many lipases, contributing to substrate engagement and providing thermodynamically stable environment for the catalysis. Both ML348 and ML349 make unique interactions with the divergent residues along this channel (**Figure 1.6**). However, these residues are either protruding away from the core of the protein (I76/M79, Q83/P86) or are similar in characteristics (eg. I75/L78). Importantly, mutational analysis identified a single residue I75/L78 (APT1/APT2) that establishes steric constraints to impart isoform selective inhibition.

Similarly, the residues within the loop of the catalytic D174/176 does not show obvious differences. Other divergent residues in the G3 helix show marginal contributions to inhibitor selectivity, potentially by constraining the dynamics of the β5-α2 loop.

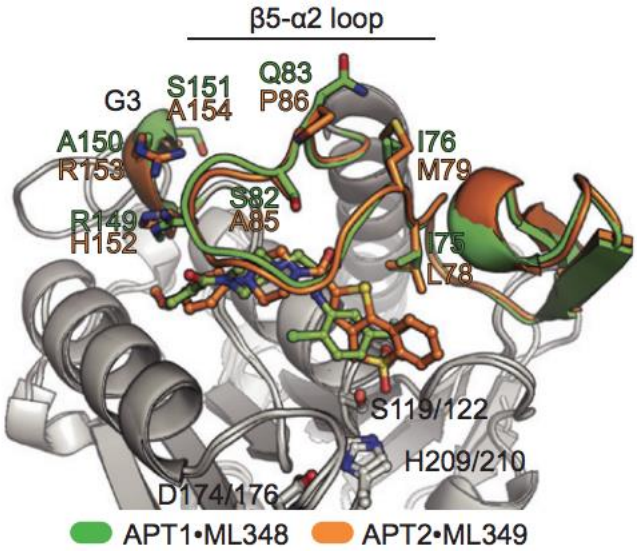

Figure 1.6 Isoform-selective inhibitor binding in APT1 and APT2.

Alignment demonstrates inhibitor engagement spanning along a hydrophobic channel towards the catalytic triad. Select residues are highlighted with sequence divergence between APT1 and APT2. Adapted from Won et al., 2016.[103]

The β5-α2 loop and the surrounding residues around the active site form a hydrophobic channel, that may enhance the entry and engagement of hydrophobic substrates. While it is tempting to think that peptide component of substrates might occupy the channel, docking simulations further support exclusive acyl chain occupancy. As further evidence, ML349-fluorescein binding to APT2 is blocked by pre-treatment with palmitic acid. Together with the observed 10ºC thermal stabilization upon HDFP engagement, we hypothesize long chain fatty acyl substrates bind in the channel, locking the substrate to promote ester hydrolysis. The channel and residues in proximity are probably not involved in the selectivity of the enzymes towards palmitoylated substrates, but rather select for acyl chain length through stabilization of the β5-α2 loop. Of note, the structures of both APT1•ML348, and APT2•ML349 lack the first few N-terminal residues. Since APT enzymes may be *S*-palmitoylated themselves at the N-terminus, it remains unclear how this may influence hydrophobic channel orientation and engagement of palmitoylated substrates. However, APT enzymes are largely

soluble present in the cytosol, so we predict APTs may only be fractionally *S*-palmitoylated.

Our structural analysis of APT1 and APT2 reveal strikingly similar substrate binding regions and surface polarity, and only conservative mutations across the enzyme active site (**Figure 1.7**). ML348 and ML349 are isoform selective apparently by coincidence and not by evolutionary selection in substrate discrimination. Therefore, any specific biological roles for each enzyme may be due to distinct protein-protein interactions, post-translational processing, differential expression, or distinct subcellular localizations. This raises several questions, such as why would evolution keep two isoforms of APT enzymes? What imparts the functional divergence between APT enzymes? Although these enzymes share nearly 70% identity, overexpression and knockdown studies clearly show preferences for specific palmitoylated substrates. One explanation could be the large difference in melting temperatures between isoforms, which suggest APT2 is more flexible and may be able to accept more diverse substrates than APT1. Furthermore, the single acyl binding channel explains the reduced activity towards diacylated substrates, and emphasizes a potential role for APT enzymes as general esterases for long-chain monoacylated substrates, including lysophospholipids, *S*-palmitoylated proteins, and prostaglandin glycerol esters. Overall, structural analysis of APT1 and APT2 do not provide a definitive explanation of how these enzymes are functionally divergent.

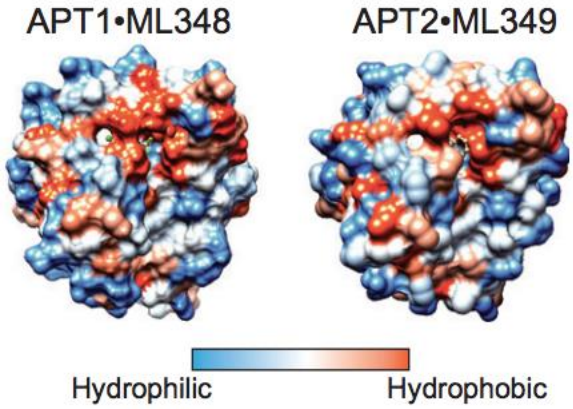

Figure 1.7 Surface polarity of APT1 and APT2.

Both APT1 and APT2 have similar surface polarity, with similar distributions of polar and hydrophobic surfaces.

ABHD17 family thioesterases

Until recently, APT1 was recognized as the primary depalmitoylase in cells, yet mutants in yeast, *Drosophila,* and *C. elegans* have no reported phenotypes. Given that APT1 was initially described as the primary depalmitoylase regulating N-Ras activity, this was quite puzzling. Cracks in this model began to appear throughout a number of publications, most strikingly from evidence that H-Ras depalmitoylase activity was exclusively in insoluble cell fraction (P100), and not with APT1 in the soluble fraction (S100).[105] Later, APT1/2 knockdown was shown to have no effect on R7BP depalmitoylation, while treatment with Palmostatin B or HDFP both blocked activity.[77] This was followed by detailed activity-based profiling of Palmostatin B targets, and the realization that Palmostatin B is broadly reactive across a number of candidate depalmitoylases.[79] Clearly other depalmitoylase activities beyond APT1/APT2 are present in cells, and likely contribute to the depalmitoylation of plasma membrane localized targets, including Ras.

In order to identify these additional depalmitoylases, Palmostatin B targeted hydrolases were over-expressed and *S*-palmitoylation turnover was assayed using 17-ODYA pulse-chase methods. This led to the identification of ABHD17 enzymes as candidate N-Ras depalmitoylases in COS-7 cells.[79] Over-expression of catalytic dead enzyme or N-terminal truncated mutants did not affect the N-Ras palmitoylation cycle, confirming ABHD17 enzymes are functional depalmitoylases in cells. ABHD17 hydrolases (ABHD17A, ABHD17B, and ABHD17C) are broadly expressed in all vertebrates, and harbor multiple conserved cysteines near their N-termini (**Figure 1.8A**). The N-terminal cysteine rich domain is essential for both *S*-palmitoylation and plasma membrane association.[34] Thus, ABHD17 enzymes are themselves *S*-palmitoylated, which is necessary for plasma membrane association and proximity to other *S*-palmitoylated proteins (**Figure 1.8B**). Importantly, deletion of the N-terminal cysteine rich domain has no effect on ABHD17 reactivity with fluorophosphonate activity-based probes, suggesting the palmitoylation motif is primarily responsible for directing membrane localization and does not influence enzyme activity. ABHD17A over-expression shifted N-Ras localization from the plasma membrane to internal membranes, indicative of more rapid *S*-palmitoylation turnover. Triple ABHD17 (A-C)

knockdown stabilized N-Ras 17-ODYA labeling, while APT1/APT2 inhibition with ML348 and ML348 had no effect. Accordingly, ABHD17 enzymes (but not APT1/APT2) contribute to N-Ras depalmitoylation in cells.

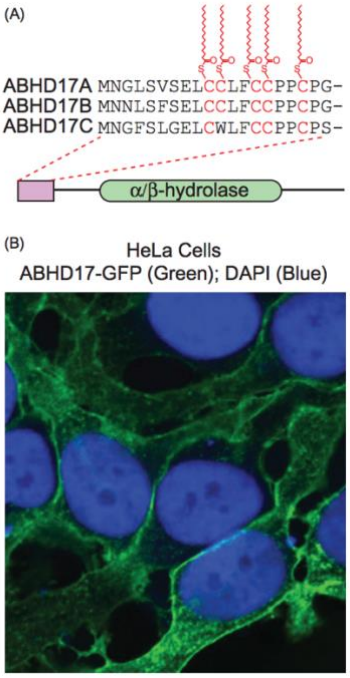

Figure 1.8 ABHD17 enzymes are palmitoylated and localize to the plasma membrane.

(A) ABHD17A-C are S-palmitoylated in a conserved N-terminal cysteine-rich motif separate from alpha-beta hydrolase domain. (B) ABHD17A-GFP localization in HeLa cells demonstrates predominant plasma membrane localization.

The synaptic protein PSD-95 is rapidly de-palmitoylated after depolarization. In order to identify the PSD-95 depalmitoylase, a panel of serine hydrolases were individually co-expressed with PSD-95 in 293T and COS-7 cells.[74, 106] Over-expressed ABHD17 enzymes efficiently depalmitoylated PSD-95 in 293T, COS-7, and primary neuronal cultures, while other Palmostatin B targets ABHD12, ABHD13, APT1, and APT2 had only fractional reductions in PSD-95 *S*-palmitoylation (**Figure 1.9**). ABHD17 over-expression reduced the synaptic clusters of PSD-95 and AMPA receptors in neurons, while ABHD17A/ABHD17B/ABHD17C knockdown stabilized palmitoylated PSD-95 and prevented the decrease in synaptic PSD-95 clustering. In addition, ABHD17 overexpression in primary neurons reduces the *S*-palmitoylation of microtubule-associated protein 6 (MAP6), causing MAP6 retention in axons and microtubule stability.[106] Recently the international knockout mouse consortium identified

ABHD17A as one of the top suppressors of distal cancer metastasis in mice[107] suggesting it may play a role in immune cell activation or surveillance.

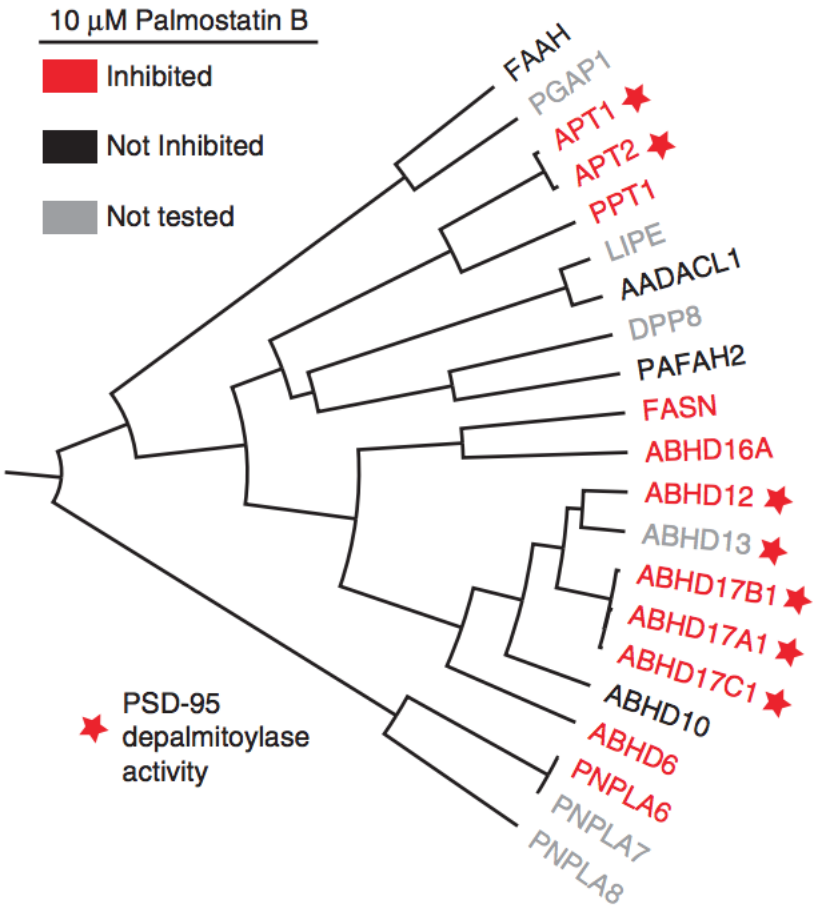

Figure 1.9 Homology, depalmitoylase activity, and Palmostatin B inhibition of HDFP-sensitive serine hydrolases.

HDFP-sensitive serine hyrolases reported from mouse B-cell hybridoma cells[28] are shown based on active-site anchored homology. Palmostatin B targets are highlighted in red. [79, 108] Enzymes that reduced PSD-95 S-palmitoylation after over-expression are labeled with a red star.[74]

Despite this growing number of cell-based ABHD17 studies, there is no biochemical evidence demonstrating *in vitro* depalmitoylation, enzyme kinetics, substrate specificity, or other functional properties of each ABHD17 enzyme. ABHD17 enzymes may hydrolyze other lipid substrates, particularly since their plasma membrane association delivers them in proximity to a number of potential substrates. A reported biochemical high throughput screen identified moderately potent inhibitors of an N-terminal truncated ABHD17B protein, yet these inhibitors failed to inhibit full-length, mammalian cell expressed protein (National Center for Biotechnology

Information. PubChem BioAssay Database; AID=2200). Structural studies are clearly necessary to understand if the N-terminal 100 amino acids before the conserved α/β-hydrolase domain function solely as a platform for *S*-palmitoylation and membrane tethering, or if they impart additional structural features important for substrate engagement. Clearly future efforts are needed to explore the substrate profile, redundancy between isoforms, and physiological roles for each ABHD17 enzymes.

Conclusions

Cycles of *S*-palmitoylation and depalmitoylation provide a mechanism for membrane sampling and trafficking of peripheral membrane proteins to the plasma membrane. Such directional palmitoylation cycles are demonstrated for G proteins, Ras, Scrib, and other central regulators of cell growth and organization. G protein internalization occurs even in the presence of generic depalmitoylation inhibitors, demonstrating that while depalmitoylation may be necessary for plasma membrane trafficking, agonist-dependent internalization occurs independent of depalmitoylation.[23] Based on these findings, many peripheral membrane proteins require cycles of *S*-palmitoylation and depalmitoylation for plasma membrane delivery, but there are no definitive examples of post-translational regulation of depalmitoylation activity. Rather, depalmitoylation appears to depend more on sub-cellular localization and regulated expression. ABHD17 enzymes localize to the plasma membrane, where they have direct access to neuronal scaffolding proteins and growth regulators. APT enzymes are soluble, and largely cytoplasmic, and play active roles in maintaining the directional palmitoylation cycle important for peripheral membrane protein trafficking.

Future efforts to understand regulation of depalmitoylation will continue to leverage emerging chemical and genetic technologies. While Palmostatin B and HDFP are useful generic inhibitors of depalmitoylases, selective inhibitors of APT enzymes should now be routinely used to individually perturb each APT isoform. These reagents will be valuable for parsing how APT1 and APT2 function either independently or in conjunction to influence distinct cellular outcomes. Future efforts are needed to validate APT1 and APT2 localization, interaction partners, and modifications to fully understand the divergent phenotypes. This would be greatly accelerated by knockout animal

models, allowing detailed biochemical and phenotypic analysis for each APT enzyme in their native physiological environments.

Similarly, ABHD17 enzymes are largely unannotated, and without biochemical analysis, it is not clear if each of the three enzymes are *bona fide* depalmitoylases or if each isoform carries out unique cellular functions. Clearly, ABHD17A plays a major role in suppressing growth of distal metastases, which likely reflects a role in immune regulation. Surely there are additional depalmitoylating enzymes, whether as their primary biochemical role or through non-specific acyl-thioester hydrolysis. Furthermore, Palmostatin B and HDFP likely act though polypharmacology, inhibiting a number of depalmitoylase (or lipase) enzyme activities to affect global depalmitoylation dynamics. Further functional studies of other hydrolases are likely to add to the growing number of factors contributing depalmitoylation dynamics in cells.

Finally, with the emergence of novel depalmitoylating enzymes, it is important to annotate the substrate profile and functional regulation by each enzyme. For example, cells could be treated with ML348 or ML349 to profile differential enrichment by mass spectrometry. Such experiments may be complicated by compensatory mechanisms, requiring simultaneous inhibition across a panel of depalmitoylases. Current enrichment and mass spectrometry detection methods are either indirect (Acyl-RAC) or require non-physiological metabolic labeling (17-ODYA). Since current liquid chromatography methods are optimized for polar peptides, future efforts are needed to extend quantitative proteomics to more hydrophobic peptides, allowing direct analysis of the modified peptide and the specific acyl chain. This could readily be accomplished by changing the column resin or adapting the mobile phase composition. Investment in sample preparation methods to optimize acyl-thioester stability, separation, ionization, and fragmentation have not been explored outside of single peptide measurements. In addition, multiplexed quantitative proteomics has emerged as a promising approach for time-dependent analyses, providing multiple measurements in a single combined proteomics experiment. We anticipate that ongoing advances in sample preparation and analysis will ultimately resolve many unanswered questions, providing a direct approach to profile the hydrophobic proteome and enzyme regulation.

Individual contributions

Sang Joon Won and Brent Martin wrote general overview and APT section. Melanie Cheung See Kit and Brent Martin wrote ABHD17 section. Sang Joon Won, Brent Martin and Melanie Cheung See Kit made figures.

Chapter 2 : Molecular Mechanism for Isoform-selective Inhibition of Acyl Protein Thioesterases 1 and 2 (APT1 and APT2)[†]

Abstract

Post-translational S-palmitoylation directs the trafficking and membrane localization of hundreds of cellular proteins, often involving a coordinated palmitoylation cycle that requires both protein acyl transferases (PATs) and acyl protein thioesterases (APTs) to actively redistribute S-palmitoylated proteins toward different cellular membrane compartments. This process is necessary for the trafficking and oncogenic signaling of S-palmitoylated Ras isoforms, and potentially many peripheral membrane proteins. The depalmitoylating enzymes APT1 and APT2 are separately conserved in all vertebrates, suggesting unique functional roles for each enzyme. The recent discovery of the APT isoform-selective inhibitors ML348 and ML349 has opened new possibilities to probe the function of each enzyme, yet it remains unclear how each inhibitor achieves orthogonal inhibition. Herein, we report the high-resolution structure of human APT2 in complex with ML349 (1.64 Å), as well as the complementary structure of human APT1 bound to ML348 (1.55 Å) (**Figure 2.1**). Although the overall peptide backbone structures are nearly identical, each inhibitor adopts a distinct conformation within each active site. In APT1, the trifluoromethyl group of ML348 is positioned above the catalytic triad, but in APT2, the sulfonyl group of ML349 forms hydrogen bonds with active site resident waters to indirectly engage the catalytic triad and oxyanion hole. Reciprocal mutagenesis and activity profiling revealed several differing residues surrounding the active site that serve as critical gatekeepers for isoform accessibility and dynamics. Structural and biochemical analysis suggests the inhibitors occupy a putative acyl-binding region, establishing the mechanism for isoform-specific inhibition, hydrolysis of acyl substrates, and structural orthogonality important for future probe development.

[†] This chapter presents a published peer reviewed article. Won S.J. et al *ACS Chem Biol.* 2017 Jan 19;24(1):87-97

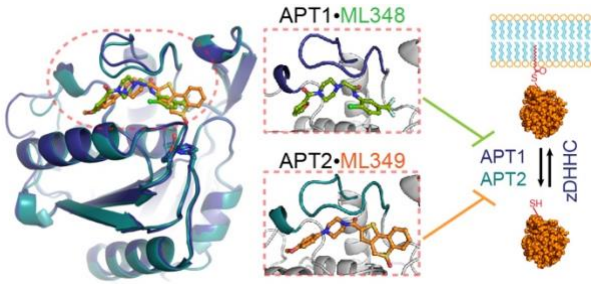

Figure 2.1 Graphical abstract.

Introduction

Post-translational S-palmitoylation anchors target proteins to membranes using a high-energy thioester, which can be readily hydrolyzed by enzymes or other cellular nucleophiles. In contrast, stable modifications like N-myristoylation and S-prenylation modify proteins via an amide or thioether linkage. Thus, while some proteins evolved as targets of stable lipidation, others use reversible membrane anchors for dynamic spatial regulation. Indeed, blocking Ras palmitoylation attenuates growth signaling and transformation in mutant cells.[26] Similarly, G proteins are rapidly depalmitoylated following activation,[25] potentially redistributing active signaling proteins to attenuate signaling. While such rapid depalmitoylation events may be enzyme-mediated, signal-dependent conformational changes could still be necessary to expose the S-palmitoylated cysteine to promote enzymatic hydrolysis.

The first characterized cytosolic protein depalmitoylase, acyl protein thioesterase (APT1/LYPLA1), was identified biochemically from rat liver.[58] Although it was previously annotated as a lysophospholipase,[109] both rat and yeast APT1 exhibit >65-fold to >2000-fold greater catalytic efficiencies (k_{cat}/K_m) as a $G_s\alpha$ protein depalmitoylase,[110,111] respectively. Rat and yeast APT1 were each shown to catalyze the depalmitoylation of $G_i\alpha_1$ (N-myristoylated and S-palmitoylated) 10-fold to 70-fold faster than Ras (S-farnesylated and S-palmitoylated),[111] respectively, demonstrating that the enzyme can discriminate between different S-palmitoylated substrates. Nevertheless, thioester hydrolysis is significantly more exergonic than ester hydrolysis, which likely accounts for the majority of rate acceleration. APT2 (LYPLA2) shares 68% protein sequence identity with APT1[64] and displays similar Ras depalmitoylase and lysophospholipase activity *in*

vitro.[64,59] While APT1 and APT2 likely share many common substrates, in cellular assays only APT2 affects the palmitoylation of GAP-43,[112] while only APT1 participates in the depalmitoylation of BK potassium channels[113] and the melanoma adhesion molecule (MCAM).[51] However, these observed isoform-specific activities could also represent differential overexpression, knockdown, or subcellular localization in each model. Overall, many studies of protein depalmitoylation rely on the dual APT1/APT2 inhibitor Palmostatin B,[61] which obscures the contributions from each individual enzyme. Nonetheless, dual APT1/APT2 inhibition disrupts overexpressed Ras trafficking and reverts certain malignant phenotypes.[61]

Later screening efforts identified piperazine amide competitive inhibitors with exquisite selectivity for APT1 and APT2[82,81,83] (**Figure 2.2 a**). The APT1 inhibitor ML348 and the APT2 inhibitor ML349 are isoform-selective and relatively potent ($K_i \leq 300$ nM) and exhibit orthogonality beyond the solubility of each probe.[83] Because both inhibitors incorporate a common piperazine amide linked to a five-membered hetero- cycle (thiophene or furan), each was hypothesized to occupy a similar position in the active-site.[100] Since there is no reported structure of APT2, the structural elements that impart inhibitor orthogonality and substrate selectivity have remained elusive. Here, we present the cocrystal structures of APT1 and APT2 binding to their respective selective inhibitors. Surprisingly, neither inhibitor directly hydrogen bonds to amino acid side chains but rather coordinates structural waters and occludes access to the catalytic residues. Mutagenesis along the β5-α2 loop and the G3 helix revealed the basis for inhibitor selectivity, which involves several residues that influence distinct loop conformations between APT1 and APT2. These elements engage each inhibitor, forming a hydrophobic fatty acyl-binding channel adjacent to the catalytic triad. Overall, these findings provide mechanistic insight into isoform-selective substrate specificity and reveal new directions for inhibitor optimization.

Results

Co-crystal Structures of APT1·ML348 and APT2· ML349. Differential scanning fluorimetry indicates a ~5 °C higher melting temperature (T_m) in APT1 (59.2 °C) relative to APT2 (54.4 °C; **Figure 2.2 b**). Thus, crystallization could be disfavored by additional

disorder in APT2. Upon ligand binding, both APT1 and APT2 are stabilized by 3.5−3.7 °C. Similar values were measured using a thermal shift assay, where heat denaturation and centrifugation are used to monitor protein solubility[114] (**Figure 2.2 C**). Again, APT1 is more thermally stable than APT2 by 4 °C, and inhibitor engagement considerably impedes denaturation.

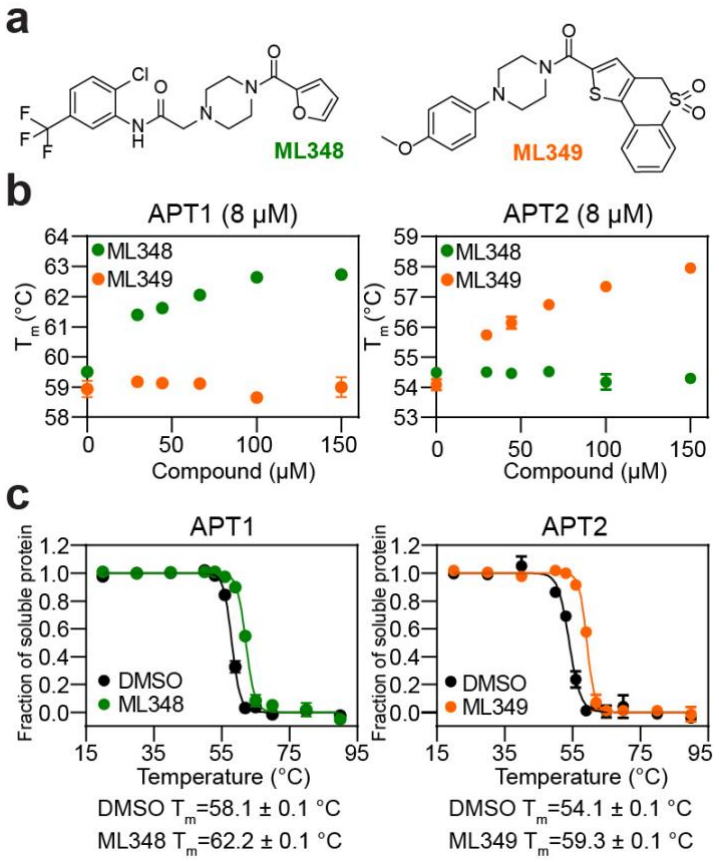

Figure 2.2 Stabilization of APT1 and APT2 by isoform-selective inhibitors.

(a) Chemical structures of ML348 and ML349. (b) ML348 and ML349 impart dose-dependent thermal stabilization of APT1 and APT2, respectively, by differential scanning fluorimetry. (c) Thermal shift assay corroborates thermal stabilization of APT enzymes by selective ligands.

Using this information, we readily obtained cocrystals of both APT1·ML348 and APT2·ML349. The structure of APT2 has not been reported, and therefore obtaining this model was critical for understanding the origins of inhibitor selectivity. Atomic structures of APT1·ML348 and APT2·ML349 were subsequently determined at 1.55 Å and 1.64 Å resolution, respectively (**Table 2.1**). Although a previously reported APT1 structure implied formation of a weak dimer,[104] both APT1·ML348 and APT2·ML349 form distinct

dimer interfaces in each respective asymmetric unit, suggesting that oligomerization is likely an artifact of crystallization.

Table 2.1 Crystallography data collection and refinement statistics

data collection	APT1·ML348	APT2·ML349
PDB code	5SYM	5SYN
space group	$P22_12_1$	$C2$
unit cell dimensions		
a, b, c (Å)	71.7, 73.7, 81.8	78.2, 79.8, 138.6
α, β, γ (deg)	$\alpha = \beta = \gamma = 90°$	$\alpha = \gamma = 90°, \beta = 93.3°$
wavelength (Å)	0.9792	0.9786
resolution (Å)[a]	35.84−1.55 (1.57−1.55)	55.81−1.64 (1.67−1.64)
R_{merge}	0.057 (0.42)	0.095 (0.488)
$I/\sigma(I)$[b]	18.5 (4.2)	7.1 (2.0)
completeness (%)[c]	100 (100)	93.2 (84.5)
redundancy	8.1 (7.8)	3.7(2.9)
refinement		
resolution (Å)	1.55	1.64
R_{work}	0.18	0.22
R_{free}	0.20	0.25
monomers/ASU	2	4
protein atoms	6888	6615
heterogen atoms	108	236
water molecules	363	310
unique reflections	63533	97049
RMS deviations		
bonds	0.009	0.01
angles (deg)	1.09	1.06
MolProbability score	0.84	1.08

[a]Statistics for highest resolution bin of reflections in parenthesis. [b]Intensity signal-to-noise ratio. [c]Completeness of the unique diffraction data.

Each APT structure adopts an atypical α/β hydrolase fold featuring a central, seven-stranded, mostly parallel β-sheet, corresponding to strands β1−β3 and β6−β9, surrounded by variable lengths of loops, helices, and strands (**Figure 2.3 a, b**). In both enzymes, the nucleophilic serine (APT1-Ser199/APT2- Ser122) assumes the typical strained conformation at the apex of the elbow between β6 and α3, whereas the histidine base (APT1-His209/APT2-His210) and aspartate (APT1-Asp174/ APT2-Asp176) are positioned on nearby extended loops between β9 and α5 and β8 and α4, respectively. APT1 and APT2 include noncanonical insertions of an antiparallel β4−β5 sheet, the corresponding β5−α2 loop, and a short G1 helix. Furthermore, both enzymes replace the fourth α-helix of the canonical fold with a short helical segment, termed G3,

which is structurally divergent between the APT1·ML348 and APT2·ML349 structures, and an additional short helix in APT2, termed G4.

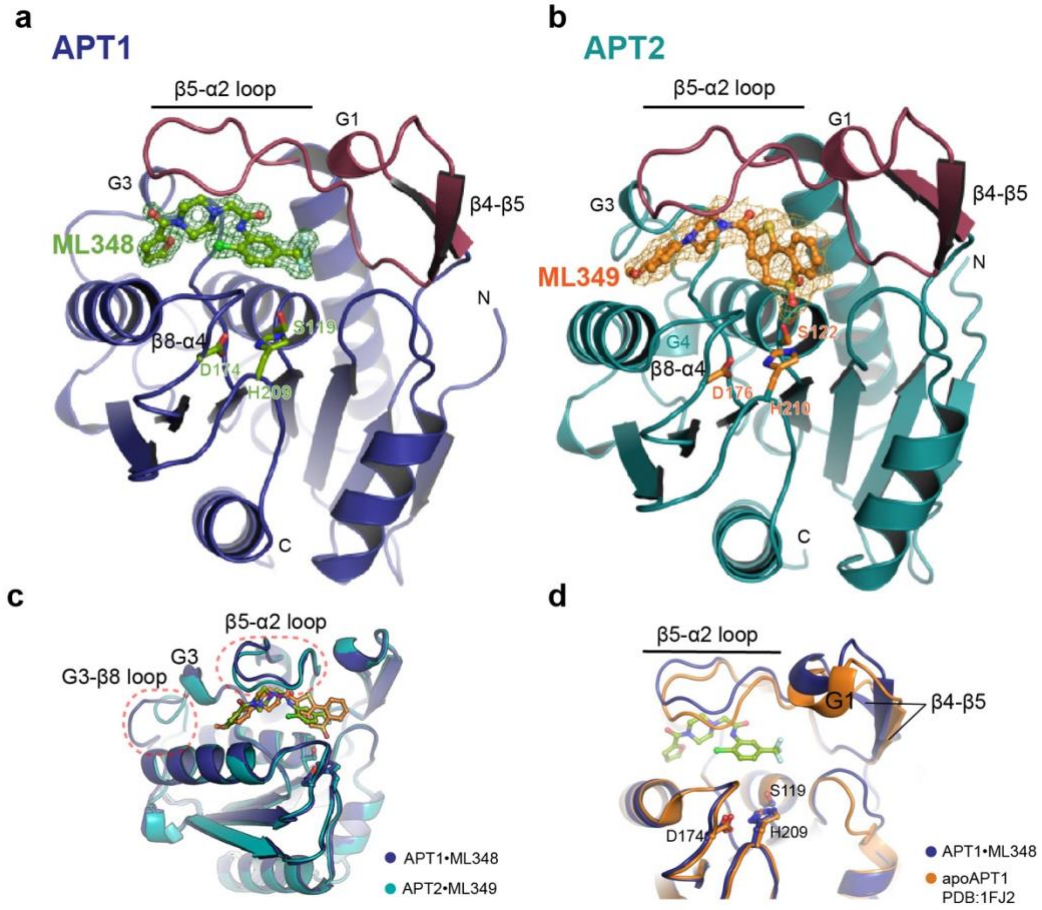

Figure 2.3 Conformational changes induced upon ligand binding revealed by co-crystal structures of APT1•ML348 and APT2•ML349.

(a) Co-crystal structure of APT1·ML348. A 2 σ omit map is shown for ML348. The catalytic triad is indicated in sticks, and the noncanonical β4-β5 sheet, the G1 helix, and the β5-α2 loop are colored purple (b) Co-crystal structure of APT2·ML349. A 2 σ omit map is shown for ML349, where the catalytic triad is indicated in sticks. Other features highlighted in APT1·ML348 are colored in purple. (c) Structure alignment of APT1·ML348 and APT2·ML349. Regions of significant conformational differences are shown in red-dotted circles. (d) Structural variance of APT1 (PDB: 1FJ2) in orange and APT1· ML348 in dark blue. Significant conformation changes are observed for the G1 helix, β4−β5 stands, and β5−α2 loop.

Unlike other α/β hydrolase lipases, APT homologues lack a distinctive “cap” domain important for substrate binding and a flexible “lid” that protects the active site from solvent. Instead, APTs may use the β5−α2 loop, which is flanked on one side by a G1/β8−α4 loop and a G3 helix on the other to form a relatively long (~20 Å) putative acyl-binding channel wherein both ML348 and ML349 reside. This hydrophobic channel shows varying degrees of openness between APT1, APT1· ML348, and APT2·ML349

(**Figures 2.3 c,d and 2.4**). In the distant bacterial homologue FTT258 (PDB: 4F21), the analogous loop domain demonstrates dynamic conformational changes proposed to define the active and inactive states, suggesting the loop closes upon substrate binding to initiate hydrolysis.[115] However, this substrate driven conformational change could differ among APTs, especially because the shorter G1 helix and the noncanonical β4−β5 sheet replace this loop in all vertebrate APTs (**Figure 2.5 a, b**). Although part of β4 and G1 pack with the β5−α2 loop to form one end of the channel, the overall functional role of the β4−β5 sheet and G1 motif remains speculative. The resulting hydrophobic channel has sufficient space and polarity to accommodate long chain fatty acyl chains. Because APT enzymes are more active toward long chain fatty acyl substrates,[116] shorter acyl chains may not provide enough free energy to counteract the entropic penalty of binding (increasing K_m) or bind too deep in the channel. Either would impede substrate orientation and activity. In comparison to the unbound structure, ML348 binding pushes out the β5−α2 loop, suggesting loop flexibility in this noncanonical region likely contributes to inhibitor engagement.

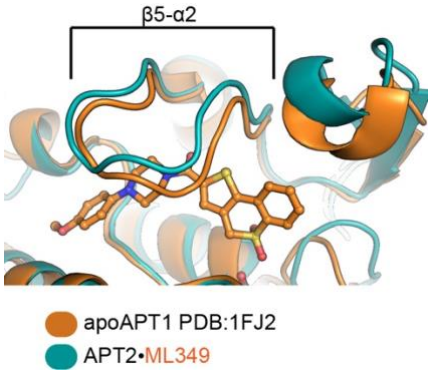

Figure 2.4 APT1 (PDB: 1FJ2) alignment with APT2•ML349.

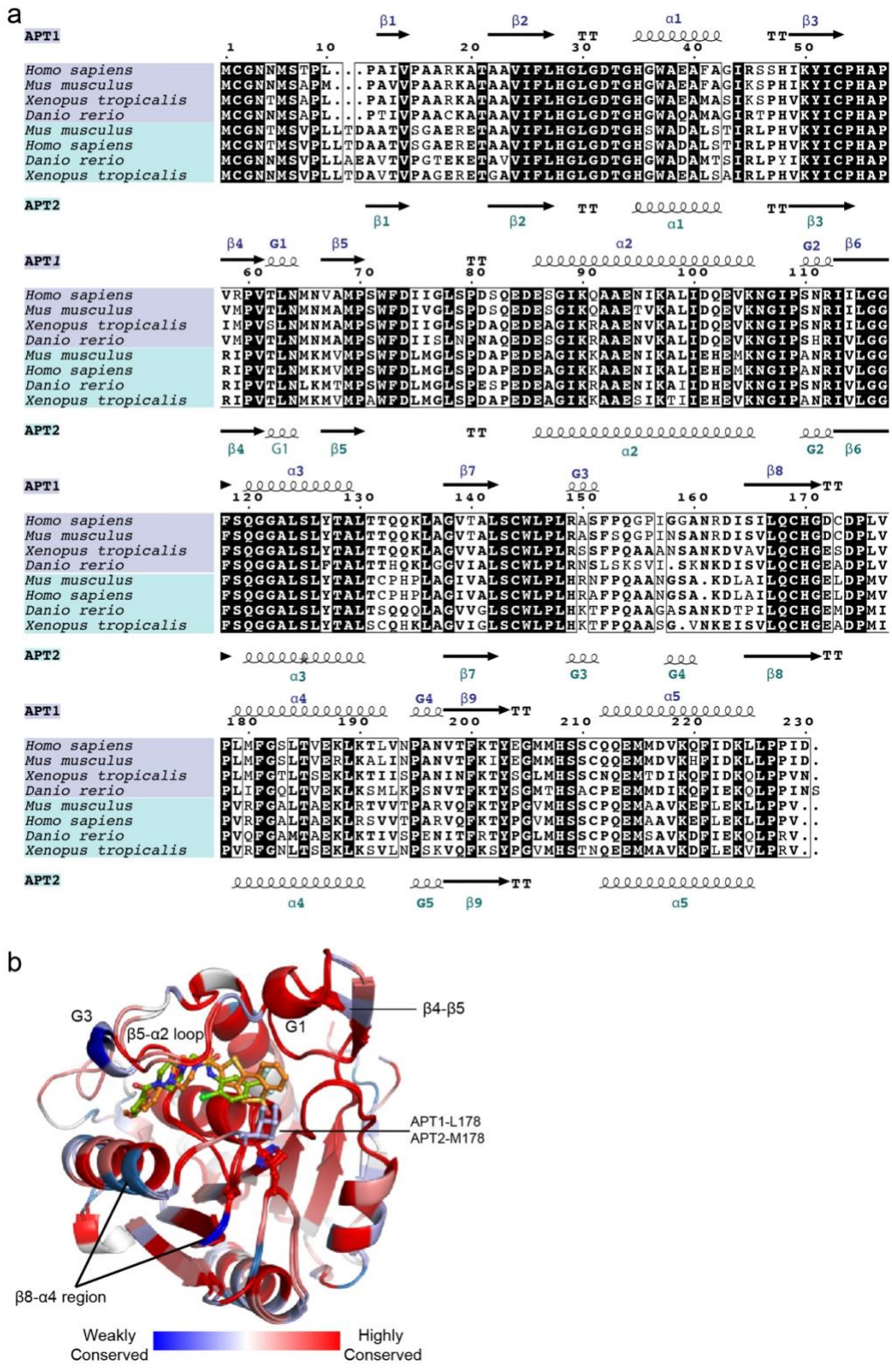

Figure 2.5 Sequence alignment and conservation across vertebrate APT enzymes.

(a) Sequence and secondary structure alignment of APT enzymes. Human APT1·ML348 and human APT2·ML349 were used to define secondary structures. (b) Cartoon model of APT enzymes rendered using UCSF-Chimera to

determine the degree of conservation. Blue regions signify divergence between APT1 and APT2, highlighting APT1-L176M and APT2-M178L (in sticks) in the β8/α4 region.

Structural Features of ML348 and ML349 Engagement. In the structure of APT1·ML348, two waters form hydrogen bonds to the anilide carbonyl, whereas in APT2 the same waters interact with the piperazine amide carbonyl (**Figures 2.6 a,d**). Clearly, the piperazine amide carbonyls of ML348 and ML349 motifs interact differently in each enzyme, showing no clear structure−activity relationship shared between APT1 and APT2.[81-83] Regardless, the bulk of both ML348 and ML349 molecules occupy the hydrophobic channel where their water-coordinated carbonyl groups are superimposed. One of these waters forms a hydrogen bond to the backbone carbonyl of APT1-Gln83/APT2-Pro86 and the backbone amide of APT1-Gly77/APT2-Met79, whereas the second forms hydrogen bonds to APT1-Glu84/APT2-Glu87. In addition, APT1-Trp145/APT2-Trp148 forms putative π−π stacking interactions with the aromatic anilide of ML348 and the thiophene of ML349. On the other end, APT1-Phe181/ APT2-Phe183 also forms a π−π stacking interaction between the ML348 furanyl group and ML349 anisole group.

The G3 helix has weak sequence similarity between APT1 and APT2, suggesting it may be a site of functional divergence (**Figure 2.5 a, b**). In APT1, Arg149 of G3 forms a hydrogen bond with a water molecule that coordinates the ML348 piperazinyl amide carbonyl and the Pro80 backbone carbonyl in the β5−α2 loop (**Figure 2.7 a**). In contrast, His152 in the APT2 G3 helix forms a π−π stacking with the ML349 anisole group, and Arg153 forms a hydrogen bond with the Asp84 side chain of the β5−α2 loop (**Figure 2.7 b**). Most importantly, both the anilide ring of ML348 and the thiochromene heterocycle of ML349 are positioned directly above the catalytic triad, blocking substrate access. The ML348 trifluoromethyl substituent passively blocks the catalytic triad through a series of hydrophobic contacts, including those with Leu30, Leu176, and the hinge residue Ile75. In contrast, the ML349 sulfone group participates in a hydrogen bond network with water molecules, making indirect contacts with both the oxyanion hole and the catalytic triad (**Figures 2.6 a−d**).

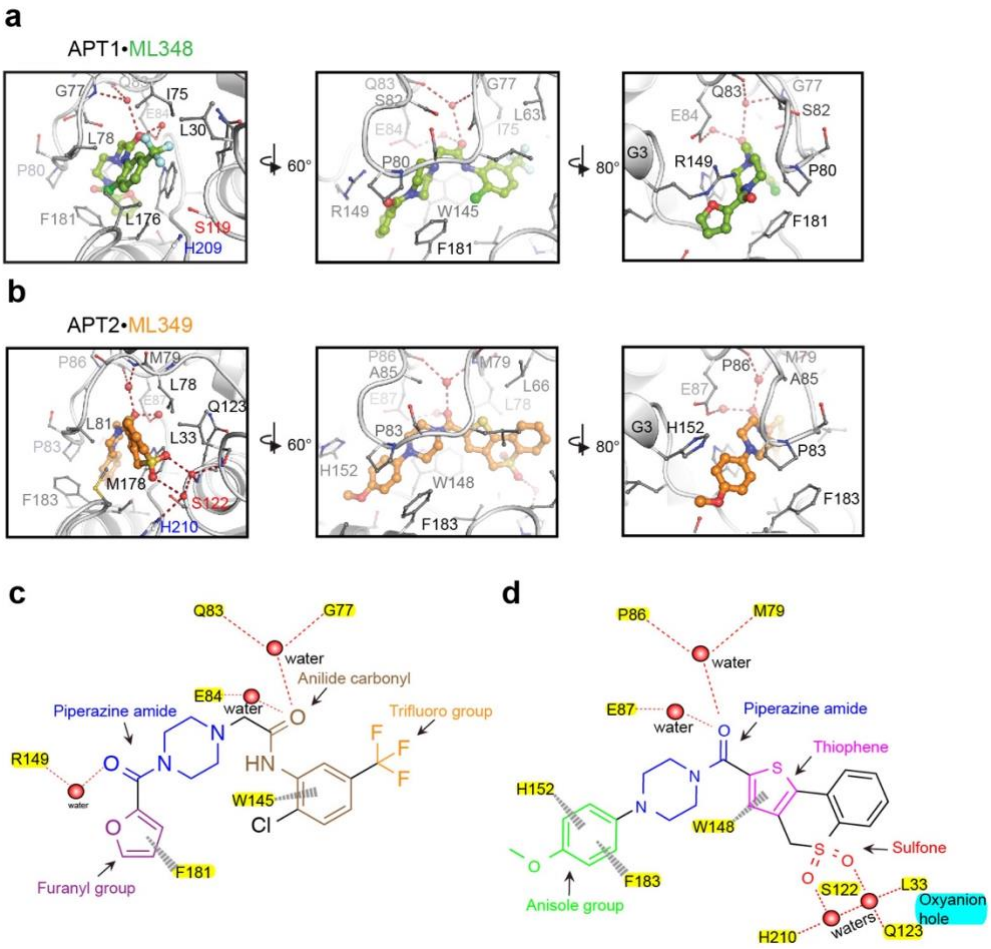

Figure 2.6 Inhibitor binding in APT1 and APT2 promoted by distinct binding modes.

(a) The hydrophobic channel of the APT1·ML348 complex from different perspectives. Side chains of residues within 3.5 Å of ML348 (green) are shown as gray sticks. Water molecules are shown as red spheres and hydrogen bonds by red dotted lines. (b) The hydrophobic channel of the APT2·ML349 complex from different perspectives. Side chains of residues within 3.5 Å of ML349 (orange) are shown in gray sticks, with similar notation for waters and hydrogen bonds. (c) Two-dimensional ligand plot of ML348 interactions with APT1. Red dashed lines represent hydrogen bonds, and gray dashed lines indicate π−π stacking interactions. Chemical features are color coded and labeled. (d) Two-dimensional ligand plot of ML349 with corresponding labels as described in c.

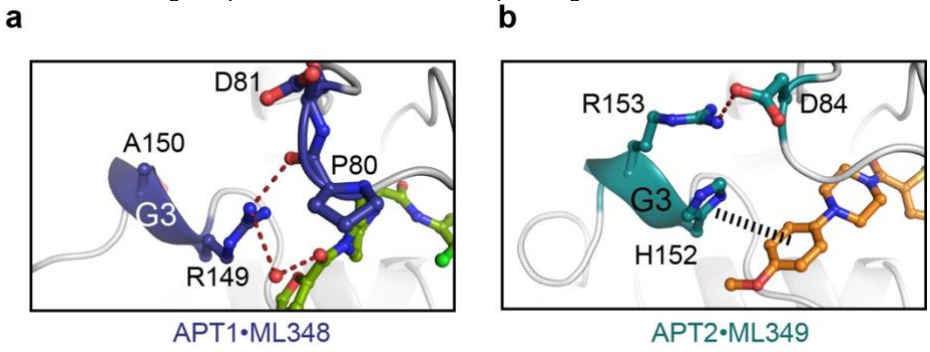

Figure 2.7 The G3 helix interacts with the β5-α2 loop.

(a) The APT1 G3 helix interacts with ML348 and the β5-α2 loop. (b) The APT2 G3 helix interacts with ML349 and β5-α2 loop, through both hydrogen bonding (red dashed lines) and a π−π stacking (black dashed lines)

At first glance, we initially hypothesized the ML349 sulfone might act as a tetrahedral transition state inhibitor since the sulfonyl group of ML349 is in proximity to the catalytic residues Ser122, His210, and the oxyanion hole backbone carbonyl oxygens of Gln123 and Leu33 (**Figure 2.6 b, d**). On closer analysis, ML349 appears to form indirect hydrogen bonds to APT2 via two intervening water molecules, each tethered by hydrogen bonds to the catalytic machinery in the active site. One water molecule forms a hydrogen bond to an oxyanion hole amide through its oxygen lone pair, while also serving as a hydrogen bond donor to an ML349 sulfone oxygen. The other water molecule is positioned near the histidine base (His210) where it would normally become polarized to participate in acyl-intermediate hydrolysis but instead forms a hydrogen bond to the other ML349 sulfone oxygen.

Next, we examined if the formation of the enzyme−inhibitor complex depends on the presence of the sulfonyl oxygens. A racemic ML349−sulfoxide derivative demonstrated some residual inhibition, but ML349−thioether completely lost any ability to bind APT2 (**Figures 2.8 b and 2.9 a, b and Table 2.2**). In order to test whether the serine nucleophile participates in ML349 binding, we synthesized an ML349−fluorescein (ML349−FL) conjugate to probe active site binding by fluorescence polarization, independent of substrate hydrolysis (**Figure 2.8 a**). Interestingly, both ML349 and the ML349−FL bind the catalytic dead APT2−S122A mutant with similar affinity (**Figures 2.8 a, b**), confirming Ser122 does not engage the thiochromene sulfone. Pretreatment with either ML349 or hexadecylfluorophosphonate (HDFP) blocked ML349-FL polarization with APT2, ruling out any alternative binding mechanisms while confirming overlap between HDFP and ML349 binding sites. Furthermore, both activity-based and fluorescence polarization competition studies confirmed that ML349 has at least 20-fold lower K_d than the racemic ML349−sulfoxide toward APT2, and no significant binding by ML349−thioether (**Figures 2.8 b and Table 2.2**).

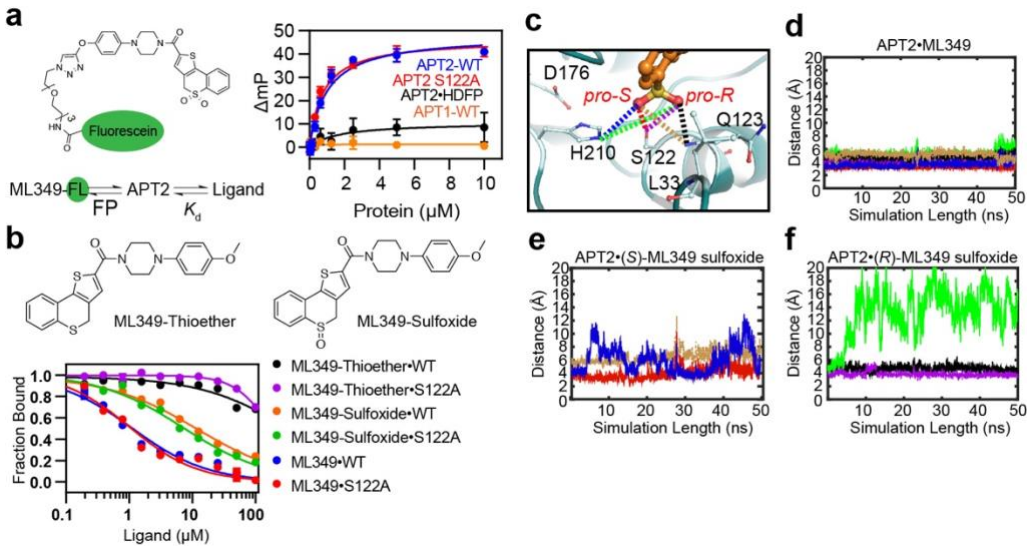

Figure 2.8 Catalytic triad and oxyanion hole of APT2 indirectly engaged by ML349.

(a) ML349−FL exhibits APT2-dependent fluorescence polarization. (b) Chemical structures of ML349 derivatives are shown above the dose-dependent ML349−FL displacement by ML349 derivatives in APT2 and APT2−S122A. (c) Structural representation of the S and R oxygen atoms comprising the ML349 sulfone group in APT2. Atomic distances are shown with dotted lines corresponding to the color schemes used to present the molecular dynamics simulations. Blue represents the distance from the His210 τ- nitrogen to ML349-S-oxygen. Brown represents the distance from the ML349-S-oxygen to Q123 backbone amide nitrogen. Red represents the distance from the ML349-S-oxygen to S122 oxygen. Green represents the distance from His210 τ-nitrogen to the ML349-R- oxygen. Black represents the distance from the ML349-R-oxygen to the Q123 backbone amide nitrogen. Purple represents the distance from the ML349-R-oxygen to the S122 oxygen. (d) Molecular dynamic simulation of APT2·ML349 demonstrates little active site fluctuation between the sulfone oxygens and catalytic triad. (e) Bound (S)-ML349-sulfoxide promotes flexibility of His210 to destabilize the active site. (f) Bound (R)-ML349-sulfoxide promotes even greater flexibility of His210, and similarly destabilizes the active site.

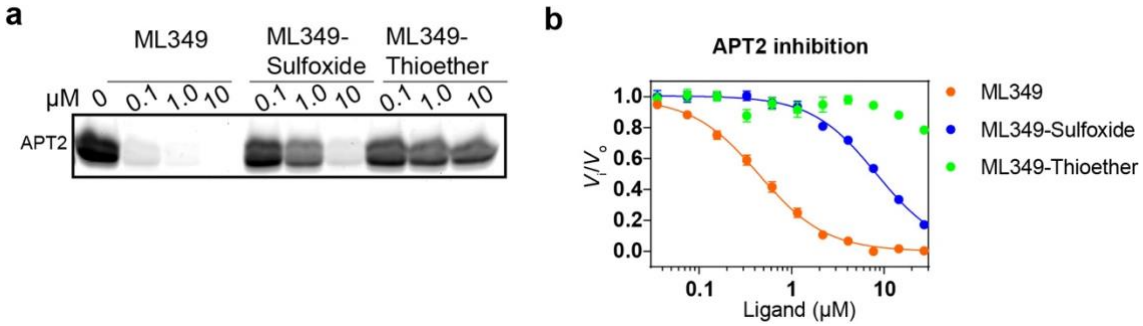

Figure 2.9 ML349 engagement with APT2 requires the thiochromene sulfone.

(a) FP-PEG-TAMRA competitive assay with ML349 derivatives. (b) APT2 binds sulfone variants with lower affinity, measured by ResOAc substrate hydrolysis assay.

Table 2.2 Binding affinity of ML349 derivatives determined from competitive ML349-FL fluorescent polarization

	APT2 WT		APT2 S122A	
Ligand	IC_{50} (μM)	K_d (nM)	IC_{50} (μM)	K_d (nM)
ML349-FL	—	1020	—	770
ML349	1.1	240	1.0	160
ML349-sulfoxide	12	5200	7.1	2600
ML349-thioether	>100	>10000	>100	>10000

Molecular Dynamics Simulations. To complement the characterization noted above, we carried out molecular dynamics simulations of the enzyme−ligand complexes to investigate how each sulfonyl oxygen of ML349 interacts in the presence of active site resident waters to stabilize the enzyme−inhibitor complex in comparison with sulfoxide variants. In order to monitor enzyme−inhibitor interactions, we constructed the distance between two designated atoms throughout the course of the simulated trajectories. These distances were displayed graphically over 50 ns periods from separate simulations for ML349 and the two in silico generated enantiomers (S)-ML349 sulfoxide (oxygen atom pointing toward His210) and (R)-ML349 sulfoxide (oxygen pointing toward oxyanion hole; **Figure 2.8c**). Whereas, the sulfonyl containing ML349 showed essentially no motion in the active site during our simulations, both (S)-ML349-sulfoxide and (R)- ML349-sulfoxide−enzyme simulations displayed increased fluctuations at His210 (**Figures 2.8d−f**). The (R)-ML349- sulfoxide showed significantly more fluctuation than the (S)- ML349-sulfoxide, suggesting the pro-(S) sulfone oxygen may play a more significant role in active site stabilization. All together, these simulations demonstrate how both sulfone oxygens of ML349 minimize disorder in the active site by indirectly engaging the catalytic residues through water- mediated hydrogen bonds and are consistent with the findings from the thermal denaturation and kinetic analysis.

The β5−α2 Loop and G3 Helix Are Responsible for Inhibitor Selectivity. APT1 and APT2 have only a few divergent residues in the ligand-binding region (**Figure 2.10a**). In order to examine whether these positions are responsible for functional discrimination between ML348 and ML349, we performed reciprocal site-directed mutagenesis between APT1 and APT2 at these sites and carried out steady-state kinetic assays with the fluorogenic substrate resorufin acetate (ResOAc)[83] (**Table 2.3** and **Figure 2.11**). As

confirmation of proper fold, essentially every reciprocal mutant displayed similar Km values except for APT1-L176M, which might be explained by its position close to the catalytic triad (**Figures 2.5b and 2.11a**). APT1-Ile75 (Leu78 in APT2) introduces a steric clash with the thiophene group of ML349 (**Figure 2.10b**) and may disrupt ML349 binding. Indeed, the APT1-I75L variant introduces a steric clash with the ML348 trifluoromethyl group. This clash reduces ML348 binding almost 10-fold (K_i = 2.2 μM) and enhances binding to ML349 (K_i = 370 nM). The analogous APT2−L78I mutant only partially mirrored the reversal observed in APT1−I75L, yielding measurable ML348 binding (K_i = 5.8 μM), but introduces a new steric clash at the ML349 thiophene sulfur to weaken ML349 binding. Thus, Ile75 and Leu78 play important roles in dictating selectivity, but these roles are distinct with each inhibitor.

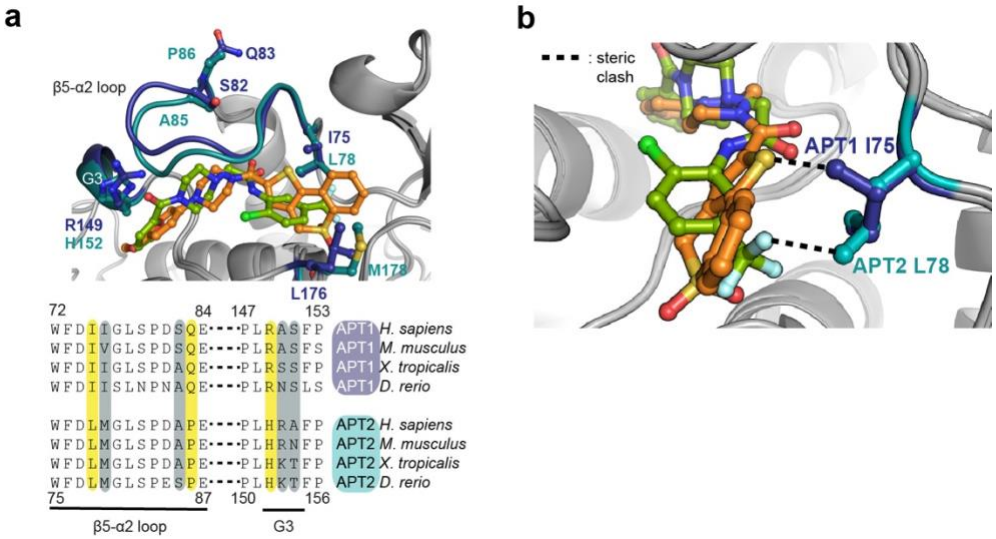

Figure 2.10 Inhibitor selectivity imparted by the divergent β5−α2 loop.

a) Structural view of divergent residues near the ligand-binding region. APT1 (dark blue) is shown bound to ML348 (green), and APT2 (teal) is shown bound to ML349 (orange). Homologous vertebrate sequences near the β5−α2 loop and G3 helix are shown, highlighting highly divergent (yellow) and less divergent (gray) residues that were selected for mutagenesis. (b) APT1-I75 and APT2-L78 contribute to inhibitor selectivity caused by isoform-selective steric clashes, high- lighted in black dashed lines.

Table 2.3 Summary of kinetic and inhibition parameters of APT reciprocal mutants using ResOAc substrate hydrolysis.

	Protein	K_M (μM) ResOAc	K_i (nM) ML348	K_i (nM) ML349
APT1	WT	18 ± 1	280 ± 33	>10000
	L176M	77 ± 1	340 ± 40	>10000
	Q83P	28 ± 1	370 ± 20	>10000
	I75L	23 ± 3	2200 ± 350	370 ± 70
	I75L/S82A/Q83P	24 ± 1	>10000	1200 ± 70
	I75L/S82A/Q83P R149H/A150R/S151A	25 ± 3	>10000	180 ± 10
APT2	WT	18 ± 2	>10000	120 ± 20
	M178L	19 ± 2	>10000	200 ± 20
	P86Q	32 ± 3	>10000	130 ± 10
	H152R	30 ± 1	>10000	660 ± 50
	L78I	19 ± 1	5800 ± 400	>10000
	L78I/A85S/P86Q	17 ± 1	3400 ± 260	>10000
	L78I/A85S/P86Q H152R/R153A/A154S	25 ± 1	430 ± 20	>10000

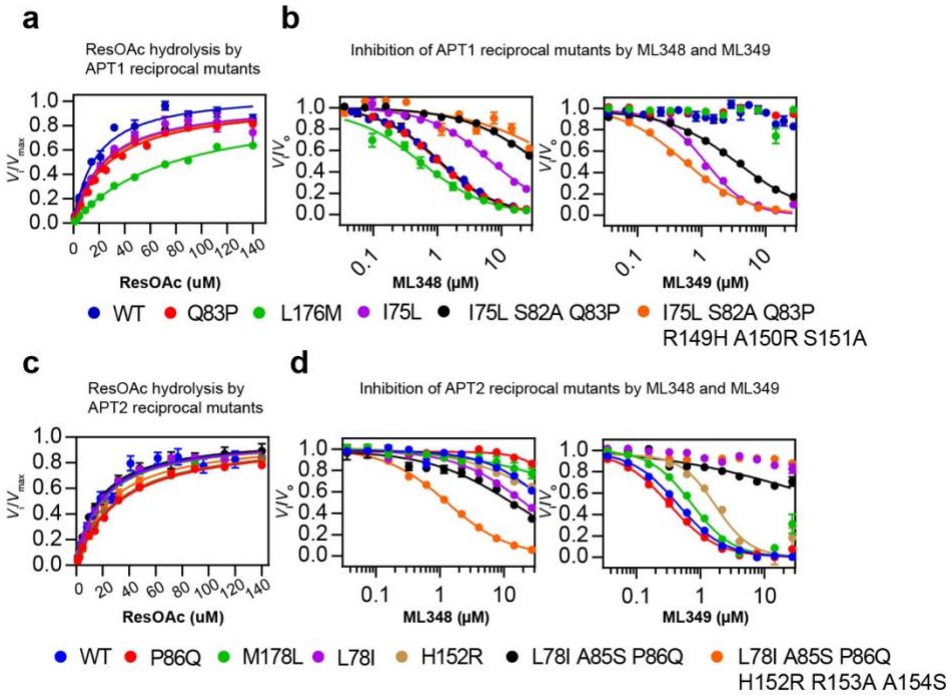

Figure 2.11 Reciprocal mutant sensitivity to ML348 and ML349.

(a) Steady-state ResOAc hydrolysis rates for APT1 mutants. (b) Reciprocal mutagenesis and inhibition of APT1 by ML348 and ML349. (c) Steady-state ResOAc hydrolysis rates for APT2 mutants. (d) Reciprocal mutagenesis and inhibition of APT2 by ML348 and ML349.

Since the reciprocal mutations at APT1-I75L/APT2-L78I do not fully reconstitute the observed potency and orthogonality of the wild type enzymes, synergistic residues were profiled by combining several reciprocal mutations. The triple APT1-I75L/ S82A/Q83P mutant completely abolished ML348 inhibition but showed weaker ML349 potency (K_i = 1.2 μM) compared to just the single I75L mutant (K_i = 370 nM). Since the APT1- Q83P mutation alone had no effect on selectivity, we examined if APT1-S82 cooperates with APT1-I75 to impart inhibitor orthogonality. Interestingly, the double mutant APT1-I75L/ S82A slightly improved ML348 and ML349 inhibition compared to APT1-I75L alone. The triple mutant APT1- I75L/S82A/Q83P no longer binds ML348 and loses significant potency for ML349. Taken together, these data demonstrate that the selectivity effect cannot be isolated to a single mutation, and S82A synergizes with Q83P to impact ML348 selectivity. Alternatively, the single APT2-P86Q and the double mutant APT2-L78I/A85S have essentially the same K_i values as either wild-type APT2 or APT2-L78I. Since the APT2 triple mutant L78I/A85S/P86Q improved ML348 potency, neither A85S nor P86Q by itself has much effect on preventing ML348 binding. As shown for APT1, the synergetic effect is observed when both residues are mutated together. Ultimately, switching the G3 helix between APT1 and APT2 led to the most robust selectivity reversal, where APT1-I75L/S82A/Q83P/R149H/A150R/S151A was potently inhibited by ML349 (K_i = 180 nM) and lost all potency for ML348. The reciprocal mutant APT2-L78I/A85S/P86Q/H152R/R153A/A154S was similarly inhibited by ML348 (K_i = 430 nM) and had no residual inhibition by ML349. Clearly, the G3 helix influences β5−α2 loop dynamics to differentially engage ML348 and ML349, through interactions with the ML348 piperazinyl amide and the ML349 methoxyphenyl ring. Altogether, these structural features form the basis for orthogonal inhibition through a combination of differential flexibility and steric constraints.

Substrates and Selective Inhibitors Engage a Common Acyl-Binding Pocket. On the basis of the arrangement of hydrophobic residues, we predict the acyl chain of native substrates lies in the same channel as ML348 and ML349. Interestingly, HDFP increased the T_m of each APT enzyme by over 10 °C (**Figure 2.12**), suggesting lipid engagement provides a major source of energetic stabilization that decreases the K_d for

long chain acyl substrates. To explore acyl engagement more directly, we performed product competition studies with ML349−FL. While oleic acid is competitive with ML349−FL binding, the observed IC_{50} value (9.9 ± 0.6 μM) is above the 6 μM critical micelle concentration (CMC) for the lipid (**Figure 2.13**).[117] Incubation with 1-oleoyl-2-hydroxy-*sn*-glycero-3-phosphocholine produced slightly more potent ML349−FL competition (IC_{50} = 4.3 ± 0.4 μM), although it also serves as a substrate and releases oleic acid. Interestingly, the catalytic dead APT2-S122A mutant showed no ML349−FL competition with 1-oleoyl-2-hydroxy-*sn*-glycero-3-phosphocholine. Thus, any competition is likely driven by released oleic acid upon lysophosphatidylcholine hydrolysis, and subject to the same potential micellar affects. To overcome this experimental obstacle, we directly assayed acyl binding using the environmentally sensitive acyl-fluorophore BODIPY-FL-C16, which exhibits increased fluorescence in nonpolar environments.[118] A constant, submicellar concentration of BODIPY-FL-C16 was incubated with increasing concentrations of each enzyme, reporting dose-dependent, saturable fluorescence enhancement with APT1 (K_d =2.5 ±0.5 μM) and APT2 (K_d =2.8 ±0.5 μM; **Figure 2.14a**). Furthermore, BODIPY-FL-C16 exhibited a dose-dependent reduction in fluorescence after the addition of ML348 in APT1 or ML349 in APT2, further supporting competition for the enclosed acyl-binding pocket (**Figure 2.14 b, c**). Although the precise BODIPY-FL-C16 orientation and binding mode are unknown, this assay confirms BODIPY engagement to a nonpolar site displaced selectively in each APT isoform by its corresponding competitive inhibitor.

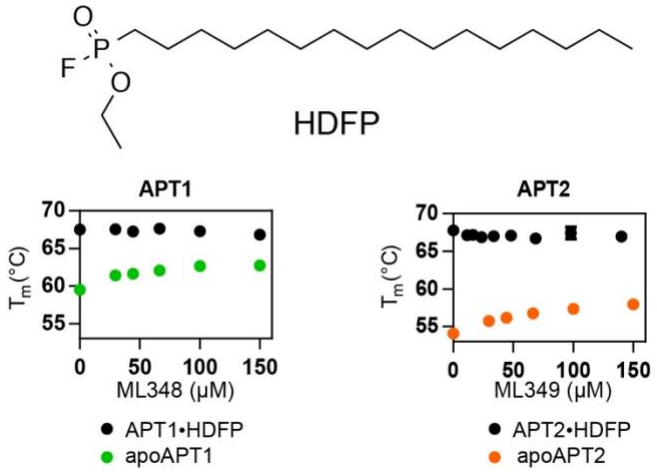

Figure 2.12 Thermal stabilization of APT1 and APT2 by HDFP.

(a) Structure of the covalent lipase inhibitor HDFP. (b) APT1 and APT2 pre-incubated with HDFP stabilizes each protein (ΔT_m >10 °C) by differential scanning fluorimetry (thermofluor). Further titration of ML348 or ML349 had no additive effect on the observed ΔT_m. Stabilization of APT1 by ML348 (green) and APT2 by ML349 (orange) are shown as a reference.

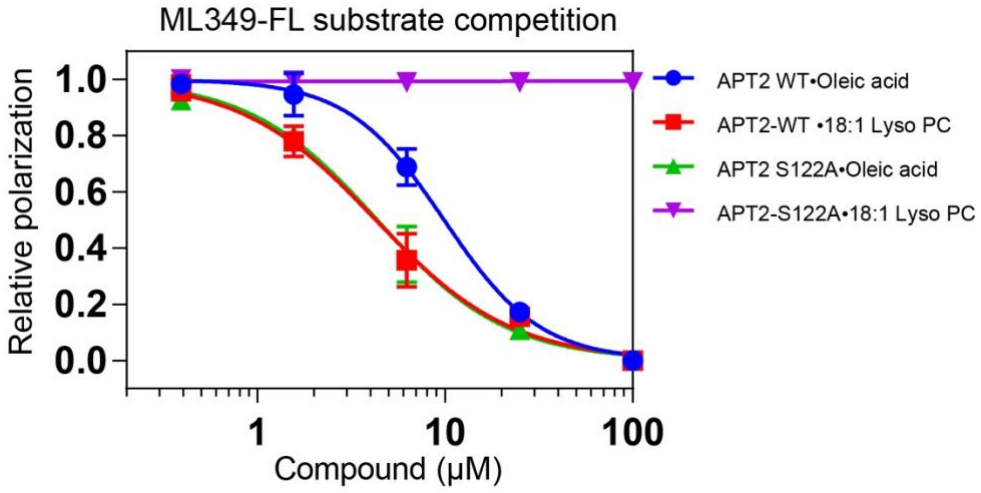

Figure 2.13 ML349-FL fluorescence polarization with APT2 is attenuated by fatty acid

APT2 fluorescence polarization with ML349-FL was measured after equilibration for 30 minutes with oleic acid or (18:1) lysophosphatidylcholine (Lyso PC). APT2-S122A was not affected by lyso PC, suggesting oleic acid product binding.

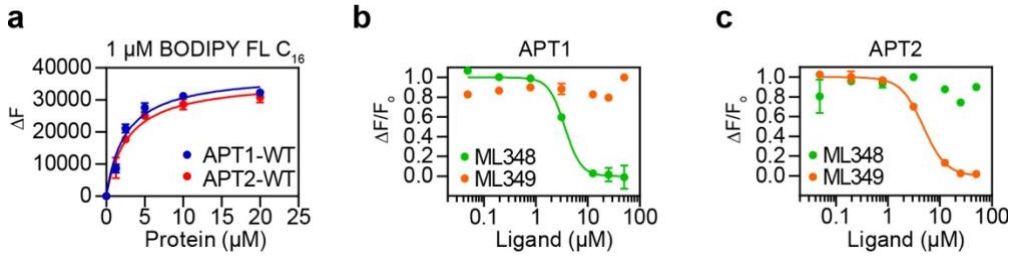

Figure 2.14 Isoform-selective inhibitors displace submicellar fluorescent lipids.

(a) APT enzymes enhance BODIPY-FL-C16 fluorescence. (b) BODIPY- FL-C16 competition with ML348 and ML349 against APT1. (c) BODIPY- FL-C16 competition with ML348 and ML349 against APT2.

Discussion

APT1 and APT2 are broadly invoked whenever describing the dynamic turnover of S-palmitoylation on proteins.[100] While ML348 and ML349 superficially share a common piperazinyl amide chemotype, our high-resolution structural analyses reveal distinct binding modes that block access to the catalytic triad and occlude the putative acyl-binding pocket. Ligand engagement by a hydrophobic channel is not surprising, since APT1 and APT2 react exceptionally fast with aliphatic fluorophosphonate probes

and HDFP, and much slower with polar, PEG-fluorophosphonate probes.[28, 83] The potent dual APT1/APT2 inhibitor Palmostatin B also incorporates a 10-carbon chain,[61] reinforcing the benefit conferred by an acyl binding element.

On the basis of structural and sequence alignment of APTs across vertebrates, any determinants promoting functional orthogonality between APT1 and APT2 are not immediately obvious (**Figure 2.5**). Several studies suggest that APT1 and APT2 harbor intrinsic substrate preferences,[112, 113] and clearly APT1 and APT2 possess sufficient structural variance to enable isoform-selective inhibition. Herein we carried out reciprocal mutagenesis at divergent residues distal from the catalytic triad, revealing functional differences affecting inhibitor engagement. Although definitive evidence supporting the precise mode of acyl group engagement will require further crystallographic analysis, our current biochemical competition data demonstrate that each isoform-selective inhibitor occludes acyl engagement across the nonpolar channel, which likely forms upon substrate engagement by the closure of the β5−α2 loop. Alternatively, the acyl group could potentially occupy the shallow groove contiguous along the catalytic site and acyl-binding pocket (**Figure 2.15**). Since this groove is largely solvent exposed with mixed polarity, it more likely helps dock lysophospholipid head groups or the palmitoylated protein domains. While this model is intuitive, any functional role for the adjacent groove will require further biochemical studies, potentially after HDFP inactivation. However, part of the β8/α4 region also features several divergent residues closer to the active site. These additional residues could cooperate in substrate acquisition, supporting additional investigation to dissect further functional divergence. Overall, the observed inhibitor orthogonality is solely derived from the acyl-binding channel, thus any substrate selectivity beyond acyl-chain selection is more likely promoted through distal sites not engaged by either ML348 or ML349.

On the basis of the structural models presented, we speculate that APT enzymes primarily hydrolyze substrates with reduced membrane partitioning, including lysophospholipids, prostaglandin esters, or singly S-palmitoylated substrates. Further S-acylation of each APT enzyme likely localizes the enzyme in close proximity to membrane-bound substrates, thereby enhancing substrate acquisition and relative activity. Following substrate recruitment and acyl engagement, we propose that the

β5−α2 loop closes to encapsulate the nonpolar acyl chain, providing significant enzyme stabilization to drive polar coordination of the acyl thioester. Additional interactions may further align the peptide, culminating in the thioester hydrolysis and subsequent release of product. This model readily accommodates S-palmitoylated sites near the protein termini or disordered regions, allowing the peptide and acyl chain to thread along the contiguous groove. Dually lipidated proteins, such as N-myristoylated and S-palmitoylated Lck and $G_i\alpha_1$, may require additional rearrangements to engage the active site. Here, the N-myristoyl group could expand the binding pocket by shifting the flexible β5−α2 loop to accommodate both lipids, or one acyl group could remain engaged in the membrane and thread next to the β4−β5 sheets and G1 helix. Deciphering the precise mechanism of substrate engagement will likely require additional structural analysis, potentially capturing native substrates with a catalytic dead enzyme, or through the design of tailored fluorophosphonate probes to mimic acylated peptide substrates.

Overall, the structures of APT1·ML348 and APT2·ML349 show highly similar active sites with distinct inhibitor conformations despite a related chemotype. Inhibitor selectivity depends on distinct residues lining a divergent flexible loop, reminiscent of the lid domain of related bacterial hydrolases.[115] More potent inhibitors may be optimized to directly engage each protein, potentially by displacing active site waters, or through extended engagement of the shallow proximal groove. Furthermore, we report the unique sulfonyl-engagement of ML349 by APT2, suggesting further exploration of sulfonyl functional groups when optimizing active site-directed reversible hydrolase inhibitors. Ultimately, this structural analysis highlights the subtle differences between APT1 and APT2 leveraged by ML348 and ML349, which will provide value in future studies profiling the physiological function and substrates of each enzyme across both lipidated peptides and metabolites.

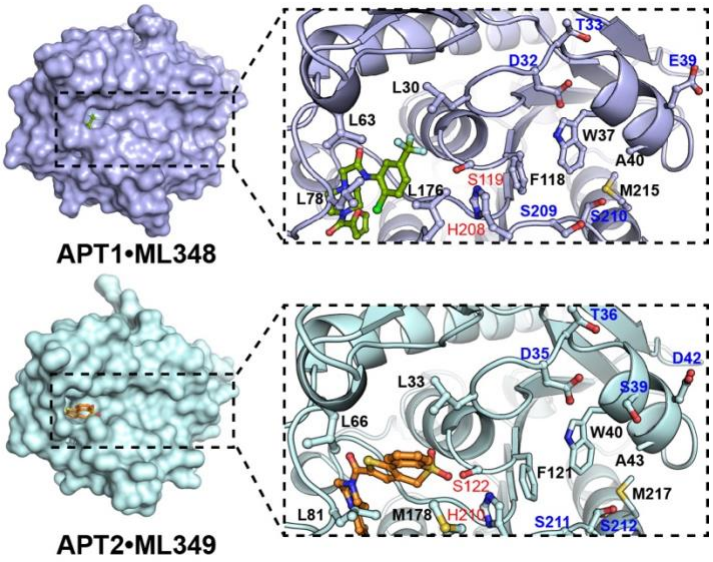

Figure 2.15 ML348 and ML348 are adjacent to a contiguous groove.

Surface rendering of APTs reveal a shallow groove contiguous from the active site. The opening of the channel and the residues that line the center in both structures are formed by hydrophobic residues (black font). Polar residues that line the groove are highlighted in blue.

Materials and Methods

Protein Expression, Purification, and Crystallization. APT1 and APT2 genes were amplified from human 239T cell cDNA and inserted into pMCSG7 to introduce an in-frame N-terminal polyhistidine tag for expression. BL21 (DE3) *E. coli* (Novagen) cultures (OD_{600} = 0.6) were induced with 0.5 mM IPTG for 16 h at 25 °C. Cell pellets were resuspended in 50 mM HEPES at pH 7.8, 300 mM NaCl, and 10% glycerol; sonicated; and centrifuged at 35000g for 30 min. Talon cobalt affinity beads (Clontech) were incubated with the cleared supernatant for 1 h and then washed with 50 mM HEPES at pH 7.8, 150 mM NaCl, and 1 mM imidazole buffer. The proteins were eluted with 50 mM HEPES, 150 mM NaCl, and 150 mM imidazole buffer. The eluted samples were dialyzed overnight in the presence of TEV protease to remove excess imidazole and to cleave the HisTag, yielding ~10 mg mL^{-1} of protein. Protein samples were supplemented with 20% glycerol and stored at −80 °C. For crystallization, protein stock solutions preincubated with inhibitors were prepared at 8 mg mL^{-1} and supplemented with 5 mM dithiothreitol (DTT). APT1 was incubated with 3 mM ML348, and APT2 was incubated with 1 mM ML349 for at least 1 h at 4 °C before setting crystal trays for

incubation at 20 °C. Crystals were produced by sitting drop vapor diffusion with drops containing 2 μL of enzyme− inhibitor complex and 2 μL of reservoir solution. For APT1·ML348, the best-diffracting crystals were formed from reservoir solution containing 0.1 M sodium citrate at pH 5.5, 22−24% PEG 3350, and 200 mM MgCl2. For APT2·ML349, the best-diffracting crystals were formed from reservoir solution containing 0.1 mM sodium citrate at pH 5.5 and 20−24% PEG 3350. Larger, better diffracting crystals were formed by microseeding 1 day after setup. After 1−2 weeks, thin plate crystals formed. Reservoir solution was supplemented with 25% ethylene glycol for cryopreservation.

Data Collection and Structure Determination. Diffraction data for APT1·ML348 and APT2·ML349 were collected on the Advanced Photon Source LS-CAT beamlines 21-ID-D and 21-ID-G, respectively. The data were processed with MOSFLM[119] and scaled with SCALA.[120] APT1·ML348 was solved to 1.55 Å resolution by molecular replacement using MOLREP[121] with the A chain of APT1 (PDB ID: 1FJ2) as the search model. The structure of APT2·ML349 was solved to 1.64 Å resolution by molecular replacement via Balbes,[122] which also used the APT1 structure as the search model. Both structures went through iterative rounds of manual electron density fitting and structural refinement in Coot[123] and Buster.[124] Difference electron density maps contoured at 2σ showed the presence of an inhibitor associated with each protein chain. Coordinates and restraint files for each ligand were created by grade[124] with the mogul+qm option. Data collection and refinement statistics for each structure are listed in **Table 2.1**. Figures were generated using the PyMol Molecular Graphics system (Schrödinger). Atomic coordinates for APT1·ML348 and APT2·ML349 have been deposited in the PDB as entries 5SYM and 5SYN, respectively.

General chemical synthesis and purification procedure.

Can be found in Appendix A.

Thermal denaturation assays. For thermal shift assays, 0.25 mg / mL of recombinant protein in Phosphate Buffered Saline (PBS) was incubated with 200 μM ligand for 30 minutes, heated to desired temperature for 3 minutes using a thermocycler (Bio-Rad), and incubated on ice. The tubes were spun at 20,000 x g for 20 minutes at 4 °C. The concentration of soluble protein was quantified with the DC Protein Assay kit (Bio-Rad).

For differential scanning fluorimetry assays, 0.2 mg / mL of protein in PBS was incubated with varying amounts of ligand for 30 minutes, followed by the addition of 1-anilinonaphthalene-8-sulfonic acid (ANS, ThermoFisher) to a final concentration of 0.2 mM. Samples were transferred to a black 384-well PCR plate (Axygen, 384-55-BK) and 1.5 µL of silicon oil was added on top of each well. Plates were heated from 25 °C to 85 °C at 1 minute intervals and each condition was measured in quadruplicate using a ThermoFluor plate reader (Johnson & Johnson). The melting curves were analyzed by fitting to a Boltzmann model to determine T_m using ThermoFluor Acquire 3.0 software.

Steady-state kinetic assays. Assays were performed as previously described with modifications[83]. The K_m for resorufin acetate was determined for different APT mutants using resorufin acetate (Sigma). Assays were performed side-by-side with catalytic-dead enzyme (APT1-S119A, APT2-S122A) to subtract any spontaneous hydrolysis. Enzymes were diluted to 10 nM in PBS pH 6.5 (adjusted with sodium acetate) supplemented with 0.1 g / L pluronic F127 (Sigma). Varying concentrations of resorufin acetate (Sigma) in DMSO were added as 5 µL aliquots to clear-bottom 96-well plates (Greiner bio-one). Using a multi-channel pipette, 95 µL of enzyme was added to each well and quickly mixed by pipetting up and down several times. Each enzyme was assayed in 2 separate runs, each with 4 replicates per substrate concentration and 4 replicates of catalytic-dead enzyme. Fluorescence was measured every 35 seconds for 15 minutes on a Tecan F500 plate reader (525/35 nm excitation filter, 600/10 nm emission filter, and a 560 LP dichroic filter). Initial reaction velocities were calculated from the slope of the background-subtracted (catalytic dead) fluorescence in the first 5 minutes, and processed in Graphpad Prism 6 to derive K_m and V_{max}. Steady-state inhibitors IC_{50} values were calculated using a similar experimental scheme, starting by pre-incubating 10 nM enzyme with varying inhibitor concentrations for 30 minutes at room temperature. A fixed concentration of substrate (50 µM final) was aliquoted into each well and the reaction was initiated by the addition of the enzyme-inhibitor mixture and initial rates were measured. The data containing 8 replicates per inhibitor concentration was imported to Graphpad Prism 6 and a standard non-logarithmic sigmoidal dose response curve was fitted to each enzyme experiment. Each K_i value was calculated using Cheng-Prusoff equation.

Fluorophosphonate-TAMRA competitive assays. APT2 (200 nM) was incubated with varying concentrations of inhibitor in PBS pH 7.4 at room temperature for 30 minutes, and then mixed with 1 µM of FP-PEG-TAMRA for 10 minutes. The reaction was quenched by addition of Laemmli sample buffer and incubation at 90 °C for 5 minutes. The samples were resolved on 12% SDS-PAGE and visualized by Azure C600 imager.

Computational methods. Molecular dynamics simulations were performed using the CHARMM macromolecular modeling program[125], version c39b2, for APT2·ML349, APT2·ML349 (*R*-sulfoxide), and APT2·ML349 (*S*-sulfoxide). Dynamics were performed using the Leapfrog Verlet/Langevin integrator with a 2 fs timestep. A non-bonded cutoff range of 10-12 Å was used with a van der Waals switching function, where the non-bonded list was generated using a 15 Å cutoff. Long range electrostatic interactions were treated using the particle-mesh Ewald method[126], with a $\kappa = 0.56$ and an interpolation spline order of 4. Each simulation was heated to 310 K utilizing a Langevin heat bath for 100 ps, equilibrated for 100 ps, followed by a production run of 50 ns. In each simulation, the APT systems were simulated as a monomer. The CHARMM22 all-atom force field for proteins with CMAP correction[127] was used for the APT2 ML349 systems, and the CHARMM36 all-atom force field was used for the sulfoxide systems. Each system was solvated in a 13,793 TIP3P[128] water molecule box with periodic boundary conditions in a cubic volume of edge length 36 Å. Eighteen sodium chloride pairs and an additional sodium ion were added to the APT2 enzyme to give a net zero charge and an excess salt concentration of 0.1 M for each system. For ligand parameterization, ML349, ML349 (*R*-sulfoxide) and ML349 (*S*-sulfoxide) were assigned parameters and partial charges consistent with the CHARMM General Force Field (CGenFF)[129-132] using the CGenFF interface for ParamChem[129-132]. The most recent extension of the CGenFF force field covers sulfonyl-containing compounds with good agreement with experimental IR/NMR data, allowing for the assignment of parameters to ML349, and was implemented into MATCH Analysis. The distance between two defined atoms was calculated in VMD[133] and graphed using MATLAB.

Fluorescence binding assays. Varying amounts of enzyme were diluted in PBS supplemented with 0.5 g / L pluronic F127 and incubated with 500 nM ML349-FL for 30 minutes at room temperature. The fluorescent polarization from each well was

measured using a Tecan F500 plate reader using 485/20 nm excitation and 535/25 nm emission polarization filters. Each concentration was measured in 2 replicates. The background signal was subtracted to obtain Δ mP at each protein concentration and imported to Graphpad Prism 6.0 for one site-specific binding analysis. For dose-response fluorescent polarization, 1 µM of protein and 500 nM ML349-FL were incubated with varying amounts of ML349 derivatives for 30 minutes at room temperature. The standard non-logarithmic sigmoidal dose-response curve was used to derive IC_{50}. K_i was calculated using the online IC_{50} to K_i converter[134]. For BODIPY-FL-C_{16} binding assays, 1 µM of BODIPY FL C16 (ThermoFisher) was incubated with various concentrations of enzyme in PBS for 30 minutes. The relative fluorescence was performed as two independent replicates, and measured using Tecan F500 plate reader (485/20 nm excitation filter, 535/25 nm emission filter). After background subtraction, the data was processed in Graphpad Prism 6 for single site binding analysis. For competition assays, 5 µM APT, 1 µM BODIPY-FL-C_{16}, and varying concentration of ML348 or ML349 were incubated for 30 minutes in PBS and data was fit to a non-logarithmic sigmoidal dose response curve.

Acknowledgements

I would like to thank Prof. John Tesmer for critically reading the manuscript. Financial support for these studies was provided by the National Institutes of Health R00 CA151460, DP2 GM114848, the American Heart Association 14POST20420040 (to Dr. Majmudar), and the University of Michigan.

Individual contributions

Kristin Labby, Rachel Pricer, and Sang Joon Won prepared expression plasmids. Kristin Labby, Jasmine Palakurthi, Laura Rodriguez, Christina Rodriguez, and Sang Joon Won purified proteins. Fei San Chong, Edward Hur, Jaimine Majmudar, Kris Torossian, and Sang Joon Won synthesized inhibitors. Kristin Labby, Jasmine Palakurthi, and Jennifer Meager optimized crystallization conditions. Jennifer Meager and Jeanne Stucky collected X-ray data and determined structures. Sin Ye Hwang and Sang Joon Won

performed all inhibitor and enzyme assays. Kira Armacost. and Charlie Brooks. performed computational studies. Sang Joon Won and David Davda designed competition experiments. Kristin Labby, Sang Joon Won, David Davda, and Brent Martin designed other experiments. David Davda and Sang Joon Won analyzed inhibition data. Rachel Pricer and Sang Joon Won designed figures. Sang Joon Won, David Davda, and Brent Martin wrote the paper.

Chapter 3 : Affinity-based Selectivity Profiling of an In-class Selective Competitive Inhibitor of Acyl Protein Thioesterase 2[§]

Abstract

Activity-based protein profiling (ABPP) has revolutionized the discovery and optimization of active-site ligands across distinct enzyme families, providing a robust platform for in-class selectivity profiling. Nonetheless, this approach is less straightforward for profiling reversible inhibitors and does not access proteins outside the ABPP probe's target profile. While the active-site competitive acyl protein thioesterase 2 (APT2) inhibitor ML349 (K_i = 120 nM) is highly selective within the serine hydrolase enzyme family, it could still interact with other cellular targets. Here we present a chemoproteomic workflow to enrich and profile candidate ML349-binding proteins. In human cell lysates, biotinylated-ML349 enriches a recurring set of proteins, including metabolite kinases and flavin-dependent oxidoreductases that are potentially enhanced by avidity-driven multimeric interactions. Confirmatory assays by native mass spectrometry and fluorescence polarization quickly rank-ordered weak off-targets, providing justification to explore ligand interactions and stoichiometry beyond ABPP.

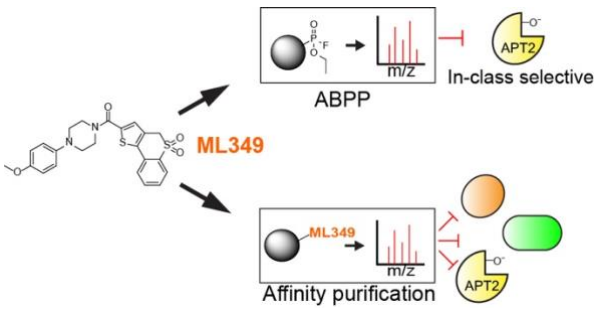

Figure 3.1 Graphical abstract

[§] This chapter presents a published peer reviewed work. Won S. J. et al *ACS Med Chem Lett.* 2016 Dec 9;8(2):215-220

Introduction

Medicinal chemistry efforts primarily focus on achieving the highest potency ligands, which in the best-case scenario obviates any off-target engagement. In practice, many lead inhibitors have suboptimal potency, leaving open the possibility of off-target binding to other enzymes. In order to validate selectivity, medicinal chemistry campaigns typically assess inhibition against related enzymes that share the same catalytic mechanism. Particularly for kinases, hydrolases, and proteases, this workflow can induce active-site competitive assays with reporter-linked covalent inhibitors.[135] For example, fluorophosphonate probe labeling is occluded when an inhibitor covalently modifies or otherwise occupies an active site. Such competitive activity-based protein profiling (ABPP) methods enable evaluation of both potency and in-class selectivity either by in-gel fluorescence or affinity purification for mass spectrometry profiling.

Across the serine hydrolase enzyme family, ABPP methods have supported the development of several mechanism-based covalent scaffolds, including N-heterocyclic ureas,[86] β-lactones,[61] and activated carbamates.[87, 136, 137] Since these scaffolds covalently modify their target enzymes, the competitive fluorophosphonate assay requires only enough probe and time to achieve complete labeling. Profiling reversible inhibitors is more complicated since each enzyme has a different rate of inactivation (K_{inact}), as well as different rates of inhibitor displacement (k_{off}).[83] Under such conditions, selectivity profiling is most representative of inhibition for enzymes with relatively slower K_{inact} constants, providing a kinetic window to profile target engagement. For example, the fluorophosphonate-TAMRA reacts extremely rapidly with acyl protein thioesterase 2 (APT2), which overwhelms much of the observable competition by the reversible active site inhibitor ML349.[83] This can be addressed by tailoring the reactivity of the ABPP probe, such as using a less reactive N-heterocyclic urea. In this example, intraperitoneal injection of ML349 was chased with an alkynyl N-heterocyclic urea probe in living mice, allowing assessment of *in vivo* target engagement and partial in-class selectivity from isolated tissue homogenates.[83]

Due to these limitations, in-class selectivity profiling can also be carried out using reversible ligands linked to an affinity resin. Such affinity purification approaches have been used for decades for target enrichment and identification, particularly when

coupled with quantitative shotgun proteomics methods. When adapted for on-bead competitive displacement assays, inhibitor selectivity can be quantitatively profiled for any enriched proteins. For example, a resin-linked kinase inhibitor cocktail (or kinome beads) allows multiplexed dose−response analysis of ligand selectivity across more than 200 enriched kinases.[138] In addition, such native enrichment approaches also capture accessory proteins, or in some cases totally orthogonal enzyme classes. Using this approach, imatinib was found to bind the oxidoreductase NQO2 6-fold stronger than BCR-ABL, establishing unanticipated off-targets outside the targeted kinase family.[138, 139] More recently, cellular thermal shift assays (CETSA),[114] drug affinity responsive target stability (DARTS),[140] or CRISPR genome-wide approaches[141] provide orthogonal routes to target discovery independent of affinity enrichment.

Here we evaluated the selectivity of the APT2 inhibitor ML349, comparing reported ABPP selectivity to traditional affinity-based target identification methods. APT2 is a widely expressed serine hydrolase with several reported substrates, including lysophospholipids,[64] prostaglandin esters,[65] and S-palmitoylated proteins.[61] The active site competitive APT2 inhibitor ML349 was first identified from a high-throughput competitive activity-based fluorophosphonate assay in collaboration with the NIH Molecular Libraries Production Centers Network.[81] Out of the 3 ×10^5 compounds tested, ML349 was identified as a promising competitive inhibitor with high selectivity across the serine hydrolase enzyme family. Even without further optimization, ML349 achieves target engagement and hydrolase selectivity in living mice.[83, 100]

ML349 was later validated to modulate protein *S*-palmitoylation in cells. The *S*-palmitoylated tumor suppressor Scribble (Scrib) localizes to the plasma membrane in polarized epithelial cells to attenuate growth signals and promote contact inhibition.[142] When polarized epithelial cells are induced to undergo epithelial-to-mesenchymal transition, Scrib relocates to the cytosol and is less *S*-palmitoylated.[75]Treatment with submicromolar concentrations of ML349 increase the *S*-palmitoylation and membrane localization of Scrib, restoring plasma membrane localization to attenuate growth signals.[75]As reported, ML349 only suppresses cell proliferation at significantly higher concentrations (100 × K_i), suggesting engagement of other potential off-target proteins.[75]In the crystal structure of APT2 bound to ML349 (1.6 Å), ML349 binds to a

hydrophobic channel extending across the enzyme active site, leaving only a solvent-exposed *p*-methoxy substituent to tether a reporter group.[103] Since cell proliferation is only inhibited at concentrations well beyond concentrations required for APT2 inhibition, we set out to functionalize ML349 at the *p*-methoxy position for affinity-guided off-target identification.

Using an affinity purification strategy, we annotated a reproducible series of enriched targets by mass spectrometry. Some of these target proteins were individually profiled by native mass spectrometry, providing a direct assessment of ligand stoichiometry and affinity,[143] particularly since several targets exist as homodimers. Confirmatory polarization assays with ML349-fluorescein ruled out other enriched targets, suggesting that resin avidity might enhance enrichment of otherwise low affinity targets. Overall, we report the target landscape of ML349, which includes APT2 and other weak cellular targets. Accordingly, while ABPP methods are streamlined for in-class selectivity of covalent inhibitors, classic ligand affinity purification methods access diverse cellular targets and circumvent potential false negatives missed in time-dependent competitive ABPP assays.

Results

Previous structure−activity analysis demonstrated that interchanging the ML349 methoxy group from the para to ortho position abolished APT2 inhibition.[83] Accordingly, we synthesized both *p*- and *o*-propargyl-ML349 derivatives and conjugated each to biotin-azide by copper catalyzed azide−alkyne cycloaddition (CuAAC) (**Figure 3.2a**). In a biochemical fluorogenic esterase assay, the *p*-substituted ML349-PEG3- biotin probe (ML349-biotin) lost approximately 9-fold affinity (K_i = 1100 nM), while the *o*-substituted probe (*o*-ML349- biotin) or the azide-PEG3-biotin linker alone were completely inactive (**Figure 3.2b**). Despite this reduction in affinity, we continued to explore if ML349-biotin could enrich APT2 or APT2-interacting proteins or reveal other protein targets. ML349-biotin was preassociated with streptavidin beads to decrease the sample processing time and limit dissociation of weak interacting proteins. The ML349-biotin/streptavidin resin was then incubated with HEK-293T whole cell lysate for 60 minutes and quickly transferred to spin columns for rapid washes. Since ML349 is a competitive inhibitor,

incubation with fluorophosphonate-TAMRA displaces any ML349-bound serine hydrolases from the resin (**Figure 3.3**). By in-gel fluorescence, ML349-biotin exclusively enriches a ~25 kDa hydrolase, corresponding to the molecular weight of APT2. Both o-ML349-biotin and unconjugated azide-PEG3-biotin did not enrich any hydrolases, providing two distinct controls to quantify ML349-binding proteins in cell lysates.

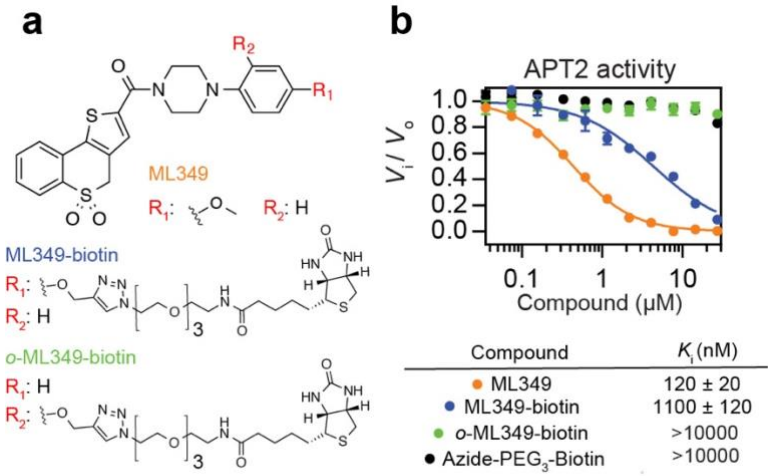

Figure 3.2 ML349 affinity probes inhibit APT2

(a) Chemical structures of ML349 and derivatives. (b) APT2 inhibition by ML349 and functionalized derivatives measured by resorufin acetate hydrolysis, reporting K_i values.

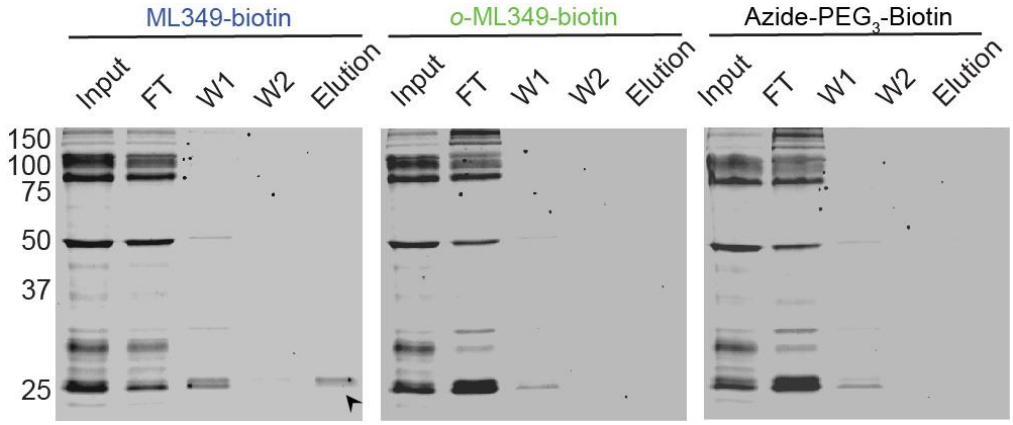

Figure 3.3 In-class selective APT2 enrichment by ML349-biotin

Elution of ML349-biotin enriched serine hydrolases from HEK-293T lysate and detection by FP-TAMRA in-gel fluorescence. A labeled band corresponding to the molecular weight of APT2 is highlighted with a black arrow. FT = flow through, W = wash.

Next, proteome-wide ML349-interacting proteins were eluted with excess ML349 and digested with trypsin for label- free mass spectrometry analysis. In our approach, we employed a data-independent acquisition workflow to maximize reproducibility, extracting precursor (MS1) peak area across replicates at high resolution (± 10 ppm), aligned retention times, and matched ion mobility drift times.[144] In this method, once a peak is annotated in one data set, it can be cross-extracted to populate data across replicates. Each biological replicate was analyzed with three technical replicates for each probe, providing a dense data set for precise statistical analysis. In pairwise comparisons, ML349-biotin significantly enriched about 10 proteins (>5-fold) compared to *o*-ML349-biotin or azide-PEG$_3$-biotin (**Figure 3a,b and Tables 3.1, 3.2**). This list includes APT2 (LYPA2), as well as the metabolite kinases ADK, DCK, and PDXK, the oxidoreductase NQO2, and the flavin adenine dinucleotide synthase FAD1.

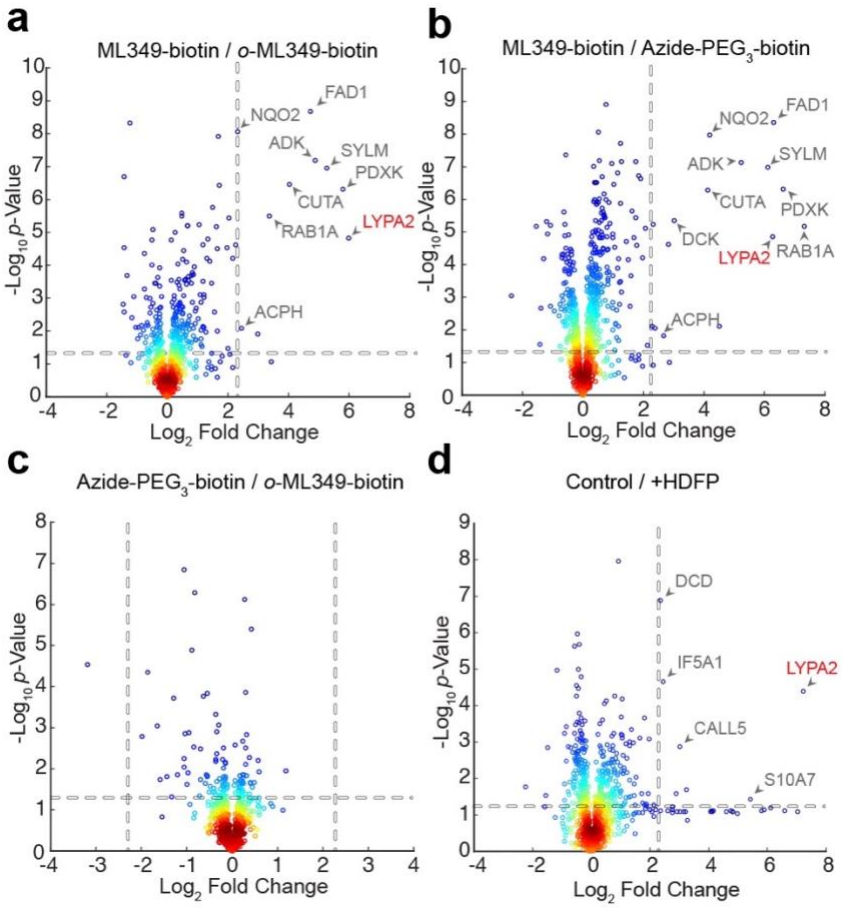

Figure 3.4 Label-free profiling of ML349-biotin enriched proteins.

(a) ML349-biotin enrichment relative to o-ML349-biotin. (b) ML349- biotin enrichment relative to azide-PEG3-biotin. (c) o-ML349-biotin enrichment relative to azide-PEG3-biotin reports few o-ML349-biotin enriched proteins. (d) ML349-biotin enrichment with or without (control) APT2 covalent inhibition by HDFP. Protein identifiers (Uniprot accession code) are shown for significantly enriched proteins quantified by at least three peptides. Dotted lines indicate a minimum 5-fold change and p-value less than 0.05. Enriched binding proteins from HEK-293T cell lysates are shown.

Table 3.1 List of significantly enriched proteins by ML349-biotin relative to o-ML349-biotin

Uniprot Accession	Description	o-ML349-biotin (average, n=6)	ML349-biotin (Average, n=9)	Fold Change	*p*-value
LYPA2	Acyl-protein thioesterase 2	79.6	5014.2	63.0	1.5E-05
PDXK	Pyridoxal kinase	103.3	5710.5	55.3	4.8E-07
SYLM	Probable leucine--tRNA ligase, mitochondrial	212.8	8114.9	38.1	1.1E-07
ADK	Adenosine kinase	152.3	4447.9	29.2	6.5E-08
FAD1	FAD synthase	56.5	1491.3	26.4	2.2E-09
CUTA	Protein CutA	162.2	2663.5	16.4	3.5E-07
RAB1A	Ras-related protein Rab-1A	10.5	107.8	10.3	3.2E-06
ACPH	Acylamino-acid-releasing enzyme	2715.7	14735.4	5.4	8.5E-03
NQO2	Ribosyldihydronicotinamide dehydrogenase [quinone]	1297.7	6533.6	5.0	8.6E-09

Table 3.2 List of significantly enriched proteins by ML349-biotin relative to Biotin-PEG3-Azide

Uniprot Accession	Description	Biotin-PEG-Azide (average, n=9)	ML349-biotin (average, n=9)	Fold Change	*p*-value
RAB1A	Ras-related protein Rab-1A	0.7	107.8	158.8	6.5E-06
PDXK	Pyridoxal kinase	57.7	5710.5	99.0	4.8E-07
FAD1	FAD synthase	19.0	1491.3	78.6	4.3E-09
LYPA2	Acyl-protein thioesterase 2	64.1	5014.2	78.2	1.4E-05
SYLM	Probable leucine--tRNA ligase, mitochondrial	118.0	8114.9	68.8	1.0E-07
ADK	Adenosine kinase	118.4	4447.9	37.6	7.3E-08
NQO2	Ribosyldihydronicotinamide dehydrogenase [quinone]	356.8	6533.6	18.3	1.1E-08
CUTA	Protein CutA	152.1	2663.5	17.5	5.1E-07
DCK	Deoxycytidine kinase	99.3	807.9	8.1	4.4E-06
K1C25	Keratin, type I cytoskeletal 25	138.0	867.2	6.3	1.5E-02
ACPH	Acylamino-acid-releasing enzyme	2810.3	14735.4	5.2	8.9E-03

Interestingly, NQO2 and ADK were both identified as binding proteins for active *S*-crizotinib stereoisomer,[145] although the antiproliferative phenotype comes solely from inhibiting the oxidized nucleotide phosphatase MTH1. NQO2 is also inhibited by the BCR-ABL inhibitors imatinib (IC_{50} = 82 nM) and nilotinib (IC_{50} = 381 nM) in steady-state substrate assays.[139] Additionally, the clinical PARP inhibitor niraparib inhibits DCK, preventing phosphorylation the chemotherapeutic nucleotide analogue cytarabine.[146] Based on these reported examples, several ML349-binding proteins may be general targets of many drug-like molecules. Other enriched proteins include the small GTPase Rab1A, the secreted acetylcholinesterase binding protein CutA, and the mitochondrial tRNA ligase SYLM. Importantly, o-ML349-biotin showed only marginal ~3-fold enrichment of NQO2 and FAD1 compared to azide-PEG_3-biotin alone, confirming its use as an orthogonal control probe (**Figure 3.4c**). Similar experiments were performed in MDCK cells lysates, where ML349 modulates Scrib S-palmitoylation.[75] This analysis returned a similar profile of binding partners, recapitulating ML349-biotin enrichment of APT2, as well as multimeric nucleotide kinases and flavin-dependent oxidoreductases. Pretreatment with the generic lipase inhibitor hexadecylfluorophosphonate (HDFP)[28] occludes the APT2 active site and blocks enrichment of APT2 (**Figure 3.4d** and **Table 3.3**). Since HDFP had no effect on ML349-binding protein enrichment, other enriched proteins are likely direct targets of ML349- biotin or ML349, and not APT2-interacting proteins.

Table 3.3 Significantly Enriched proteins in the presence and absence of HDFP

Uniprot Accession	Description	ML349-biotin (average, n=9)	HDFP-ML349-biotin (average, n=9)	Fold Change	*p*-value
LYPA2	Acyl-protein thioesterase 2	1888.7	4.7	150.1	4.1E-05
S10A7;S1A7A	Protein S100-A7	540.0	12.7	42.5	3.6E-02
K1C16	Keratin, type I cytoskeletal 16	4274.2	455.1	9.4	2.0E-02
CALL5	Calmodulin-like protein 5	411.6	51.5	8.0	1.4E-03
IF5A1;IF5A2;IF5AL	Eukaryotic translation initiation factor 5A-1	15.5	2.9	5.4	2.2E-05
DCD	Dermcidin	284.2	55.5	5.1	1.3E-07

In contrast to ABPP, affinity enrichment only returns proteins with some affinity for the ligand and does not report the fraction of enriched enzyme. Therefore, many of the enriched proteins could have marginal affinity for ML349-biotin, possibly influenced by the resin-enrichment strategy. On closer inspection, several of the enriched proteins from HEK-293T cells form oligomers, including NQO2 and PDXK. Based on this partial preference for oligomeric proteins, we wondered if avidity interactions contribute to the enrichment of weak ML349-interacting proteins.

Accordingly, we set out to validate and quantify ML349 binding to the recurring set of proteins. Recombinant APT2, NQO2, PDXK, and Rab1A were incubated with a fluorescein-conjugated ML349 to assay binding by fluorescence polarization.[84] ML349-fluorescein (ML349-FL) (**Figure 3.5a**) interacted similarly with APT2 (K_d = 900 nM) and PDXK (K_d = 1.4 μM), but failed to interact with NQO2 or Rab1A in solution (**Figure 3.5b**). Either these interactions are disrupted by the conjugated fluorescein, or they derive some additional affinity from the PEG-biotin reporter group. In the competition experiments, ML349-FL was readily competed with ML349 for APT2 (IC_{50} = 1.1 μM) but showed marginal competition with PDXK (IC_{50} > 10 μM) (**Figure 3.5c**). Furthermore, ML349- biotin only weakly competed with ML349-FL for both APT2 and PDXK (IC_{50} > 10 μM). Therefore, unlike APT2, PDXK does not discriminate between ML349 and ML349-biotin.

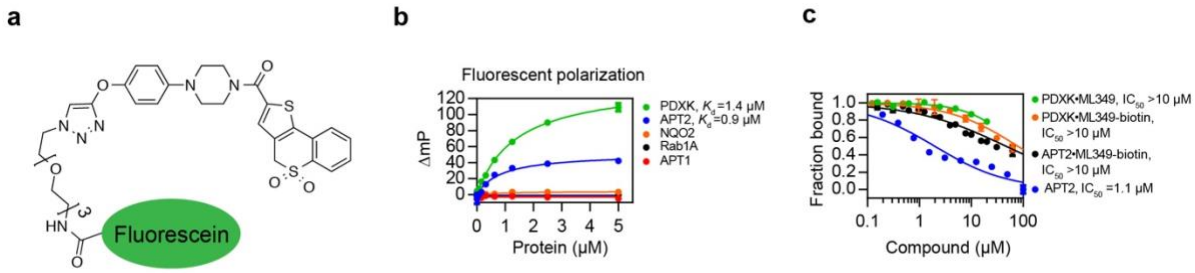

Figure 3.5 Competitive fluorescence polarization assay for ML349 binding.

(a) Chemical structure of ML349-FL. (b) ML349-FL binding to candidate interacting proteins detected by fluorescence polarization. (c) Dose-dependent competition of ML349-FL binding to APT2 or PDXK by ML349 and ML349-biotin.

Since the ML349-FL polarization experiments had limited target scope, we set out to evaluate ligand binding and stoichiometry by native mass spectrometry. Putative ML349-binding proteins were mixed in an equal ratio with ML349 and directly infused for electrospray ionization native mass spectrometry. Using nanoelectrospray ionization, proteins are transferred from native buffer into the gas-phase in a gentle fashion to maintain native-like conformations and noncovalent interactions with small molecules. The signals generated using this method have been shown to be reflective of solution-phase equilibria, providing a direct assay to profile protein−protein and protein−ligand interactions.[147] Since native MS analysis reports on electrosprayed protein−ligand complexes, we predict some deviation from solution-phase affinity measurements due to high local concentration of ligands within electrospray droplets. Nonetheless, this assay provides a direct measure of relative binding stoichiometry. As a proof of principle, ML349 and ML349-biotin did not form significant amounts of complex with the homologous hydrolase APT1, but formed a stoichiometric complex with APT2 with no observable dimer formation (**Figure 3.6a,b**). In agreement with 9-fold increase in K_i, ML349-biotin displayed substoichiometric binding to APT2 (**Figures 3.6a and 3.7**). This approach provides a rapid assessment of the relation between homodimerization and the stoichiometry of ML349 or ML349-biotin association (**Figures 3.6a and 3.7**). As expected, Rab1A was observed solely as a monomer, yet did not associate with ML349. PDXK and NQO2 were detected as homodimers, yet with sub- stoichiometrtic association with ML349 and ML349-biotin. NQO2 can associate with two ML349 ligands

per homodimer, yet ML349-biotin preferentially binds only one site per homodimer. Conversely, PDXK binds only one ML349 or ML349-biotin per dimer. Therefore, in contrast to NQO2, PDXK enrichment is unlikely biased by avidity effects. Nonetheless, on-resin interactions are likely quite different than those in solution or in the gas-phase. Overall, ML349 demonstrates significantly weaker affinity for Rab1A, NQO2, and PDXK, suggesting low-micromolar concentrations of ML349 achieve selective APT2 engagement in cells.

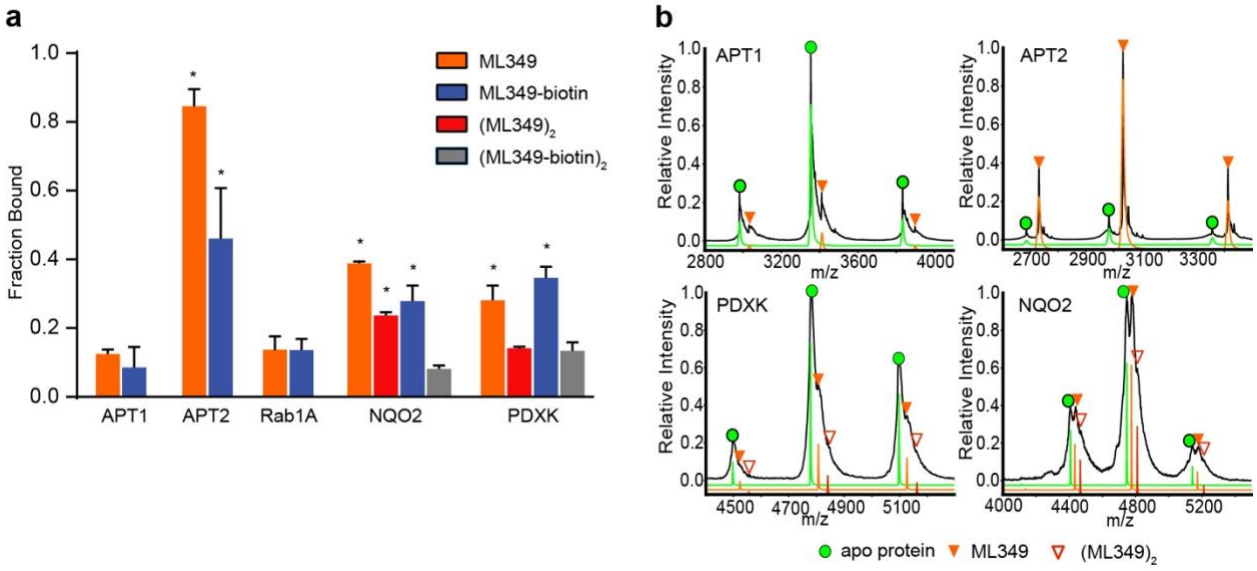

Figure 3.6 Native mass spectrometry profiling of inhibitor engagement and stoichiometry.

(a) Graphical distribution of ligand−protein complexes derived from native mass spectrometry analysis. NQO2 and PDXK formed observable dimers, forming two potential ligand binding sites per complex. Red bars represent occupancy at both binding sites, representing two ML349 molecules per dimer. Gray bars represent complete occupancy of ML349-biotin in NQO2 and PDXK. Asterisks (*) indicate a *p*-value less than 0.05, as compared to the nonspecific binding to APT1 (n = 3, standard deviation). (b) Representative mass/charge spectra with three charge states used for quantitation of proteins binding to ML349 before (black trace) and after deconvolution (green = apo protein, orange = ML349 bound protein, red = 2 xML349 bound protein) are shown for each protein.

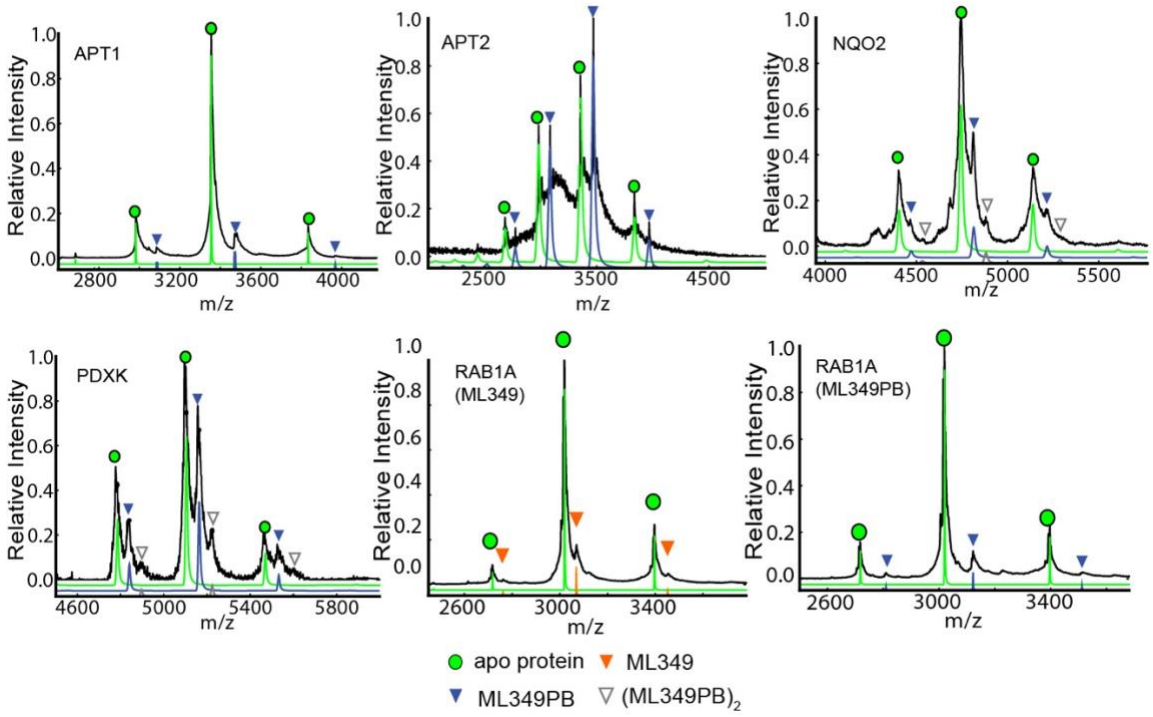

Figure 3.7 Native mass spectrometry analysis of ML349-biotin binding and stoichiometry.

Representative mass / charge spectra for each recombinant protein are shown. 3 charge states were for the quantitation. (Green = apo protein, blue = ML349-biotin bound protein, orange = ML349 bound protein, white triangle = 2xML349-biotin bound protein).

Discussion

As chemical proteomics methods become widely adopted, it is increasingly recognized that small molecule inhibitors often have multiple unanticipated binding partners in cells. In contrast to biochemical affinity-based methods, photoaffinity groups provide another sensitive approach to identify ligand targets in living cells.[148, 149] This approach retrieves a snapshot of live-cell engagement of putative interacting proteins, although quantifying the interaction affinity requires titrations, competitions, or additional biochemical validation. This becomes even more challenging for well-validated inhibitors like (+)-JQ1, where photoaffinity profiling identified an additional >100 additional cellular binding partners.[149] Clearly ligand space for many inhibitors is broader than previously envisioned. Other emerging approaches that leverage thermal stabilization may also miss many relevant interactions when the target is not sufficiently stabilized. Overall, various target identification methods each have different caveats, and selectivity from one assay can present different targets from another assay. ML349 is highly selective

by competitive fluorophosphonate ABPP, yet still weakly binds several hydrolases by ML349-biotin enrichment. Therefore, affinity-enrichment is likely more sensitive for initial target discovery, but does not provide information on the relative level of target occupancy. Importantly, many of the ML349-enriched targets are common to other chemoproteomic analyses, implying that many drug-like molecules share common promiscuous protein targets. Future efforts combining different target enrichment strategies will provide the most robust approach for understanding ligand selectivity across the proteome and provide new starting points for lead discovery across putative off-targets.

In summary, we present a detailed profile of the proteome-wide target landscape of the reversible APT2 inhibitor ML349. While fluorophosphonate ABPP was critical for the initial discovery and characterization of ML349, we now demonstrate that narrow in-class ABPP can overlook the extent of ligand targets outside of the tailored enzyme family. In this example, ML349-biotin/streptavidin resin enriches about a dozen targets outside of the serine hydrolase enzyme family, although confirmatory experiments suggest many of these may reflect multivalent interactions and are unlikely valid cellular targets at working inhibitor concentrations. Nonetheless, these efforts present a new affinity probe for profiling ligand engagement across this series of targets, providing a path to future competitive biochemical screens for proteins beyond the serine hydrolase enzyme family.

Materials and Methods

ML349-biotin pull-downs. Human HEK-293T cells were resuspended in phosphate buffered saline supplemented with 0.01% (v / v) triton-X (PBST) and sonicated briefly. Streptavidin-Agarose beads (EMD Millipore) (100 µL slurry) were incubated with 50 µM of ML349-biotin, *o*-ML349-biotin, or azide-PEG_3-biotin (Click Chemistry Tools) in PBST for 30 minutes at 4 °C, and washed three times. Next, 1 mg of cell lysate was added for 1 hour at 4 °C, centrifuged at 1000 x g for 1 minute, and then quickly washed 3 times with PBS. The enriched beads were then resuspended in 50 µL of PBS supplemented with 10 µM of ML349 and incubated for 1 hour at 4 °C. After centrifugation at 1000x g for 1 minute, the supernatant was transferred to another tube and treated with either 1

µM of FP-TAMRA for in-gel fluorescence or further processed for mass spectrometry analysis, diluting the sample in 6 M urea (4-fold) for 20 minutes at room temperature. Next, the sample was reduced with 5 mM Tris(2-carboxyethyl)phosphine hydrochloride (TCEP) for 20 minutes at 37 °C, and alkylated with 20 mM iodoacetamide for 1 hour at 37 °C in the dark. After 3-fold dilution in PBS, 2.5 µg of mass spectrometry-grade trypsin (Promega) was added and incubated overnight at 37 °C. Samples were desalted using Oasis HLB µElution plates (Waters), dried using the Savant SPD1010 SpeedVac (Thermo Scientific) and reconstituted in LC-MS buffer (3% acetonitrile in LC-MS grade water, 0.1% formic acid, and 10 fmol/µL *Saccharomyces cerevisiae* alcohol dehydrogenase (P00330) digest, Waters).

LC-MS proteomic analysis and data processing. Tryptic peptides were injected onto a 1D Waters NanoAquity UPLC system UPLC system equipped with a 5 µM Symmetry C18 (180 µm x 20 mm) trap column and a 1.8 µm High Strength Silica (HSS-T3) analytical column (75 µm x 150 mm). Initial loading of tryptic peptides was performed over 3 minutes by loading onto a trap column, followed by analytical separation over a 90-minute gradient (7% to 35% acetonitrile) coupled to a Waters Synapt G2S HDMS time-of-flight mass spectrometer with ion mobility separation using data independent acquisition methods (Waters Corp.). The nanoLC flow rate was 500 nl / min. Lock mass (Glu-fibronogen peptide, m/z = 785.8426) was collected every 30 seconds for internal reference mass calibration. The capillary voltage was set at 3.00 kV. The quadruple mass analyzer was manually set for mass 500, 600 and 700 and the sampling cone was set to operate at 32 eV. The nano flow gas was set to flow at 0.2 bar with the purge gas set to flow at 50 L / h and the source temperature was set at 70 °C. All measurements were collected with the mass spectrometer operating in resolution mode (resolving power of at least 20,000 FWHM (full-width at half maximum) in positive-mode ESI for 400 m/z). For Ion Mobility Separation (IMS) wave height was set as 40 V and IMS wave velocity as 600 m/s, with the spectral acquisition time each mode being 0.5 s. Collision energy (CE) ramp from 16 eV to 60 eV during each 0.5 s-integration was used as standard setting for the elevated energy MS scan. Data was analyzed with Progenesis QI for proteomics software (Nonlinear dynamics). The false discovery rate (FDR) was set to 1% with 1 maximum missed cleavage. The minimum ion matching requirements

were set to 2 fragments / peptide, 5 fragments / protein and 2 peptides / protein. The Top3 (3 most intense peptides) method was used for quantitative analysis. Briefly, the 3 most-intense peptides from each protein were used to quantify the average abundance of a protein.[150] Proteins with a minimum of 5-fold enrichment, a *p*-value less than 0.05, and at least 3 quantified peptides were assigned as putative ML349-biotin binding proteins.

Recombinant protein expression and purification. Human *LYPLA1* (*APT1*)*, LYPLA2* (*APT2*), *Rab1A, NQO2*, and *PDXK* genes were amplified from HEK-239T cell cDNA and sub-cloned into the pTrcHis2A bacterial expression vector (Sigma), transformed into BL21(DE3) cells, and induced with 0.5 mM IPTG for 16 hours at 25 º C. Cell pellets were lysed in 50 mM HEPES pH 7.8, 300 mM NaCl, and 10 % glycerol by sonication and cleared by centrifugation at 35000 x g for 30 minutes. The supernatant was incubated with Talon cobalt affinity beads for 1 hour (Invitrogen), washed, and eluted with imidazole. The eluted samples were dialyzed overnight in 50 mM HEPES pH 7.8, 150 mM NaCl and supplemented with 20 % glycerol before for storage at -80 º C.

Steady-state kinetic analysis. Resorufin acetate (Sigma) hydrolysis assays were performed to characterize APT2 inhibition, subtracting any spontaneous hydrolysis from the catalytic-dead enzyme (APT2-S122A). Steady-state inhibitors IC_{50} values were calculated by pre-incubating 10 nM protein with varying inhibitor concentrations for 30 minutes at room temperature. A fixed concentration of substrate (50 µM final) was aliquoted into each well and the reaction was initiated by the addition of the enzyme-inhibitor mixture and initial rates were measured. The data containing 8 replicates per inhibitor concentration was imported to Graphpad Prism 6 and a standard non-logarithmic sigmoidal dose response curve was fitted to each enzyme experiment. Each K_i value was calculated using Cheng-Prusoff equation, referencing previously reported K_m values. Fluorescence polarization assays were performed as previously described.[103]

Native mass spectrometry analysis. Native MS experiments were performed using a Synapt G2 ion mobility-mass spectrometer (Waters Corp.). Samples were buffer exchanged into 200 mM ammonium acetate using a Micro Biospin column (Bio-Rad, Inc. Hercules, California). Each protein was incubated at a final concentration of 10 µM

protein: 10 µM ligand (ML349 or ML349-biotin) in 5% DMSO for 5 min. Samples were electrosprayed from in-house gold-coated borosilicate capillaries. Instrument parameters were optimized for high transmission of protein-ligand ions with minimal gas-phase dissociation. The backing pressure was set to ~8 mBar and the capillary potential was set to 1.6 kV, with a sampling cone potential of 30 V. For monomeric species, the trap collision energy was set to 20 V for efficient transmission of ions with no observable unfolding or ligand dissociation. For dimeric species, the trap collision energy was set to 50 V for more efficient desolvation, with no apparent ligand dissociation. Spectra were acquired from 1000 to 10000 m/z for 1 minute. Other instrument parameters were set to those found described as optimal in previous literature.[151] The resulting datasets were processed and deconvolved using Unidec[152] to yield relative abundances of apo and bound proteins. Relative abundance ratios were also validated manually using background subtraction and integration tools mMass.[153] Ratios of manually integrated peak areas were compared with the relative intensities derived from Unidec and found to be within 5% error in all cases.

General chemical synthesis and purification procedures.

Can be found in Appendix B.

Individual contributions

Sang Joon Won and Fei San Chong synthesized compounds. Sang Joon Won performed affinity purification proteomic experiments. Sang Joon Won and Jaimeen Majmudar processed and analyzed LC/MS data. Sang Joon Won purified all proteins. Sang Joon Won and Sin Ye Hwang performed enzyme assays. Joseph Eschweiler and Brandon Ruotolo performed native mass spectrometry and interpreted the data. Sang Joon Won and Brent Martin designed experiments and wrote the paper.

Chapter 4 : Temporal Profiling Establishes a Dynamic S-palmitoylation Cycle[§]

Abstract

S-palmitoylation is required for membrane anchoring, proper trafficking, and the normal function of hundreds of integral and peripheral membrane proteins. Previous bioorthogonal pulse-chase proteomics analyses identified Ras family GTPases, polarity proteins, and G proteins as rapidly cycling *S*-palmitoylated proteins sensitive to depalmitoylase inhibition, yet the breadth of enzyme regulated dynamic *S*-palmitoylation largely remains a mystery. Here we present a pulsed bioorthogonal *S*-palmitoylation assay for temporal analysis of *S*-palmitoylation dynamics (**Figure 4.1**). Low concentration hexadecylfluorophosphonate (HDFP) preferentially inactivates the APT and ABHD17 families of depalmitoylases, which dramatically increases alkynyl-fatty acid labeling and stratifies *S*-palmitoylated proteins into kinetically distinct subgroups. Surprisingly, HDFP treatment has no effect on steady-state *S*-palmitoylation levels, in agreement with *S*-palmitoylation profiling of APT1$^{-/-}$/APT2$^{-/-}$ mouse brains. Thus, disrupting depalmitoylase activity enhances levels of incorporated probe, but does not significantly affect steady state *S*-palmitoylation across the proteome.

[§] This chapter presents a submitted manuscript by Sang Joon Won and Brent Martin (2018).

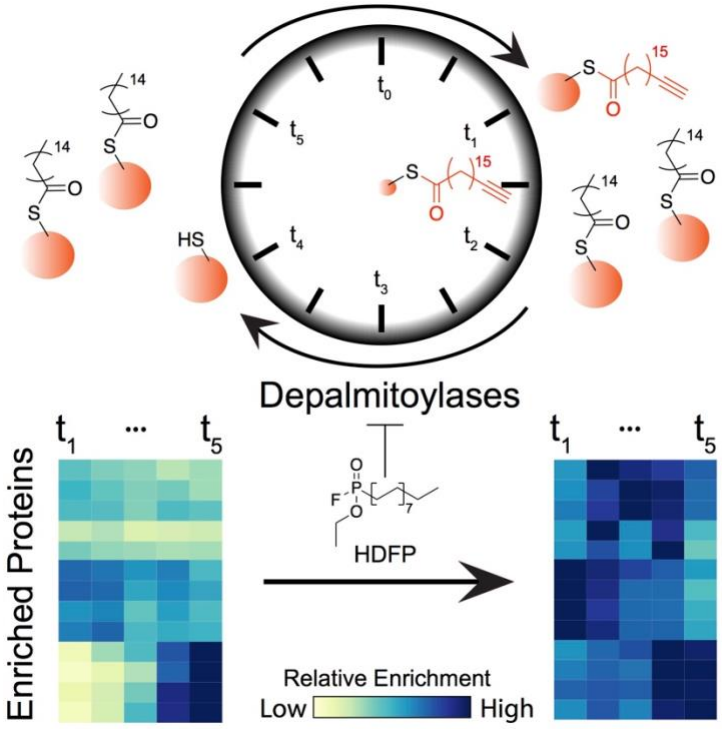

Figure 4.1 Graphical abstract

Introduction

The palmitoylation / depalmitoylation machinery establishes a spatially directed flow of *S*-palmitoylated proteins along vesicular pathways towards the plasma membrane, effectively overriding entropy-driven random membrane distribution. [20] The complete cycle occurs within seconds, where proteins are dynamically palmitoylated and depalmitoylated to effectively restrict transport along the flux of vesicular traffic. Generic depalmitoylase inhibition blocks this cycle, distributing plasma membrane targeted peripheral membrane proteins, such as Ras-family small GTPases [61] and G-proteins[23] , randomly across internal membranes. In contrast, inhibition of the depalmitoylase APT2 corrects an imbalanced palmitoylation cycle in malignant cells to restore lateral membrane localization of the multi-domain polarity scaffolding protein SCRIB. [75] Across decades of study, protein depalmitoylation has emerged as a critical mechanism for dynamic membrane localization, trafficking, and functional regulation, yet the breadth of substrates and global dynamics remain poorly characterized on a global scale.[154]

The recent development bioorthogonal labeling strategies has transformed the analysis of dynamic *S*-palmitoylation. [155] Pulse-chase metabolic labeling with the

alkynyl-fatty acid reporter 17-octadecynoic acid (17-ODYA) and click chemistry conjugation to biotin-azide has enabled quantitative proteomics assignment of a proteins with accelerated turnover dynamics, including Ras-family small GTPases, G-proteins, and cell polarity organizing proteins.[28] This accelerated turnover is stabilized by treatment with hexadecylfluorophosphonate, a broad inhibitor of cellular lipases.[28] While identifying new targets of depalmitoylase regulation, this limited profile falls short of many historical biochemical analyses demonstrating widespread depalmitoylase action across *S*-palmitoylated substrates.[156] This discrepancy is likely due to the poor sensitivity of the alkynyl-fatty acid pulse-chase assay, particularly since alkynyl fatty acids are incorporated broadly across lipid classes. [47] Once distributed across membrane lipids, addition of excess palmitate is not very efficient in pulse-chase experiments, and limits sensitive analysis of proteome-wide *S*-palmitoylation turnover rates.

Here we present a multiplexed pulse-labeling method for profiling the kinetics of alkynyl fatty acid incorporation. The resulting kinetic signatures corroborate previous pulse-chase analysis, and reveal the presence of a conserved S-palmitoylation kinetic profile between different cell lines. In addition, HDFP increases alkynyl fatty acid incorporation through covalent inactivation of lipid hydrolase and depalmitoylase enzymes, revealing a much broader role for depalmitoylase regulation. While metabolic labeling reveals significant dynamics, hydroxylamine-switch methods do not identify any major steady-state S-palmitoylation changes. Furthermore, steady-state profiling of mouse brain samples deficient in both acyl protein thioesterases (APT1 and APT2) similarly lacked any change in global *S*-palmitoylation. Accordingly, we propose metabolic labeling only accesses a dynamic fraction of modified proteins, and these changes are lost in bulk steady-state analyses. These studies corroborate the presence of a dynamic palmitoylation cycle, and demonstrate multiple depalmitoylases contribute to the global *S*-palmitoylation regulation.

Results

Quantitative proteomic analysis of alkynyl fatty acid pulse-chase labeling revealed a distinct subset of depalmitoylase-regulated S-palmitoylated proteins[28] but

sensitivity is hampered by the high concentrations of alkynyl reporters required for in-gel or mass spectrometry analysis. To avoid these challenges, we focused our efforts on profiling the temporal dynamics of S-palmitoylation, since probe incorporation must reflect the rate of S-palmitoylation cycling in cycloheximide treated cells. Interestingly, treatment with the promiscuous lipase inhibitor HDFP stimulates a time-dependent increase in alkynyl fatty acid incorporation broadly across labeled proteins, even at relatively early time points across multiple cell lines (**Figures 4.2A, 4.3A, and 4.3B**). The effect was independent of 17-ODYA labeling concentrations (**Figure 4.2B**), and present even at sub-micromolar HDFP concentrations. Competitive activity-based protein profiling (ABPP) with fluorophosphonate-rhodamine (FP-TAMRA) confirmed inactivation of the depalmitoylase enzymes APT1 and APT2 at sub-micromolar HDFP concentrations sufficient to stimulate 17-ODYA incorporation (Figures 4.2C and 4.2D). Quantitative mass spectrometry analysis identified a subset privileged HDFP targets (**Figure 4.2E**) including APT and ABHD17 family depalmitoylase enzymes. More selective inhibition of APT1 and APT2 similarly had no significant effect on 17-ODYA incorporation, suggesting the enhanced label incorporation may require the inhibition of alternative depalmitoylases (**Figures 4.4A-C**). Further profiling of FASN, PPT1, ABHD6, CES3, and NCEH1 similarly failed to stimulate 17-ODYA incorporation (**Figures 4.4D-G**). Nonetheless, HDFP is a potent modulator of S-palmitoylation useful for broadly profiling dynamic regulation.

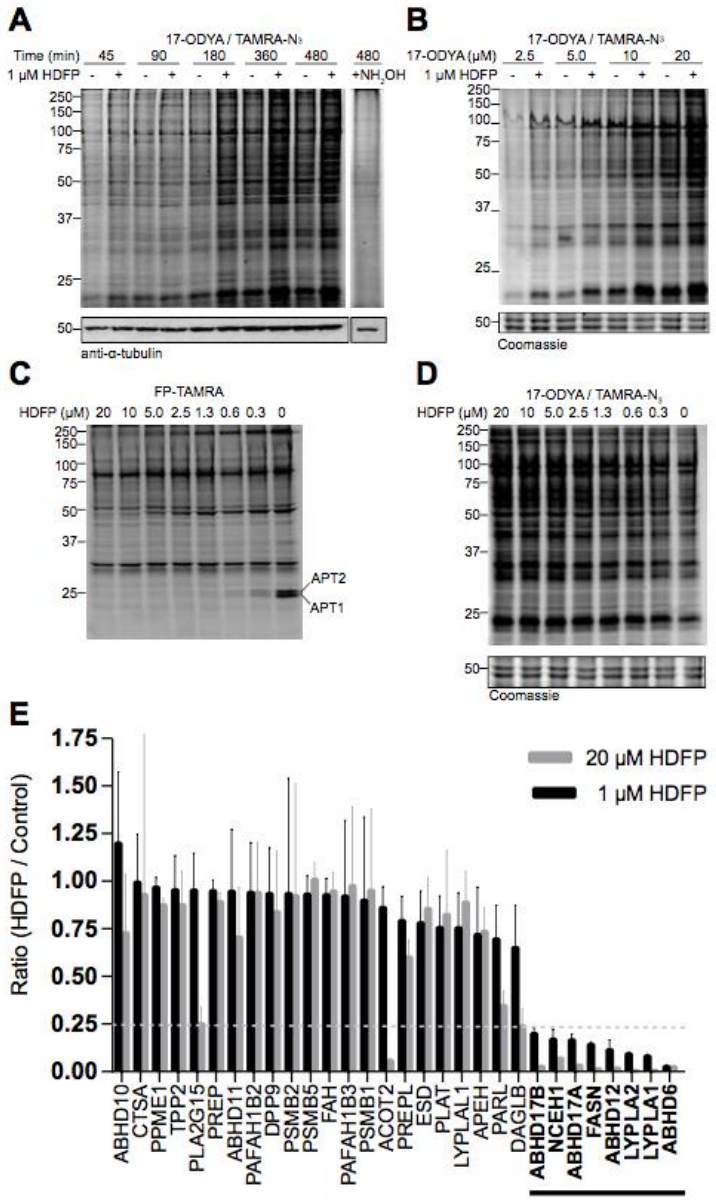

Figure 4.2 Depalmitoylase inhibition enhances 17-ODYA labeling

A) HDFP enhances 17-ODYA incorporation at all time points during labeling. Neutralized 0.5 M hydroxylamine (NH_2OH) hydrolyzes 17-ODYA labeling, demonstrating the presence of a thioester linkage. (B) Different concentrations of 17-ODYA do not affect HDFP-dependent enhanced probe incorporation. (C) Fluorophosphonate-TAMRA (FP-TAMRA) competitive ABPP demonstrates APT enzymes are inactivated by sub-micromolar HDFP concentrations. (D) Dose-dependent profile of HDFP-dependent enhancement of 17-ODYA incorporation. (E) Competitive ABPP mass spectrometry analysis of HDFP inhibition across the serine hydrolase family. Error bars represent error propagated from standard errors at differing HDFP concentrations, quantified from multiplexed TMT isobaric reporter ions. N = 4. Serine hydrolases with >2 PSMs are shown. Analysis was performed in human 293T cells across these experiments.

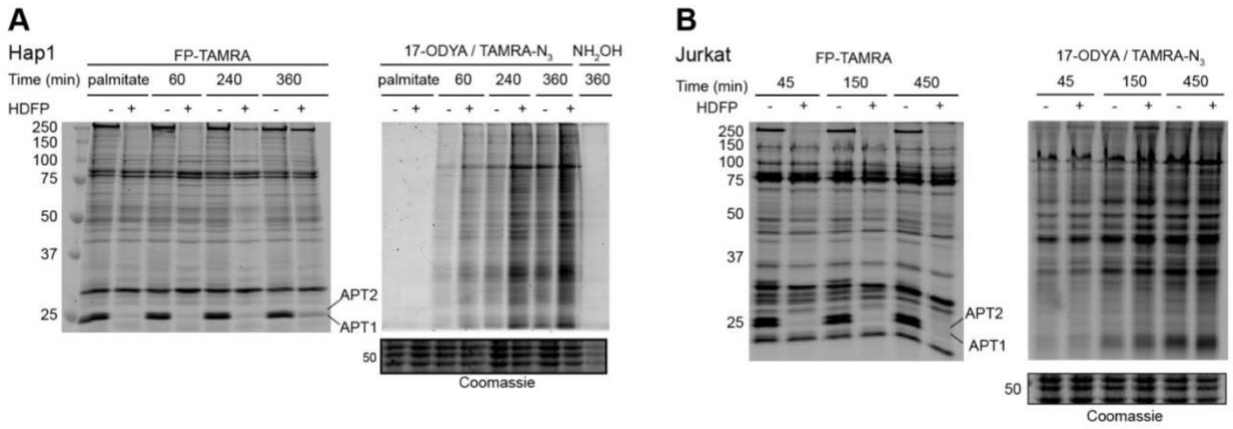

Figure 4.3 HDFP augments 17-ODYA incorporation in multiple cell lines.

(A) Kinetic profile of 17-ODYA labeling demonstrates HDFP-dependent enhancement in Hap1 cells. Competitive ABPP analysis of HDFP treatment in while cell lysates with FP-TAMRA confirms inhibition of APT enzymes and other HDFP-sensitive hydrolases. Hydroxylamine (NH_2OH) addition eliminates 17-ODYA labeling, confirming thioacylation of cellular proteins by 17-ODYA. (B) Kinetic profile of 17-ODYA labeling in Jurkat cells is also stimulated by HDFP.

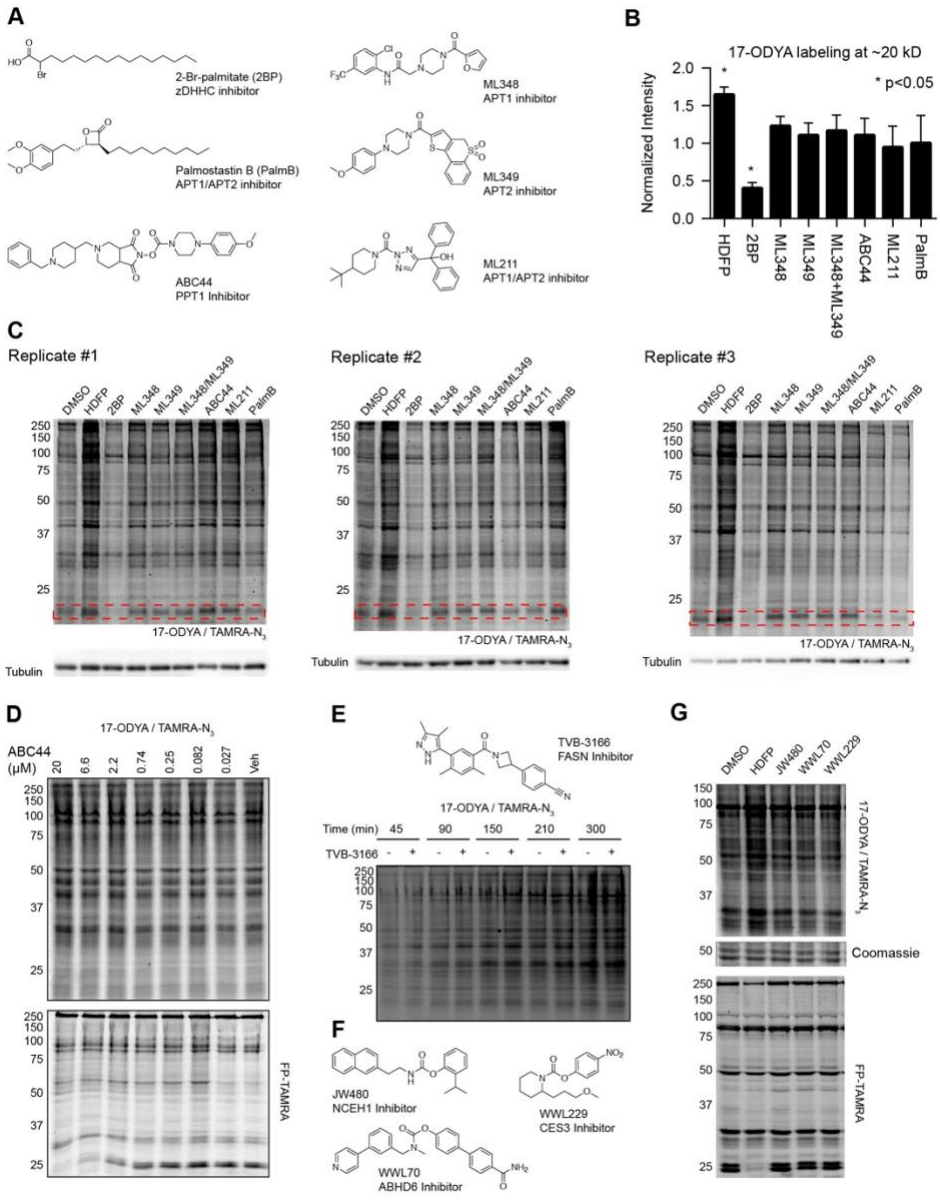

Figure 4.4 Pharmacological profiling of hydrolase-regulated 17-ODYA labeling in cells

(A) Structures of acyl protein thioesterase and zDHHC inhibitors. (B) APT inhibition does not affect 17-ODYA incorporation levels in 293T cells. 1 μM HDFP, 50 μM 2BP, 10 μM ML348, ML349, and PalmB, 1 μM ABC44 and ML211 were used. Data represents the average and standard error of 3 independent replicates, shown in (C). Red boxes illustrate the 20 kD band used for quantitation, which represents the molecular weight of Ras-family small GTPases. Intensity in each lane is normalized to the alpha-tubulin loading control. (D) PPT1 inhibition has no effect on 17-ODYA incorporation. High concentrations of ABC44 also inhibit APT enzymes. (E) FASN inhibition (1 μM TVB-3166) has no effect on 17-ODYA incorporation. (F) Structures of reported carbamate inhibitors for other HDFP targets. (G). ABHD6, CES3, and NCEH1 inhibition has no effect on 17-ODYA incorporation. Inhibitors were added at 15 μM final concentration, except HDFP (1 μM).

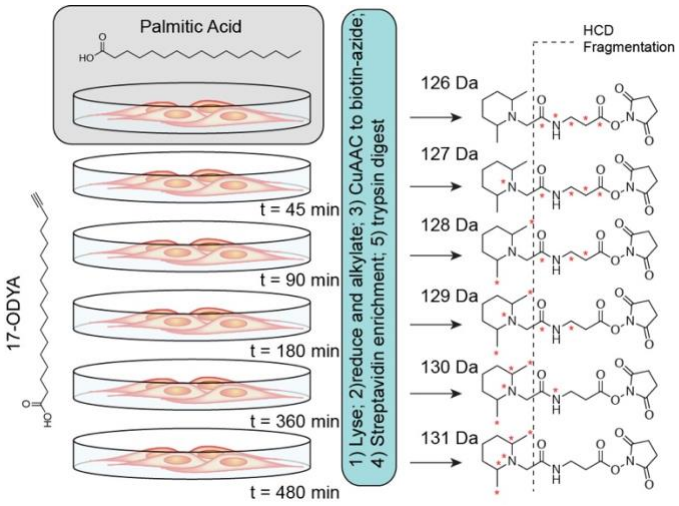

Figure 4.5 Schematic of multiplexed kinetic profiling of S-palmitoylation.

Cells are incubated with 17-ODYA for various time points, followed by click chemistry to biotin-azide, streptavidin enrichment, trypsin digestion, and labeling with lysine reactive TMT reagents for quantitative mass spectrometry analysis.

Based on these observations, we designed a multiplexed mass spectrometry approach for temporal profiling of bioorthogonal *S*-palmitoylation (**Figure 4.5**). Human 293T cells were incubated with cycloheximide to block protein synthesis and co-translational *N*-myristolyation, followed by 17-ODYA incubation for varying times. After click chemistry conjugation to biotin-azide, streptavidin enrichment, and trypsin digestion, the eluted peptides we incubated with amine-reactive 6Plex-TMT isobaric labeling reagents and combined for quantitative mass spectrometry analysis. Data was filtered based to include proteins annotation by at least 3 peptide spectrum matches (PSMs) and with >2-fold enrichment over the control across the last 3 time points. This analysis yielded several hundred specifically enriched proteins in 293T cells (**Table 4.1**), and nearly twice as many in HAP1 cells (**Table 4.2**), both largely overlapping with previously published *S*-palmitoylation proteomics studies. [30]

Hierarchical cluster analysis classified *S*-palmitoylated proteins with different kinetic features. For example, NRAS, SCRIB, MTDH, and GNAS were all grouped together in the most rapidly *S*-palmitoylated sub-group (**Figure 4.6A** and **Table 4.1**), corroborating previous pulse-chase studies. [28] Within this accelerated group, 17-ODYA incorporation peaks within 90 minutes, followed by decay to a steady state equilibrium. Since the analysis relies on quantitation of tryptic peptides outside of the specific *S*-

palmitoylation sites, proteins with multiple *S*-palmitoylation sites would be predicted to incorporate 17-ODYA at a faster rate than proteins with a single *S*-palmitoylation site. Despite this prediction, there is no clear correlation between multiply *S*-palmitoylated proteins and the rate of probe incorporation. For example, SNAP23 has at least 5 *S*-palmitoylation sites [157], yet demonstrates relatively average probe incorporation kinetics.

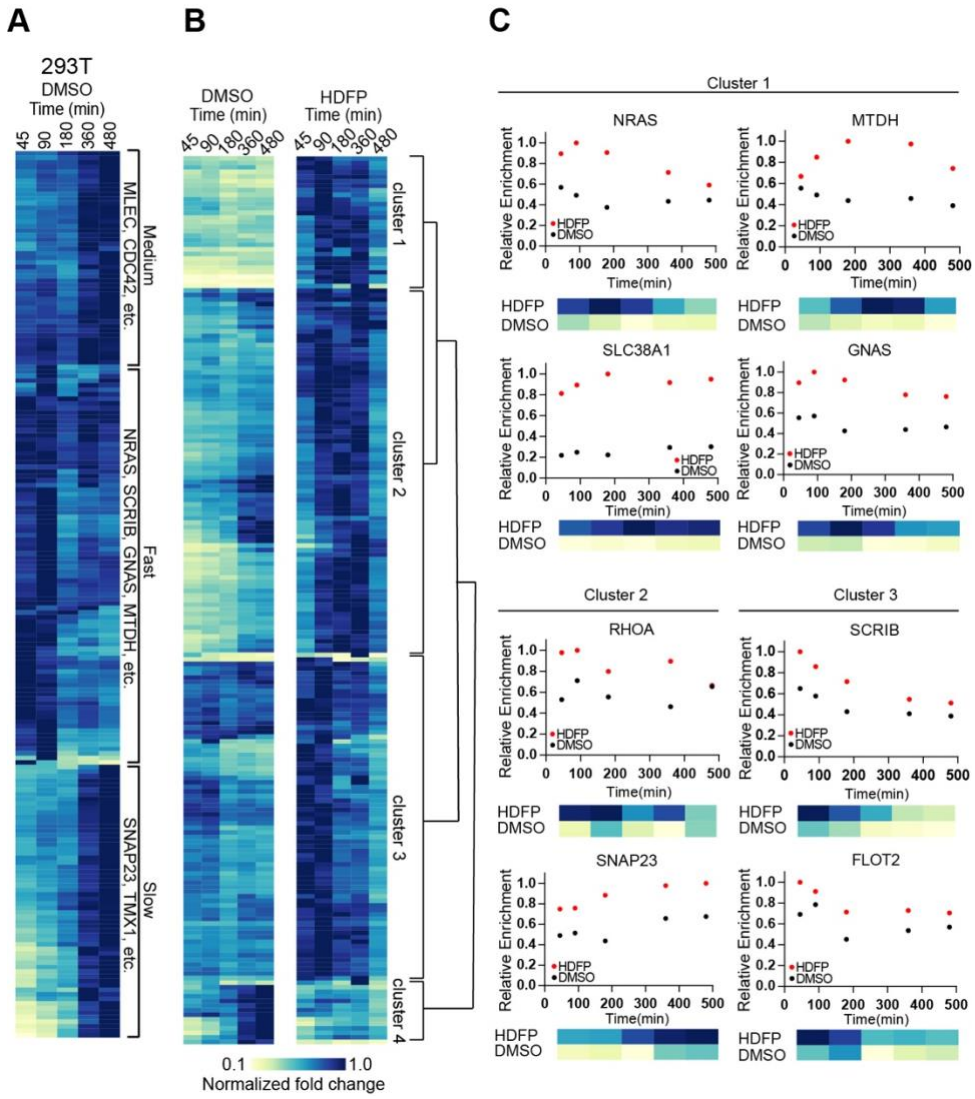

Figure 4.6 Time-dependent profiling of 17-ODYA incorporation identifies kinetic clusters of dynamic S-palmitoylated proteins

(A) Clustered heat map of enriched proteins from 293T cells labeled with 17-ODYA for increasing lengths of time. Clusters of "fast", "medium", and "slow" are highlighted. Branches are simplified for clarity. Proteins were identified by 3 or more PSMs and demonstrate >2-fold enrichment over DMSO controls. (B) Hierarchical clustering of 17-ODYA enriched *S*-palmitoylated proteins across both control and HDFP-treated cells reveals distinct kinetic clusters in 293T cells. Proteins with >2-fold enrichment and at least 3 PSMs are shown. The heat map is normalized to the highest point along the labeling time course. Branches were simplified to highlight higher level grouping. (C) Representative labeling time course of select proteins from each subclass.

In the same multiplexed analyses, HDFP treatment accelerated the kinetics of 17-ODYA labeling, defining different *S*-palmitoylated proteins with more or less sensitivity to depalmitoylase inhibition (**Figure 4.6B, Figure 4.7A, Tables 4.1-4.2**). Paired clustering of control and HDFP treated cells led to further kinetic segregation, producing 4 major categories, essentially stratifying proteins based on their kinetic response to depalmitoylase inhibition (**Figure 4.6C and 4.7B**). Cluster 1 represents enriched proteins with both fast incorporation and relatively high sensitivity to HDFP at all time points. Cluster 2 represents enriched proteins with mild sensitivity to HDFP during the early to middle time points (RHOA, SNAP23, etc.). Cluster 3 represents enriched proteins with high HDFP sensitivity in early time points (SCRIB, FLOT2, etc.). Cluster 4 includes proteins with reduced labeling upon HDFP addition, and includes many proteins reported across multiple *S*-palmitoylation proteomics datasets. [30] These proteins may represent common false positives or could be enriched via chemically distinct mechanisms of protein acylation. Interestingly, NRAS *S*-palmitoylation is initially stimulated in HDFP treated samples, but decays over time and eventually equilibrates to similar levels as control cells. In many instances, HDFP shifts proteins to a hyper *S*-palmitoylated state (MTDH, GNAS, SLC38A1, etc.), presumably increasing the steady-state stoichiometry of probe incorporation. These clusters are largely similar between 293T cells and HAP1 cells, supporting a conserved program of temporal and enzymatic regulation (**Figure 4.7B-C**).

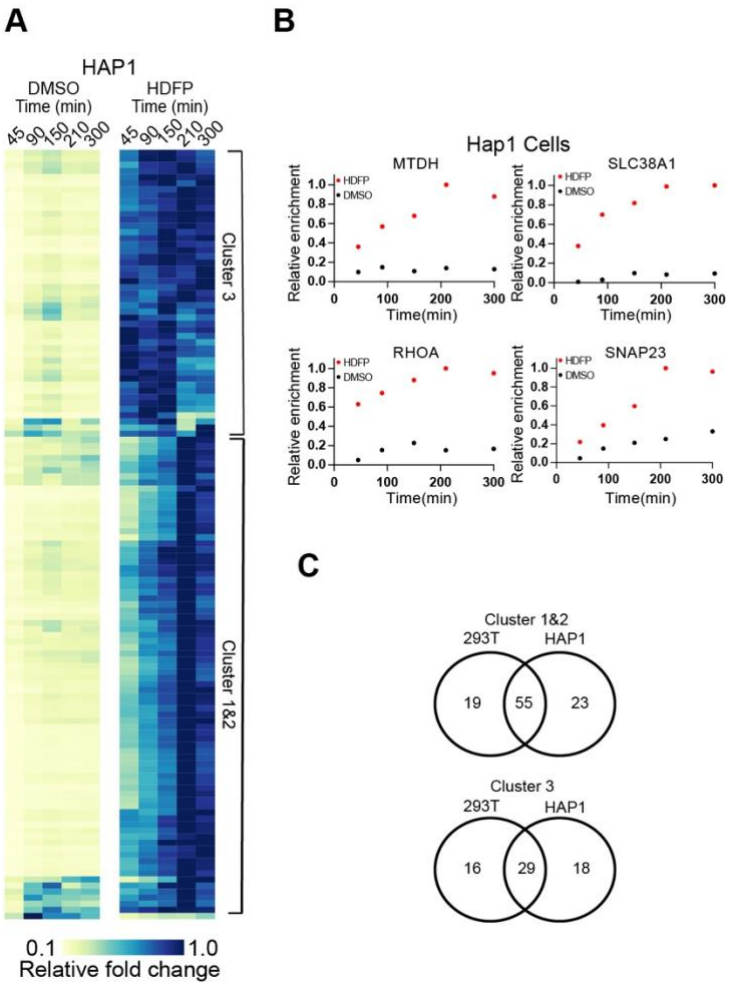

Figure 4.7 Multiplexed kinetic profiling of 17-ODYA incorporation in HAP1 cells

(A)Clustered heat map of *S*-palmitoylated proteins from HAP1 cells labeled with 17-ODYA comparing the effects of depalmitoylase inhibition with HDFP. Proteins identified in both 293T and HAP1 cells are shown. Clusters correspond to the kinetic groups described for 293T cells in **Figure 4.6**. (B) Representative *S*-palmitoylation kinetics from HAP1 cell analysis corresponds data in **Figure 4.6** (C) Representative overlapping clusters from 293T and HAP1 define conserved *S*-palmitoylation labeling kinetics and depalmitoylation effects across cell types.

Since HDFP promotes greater 17-ODYA labeling, we questioned whether this translates to an increase in steady-state *S*-palmitoylation levels. In contrast to bioorthogonal metabolic labeling, steady-state *S*-palmitoylation can be assayed by methods using hydroxylamine-dependent thioester hydrolysis, thiol capture, and enrichment.[38] In the acyl-Resin-Assisted Capture (acyl-RAC) protocol, thiols are first reduced and alkylated, and hydroxylamine is added to hydrolyze thioesterified cysteines for capture on pyridyl-disulfide conjugated agarose resin. This method is agnostic to the nature of the acyl group, and captures both *S*-palmitoylated and endogenously thioesterified proteins, including lipoamide cofactor-dependent dehydrogenases and

ubiquitin ligases. Despite the prevalence of bioorthogonal metabolic labeling and hydroxylamine-switch assays for *S*-palmitoylation, there have been no direct comparison by mass spectrometry profiling. In-gel hydroxylamine-switch analysis demonstrated no obvious changes in steady-state *S*-palmitoylation after HDFP or both HDFP and 17-ODYA (**Figure 4.8A**). Analysis of HDFP or HDFP/17-ODYA treated cells by acyl-RAC enrichment and multiplexed mass spectrometry analysis confirmed that lipase inhibition has no major effect on global steady-state *S*-palmitoylation levels (**Figures 4.8B, 4.9A-B,** and **Table 4.3-4.4**). These results were corroborated by gel-based analysis of RAS and SCRIB, which were selected based on their validated dynamic *S*-palmitoylation[28, 75] and their rapid increase in 17-ODYA labeling after HDFP treatment. Following acyl-RAC enrichment, neither protein was significantly different in HDFP treated samples (**Figures 4.8C-D** and **4.9C-D**).

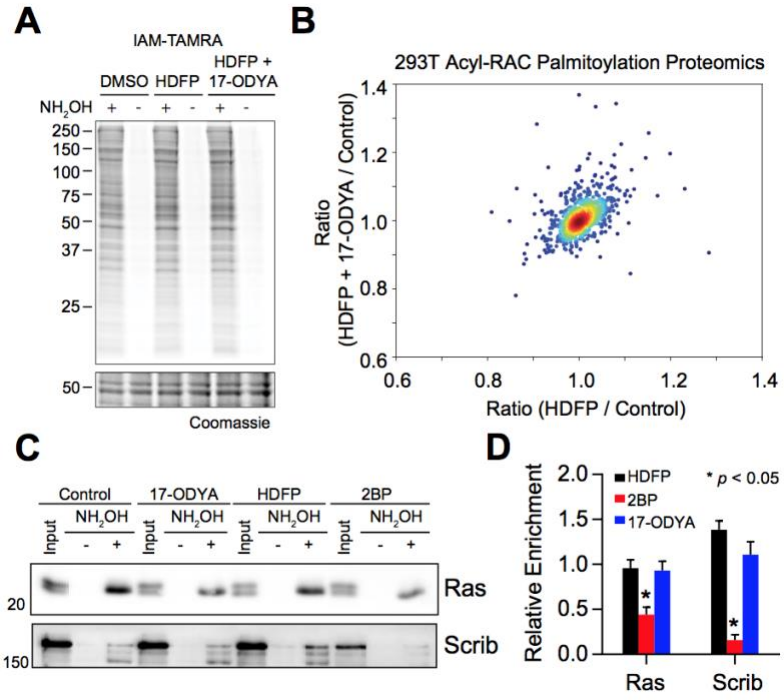

Figure 4.8 Depalmitoylase inhibition does not influence steady-state S-palmitoylation.

(A) In-gel analysis of *S*-palmitoylation using the hydroxylamine-switch analysis reports equivalent labeling profiles after 17-ODYA and HDFP treatment. Iodoacetamide-rhodamine (IAM-TAMRA) labeling reports the presence of hydroxylamine sensitive thiols. (B) Equivalent enrichment of *S*-palmitoylated proteins by quantitative proteomic analysis of acyl-RAC enriched proteins from control (DMSO) and HDFP or HDFP+17-ODYA treated cells, N=4. Proteins with >2 PSMs, multiple annotations in SwissPalm are shown. (C) Confirmatory acyl-RAC analysis of pan-RAS and SCRIB *S*-palmitoylation. (D) Quantitation of acyl-RAC enrichment relative to control (DMSO) across replicates after normalizing to input (Ras, N = 5 for all conditions except 17-ODYA, N = 3; Scrib, N = 3 for all conditions except 17-ODYA, N = 2, ±SEM) demonstrates no significant changes following HDFP treatment, but shows major reductions after 2BP treatment (two-tailed Student's t-test with unequal variance).

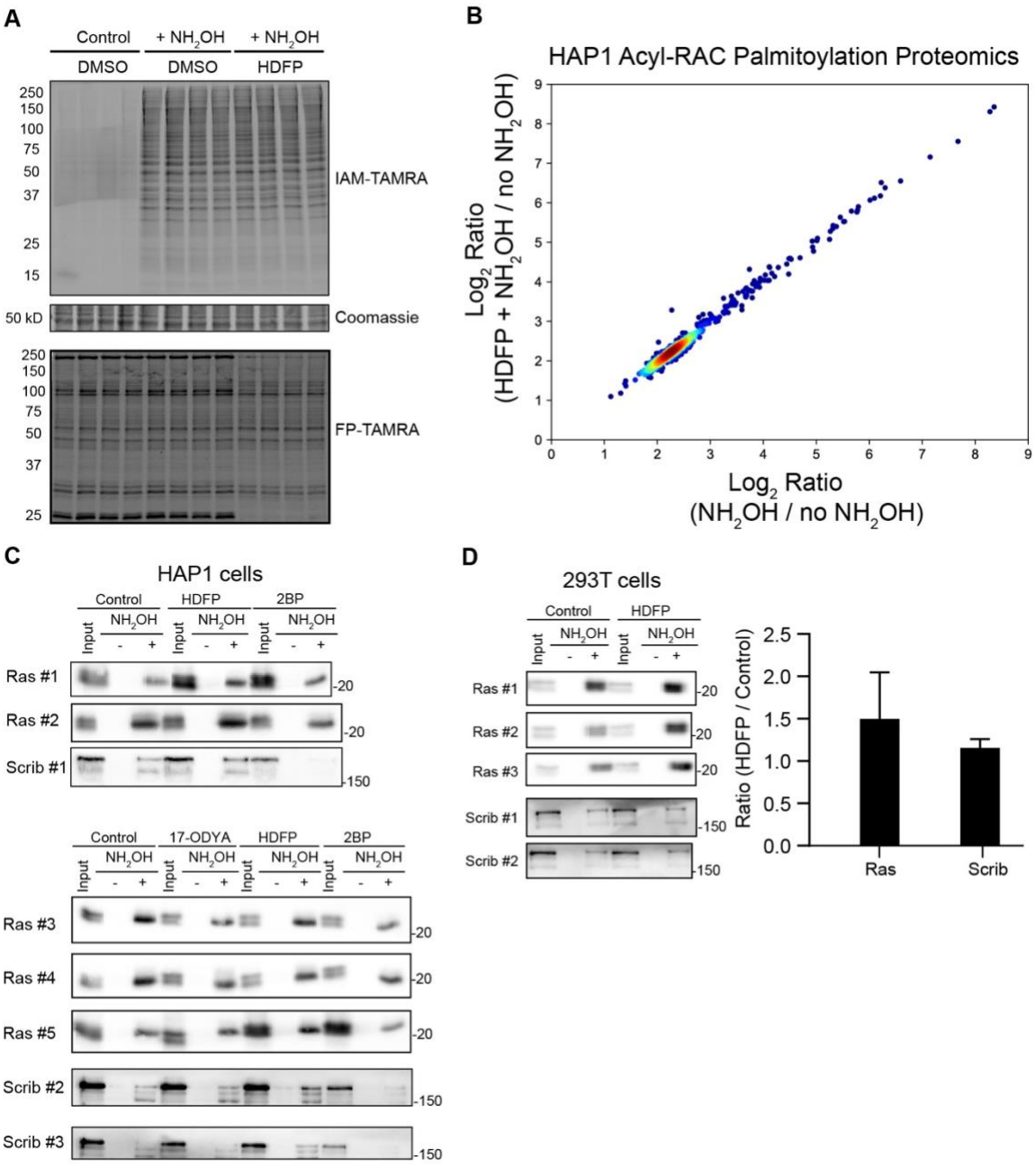

Figure 4.9 Steady-state S-palmitoylation is not affected by depalmitoylase inhibition.

(A) Hydroxylamine-switch assay in HAP1 cells. 4 replicates in each condition. (B) Fold-change correlation plot of Acyl-RAC enriched proteins in HAP1, N = 4. Proteins with >2 PSMs and multiple annotations in SwissPalm are shown. (C) Replicates of acyl-RAC blots as described in **Figure 4.8C-D.** (D) Acyl-RAC replicates of Ras and Scrib in 293T cells. Cells were incubated with HDFP for 90 minutes. Quantitative enrichment relative to DMSO control is shown. N = 3 for Ras, N = 2 for Scrib. Error bars represent the standard deviation. Changes are not significant ($p > 0.05$).

Conversely, the broadly reactive *S*-palmitoylation inhibitor 2-bromo-palmitate (2BP)[49] reduced both RAS and SCRIB steady-state *S*-palmitoylation, verifying sufficient

sensitivity to measure chemically modulated *S*-palmitoylation. Nonetheless, 2BP can directly modify depalmitoylases, including APT [158] and ABHD17 enzyme families[49], and thus could affect both arms of the *S*-palmitoylation cycle. Importantly, gel-based analysis using standard image auto-thresholds demonstrates an apparent increase in Ras *S*-palmitoylation (**Figure 4.9D**). After loading control normalization, these effects are neither large nor significant, underscoring the importance of biological replicates for accurate and precise measurements. Overall, HDFP enhances the stoichiometry of alkynyl labeling, but does not greatly impact bulk steady-state *S*-palmitoylation levels in either 293T or HAP1 cells.

The protein depalmitoylases APT1 and APT2 are structurally similar α/β-hydrolases[103] and catalyze depalmitoylation across dozens of proteins both *in vitro* and in cells [156]. Despite the predicted role for APT1 and APT2 in broad regulation of protein depalmitoylation, cell-based studies rely exclusively on inhibitors or RNA interference to probe cellular phenotypes. Even with an arsenal of APT1 and APT2 inhibitors[100], there have not been any reported efforts to profile APT1 and/or APT2 dependent *S*-palmitoylation. To address this gap, APT1 (Lypla1) and APT2 (Lypla2) knockout mice were acquired through commercial sources, and crossed to generate double knockout mice. The resulting mice double knockout mice were viable and fertile, yet were born at sub-Mendelian frequencies. Whole brains were harvested from 3-month old APT1$^{-/-}$/APT2$^{-/-}$ mice for *S*-palmitoylation analysis. Double knockout was confirmed by fluorophosphonate activity-based profiling (**Figure 4.10A**). As observed with HDFP-treated cells, there was no visual change in the *S*-palmitoylation profile by in-gel hydroxylamine-switch analysis (**Figure 4.10B**). These observations were confirmed by multiplexed mass spectrometry, again reporting no obvious changes in *S*-palmitoylation levels by APT1 and APT2 deletion, with the exception of MAP6 (2.5-fold increase) (**Figure 4.10C** and **Table 4.5**). Interestingly, MAP6 was recently reported to require ABHD17 activity to maintain a dynamic *S*-palmitoylation necessary for synaptic trafficking [106]. This suggests either an interplay between ABHD17 and APT enzymes or differential depalmitoylase regulation between cultured primary neurons and brain. Accordingly, APT1 and APT2 knockout does not affect steady-state *S*-palmitoylation levels in the mouse brain.

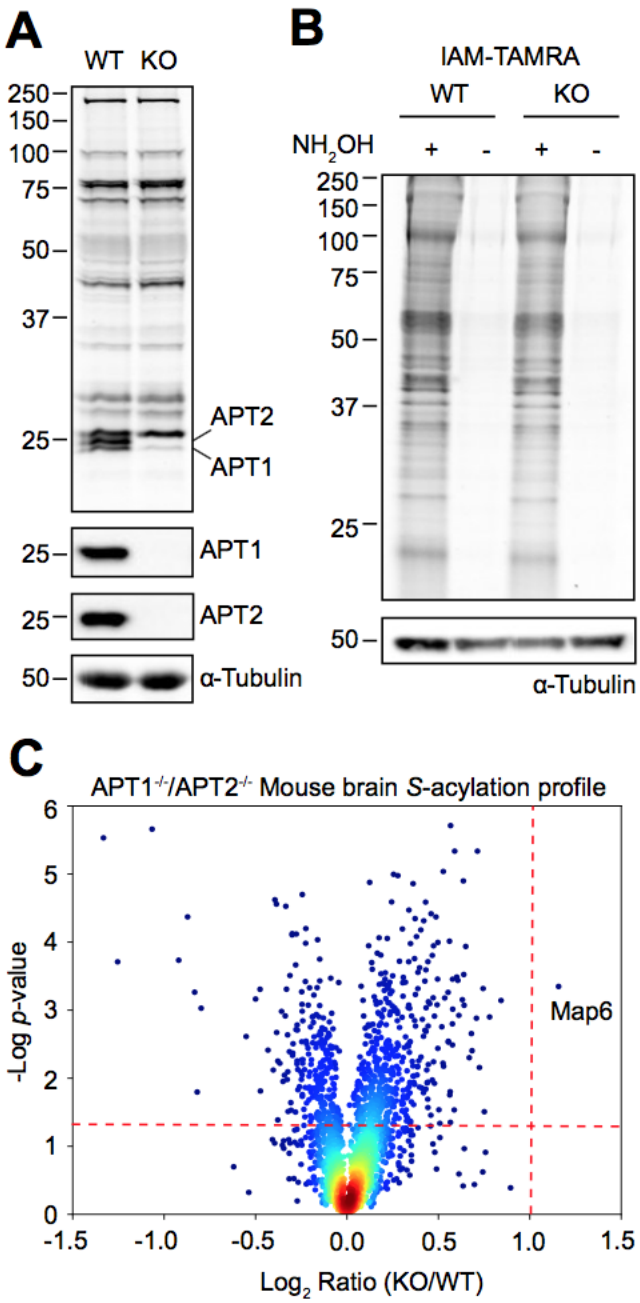

Figure 4.10 Steady-state S-palmitoylation is unaffected in APT1$^{-/-}$/APT2$^{-/-}$ mouse brains.

(A) FP-TAMRA labeling of active serine hydrolases in whole mouse brain homogenates confirms selective deletion of APT1 and APT2. Knockout was also confirmed by western blot. (B) Hydroxylamine-switch analysis of *S*-palmitoylation in normal and knockout samples does not reveal major changes in S-acylation profiles. (C) Volcano plot analysis of acyl-RAC enrichment and multiplexed TMT mass spectrometry analysis of APT1$^{-/-}$/APT2$^{-/-}$ whole mouse brain homogenates (N=3). Red lines represent $p < 0.05$ from two-tailed Student's t-test with unequal variance (horizontal) and 2-fold change (vertical).

Discussion

S-palmitoylation is widely presented as a dynamic modification, yet due to technical challenges, there has been little progress towards profiling proteome-wide dynamics. Here we establish a method for temporal profiling, and confirm a direct correlation between dynamic *S*-palmitoylation and the rate of fatty acid incorporation. We anticipate this multiplexed mass spectrometry approach will significantly impact the analysis of the *S*-palmitoylation cycle, including further annotation of select depalmitoylases, zDHHC protein acyl transferases, and signal-dependent regulation. Since zDHHC enzymes often share common substrates[16], this approach could provide an opportunity to bypass steady-state compensatory effects and assign substrates based on kinetic signatures of fatty acid incorporation. Such analysis could be complicated by acyl-CoA substrate preferences among zDHHC enzymes[4], but provides a platform to profile incorporation of different alkynyl fatty acid derivatives across the proteome.

We recently demonstrated HDFP treatment redistributes G_{α}s randomly across internal membranes, independent of GPCR activation. [23] This corresponds to similar to analysis of NRAS random distribution after treatment with the promiscuous depalmitoylase inhibitor Palmostatin B.[61] Based on our comparative acyl-RAC and 17-ODYA profiling, we propose a model where depalmitoylase inhibition can affect the rate of fatty acylation, yet maintain relatively constant steady state *S*-palmitoylation levels. Accordingly, when the *S*-palmitoylation cycle is stalled, the functional affect may not be a shift in steady-state *S*-acylation, but instead a release from the vesicular flux and random localization across internal membranes. Alternatively, metabolic labeling approaches may only access a limited fraction of the total *S*-palmitoylated protein, and diminish any affects measured by bulk analysis. Clearly, the profile of 17-ODYA labeled proteins appears quite different than gel-based analysis using hydroxylamine-switch methods. Furthermore, while HDFP treatment stimulates 17-ODYA incorporation, the fraction labeled may only represent a minor fraction of the bulk *S*-palmitoylated form. While several studies have reported changes in *S*-palmitoylation of select targets by acyl-RAC after APT inhibition [156], these effects may be cell line dependent.[75] APT enzymes represent only a fraction of depalmitoylase activity in 293T cells, suggesting

significant compensation from other uncharacterized enzymes. [102] While clarifying the HDFP-sensitive enzymes involved in this effect is ongoing, this compensation may be linked to ABHD17 family depalmitoylases. The development of potent and selective ABHD17 inhibitors will begin to address these questions, while avoiding technical challenges in deriving ABHD17A, ABHD17B, and ABHD17C triple knockout cells, particularly when knockout of individual members reduces cell viability across many cancer cell lines. [159] Alternatively, addition of azido-fatty acids to cells stimulates biosynthesis of CoA conjugates. [4] The data presented here suggests steady-state *S*-palmitoylation is not greatly affected by addition of bioorthogonal fatty acids, depalmitoylase inhibitors, or genetic deletion of depalmitoylases, whether or not they modulate acyl-CoA levels in cells.

APT enzymes have been studied nearly exclusively in cancer cell models, where APT1 and APT2 inhibition represses oncogenic signaling and stem cell-like features by modulating lateral polarity complexes[75] and asymmetric cell division[160]. Surprisingly, APT1$^{-/-}$/APT2$^{-/-}$ mice are viable and have no overt developmental defects. While detailed analysis of these mutant mice will require more focused effort, cursory analysis suggests APT enzymes may exclusively exert their effects only in specific cell contexts to support tumorigenesis. [43, 160] Since APT1$^{-/-}$/APT2$^{-/-}$ mice have no measureable changes in steady-state *S*-palmitoylation, it is unclear how relevant these enzymes are to regulating *S*-palmitoylation dynamics over other lipid hydrolase activities. [65]

Overall, the methods and analyses presented reveal the kinetic profile of *S*-palmitoylation in cells, revealing new insights to proteins linked to dynamic *S*-palmitoylation cycles. These methods reveal potential limitations of steady-state analysis while presenting new opportunities for temporal profiling of *S*-palmitoylation.

Materials and Methods

Cell Lines

Human 293T cells were cultured in Dulbecco's Modified Eagle Media (DMEM / Invitrogen) supplemented with 1 % (v / v) 10000 Units / mL penicillin-streptomycin (Invitrogen), 4.5 g / L D-Glucose, 2 mM L-Glutamine, 110 mg / L sodium pyruvate, and 10 % (v / v) dialyzed fetal bovine serum (JR Scientific). HAP1 cells were a generous gift

from Gisou van der Goot (EPFL), and were cultured in Iscove′s Modified Dulbecco′s Medium (IMDM / Invitrogen) supplemented with 1 % (v / v) 10000 Units / mL penicillin-streptomycin, and 10 % (v / v) dialyzed fetal bovine serum. Jurkat cells were grown in Roswell Park Memorial Institute (RPMI) 1640 (Invitrogen) supplemented with 2.383 g / L HEPES buffer, 1.5 g / L sodium bicarbonate, 1 % (v / v) 10000 Units / mL penicillin-streptomycin, 4.5 g / L D-glucose, 2 mM L-Glutamine, 110 mg / L sodium pyruvate, and 5 % (v / v) dialyzed fetal bovine serum. There was no additional effort to authenticate these cell lines, since the morphological characteristics matched signatures for each cell line.

Mice

Lypla1 (APT1) knockout mice were generated by purchasing the cryopreserved TF1704 model from Taconic Biosciences. C57BL/6NTac females were impregnated with cryopreserved sperm from a mixed C57BL/6-129/SvEv background harboring a gene-trap (“gt”) cassette between Lypla1 exons 2 and 3. After intercrossing, western blot and gel- and mass-spec-based experiments with FP probes confirmed complete loss of APT1 protein in Lypla1$^{gt/gt}$ mice. Lypla2 (APT2) knockout mice were generated by acquiring cryopreserved sperm from the KOMP repository at UC Davis harboring the Lypla2$^{tm1a(KOMP)Mbp}$ “knockout-first” gene-trap cassette which was inserted between exons Lypla2 1 and 2. Homozygous Lypla2$^{gt/gt}$ mice were found to retain ~20% residual APT2 expression via gel- and mass-spec-based experiments with FP-probes. Complete ablation of APT2 protein was achieved by crossing Lypla2$^{gt/gt}$ mice with a C757BL/6 mouse line with ubiquitous expression of Cre recombinase (Taconic #12524) which resulted in removal of Lypla2 exons 2-10 from the genome. The resulting Lypla2$^{Cre/Cre}$ mice were confirmed to have no residual APT2 protein expression, as measured by gel- and mass-spec based experiments with FP probes. Lypla1/Lypla2 (APT1/APT2) double knockout mice were generated by crossing Lypla1$^{gt/gt}$ mice with Lypla2$^{gt/gt}$ mice. The resulting Lypla1$^{gt/gt}$;Lypla2$^{gt/gt}$ mice were then crossed with a ubiquitous Cre deleter line (Taconic #12524) to accomplish removal of Lypla2 exons 2-10 and complete ablation of APT2 expression.

Metabolic labeling and inhibitor treatments

17-ODYA labeling was performed as described previously[28]. HDFP, ML348, and ML349 syntheses were previously reported [28, 103]. Other inhibitors were purchased from Sigma (2-bromohexadecanoic acid, TVB-3166, and ABC44) or Cayman (JW480, WWL229, and WWL70). At ~90 % confluency, the growth media was aspirated and the new media containing 25 µM cycloheximide (Sigma) and the inhibitor was added to the cells (Control = 0.1% v / v DMSO final). For ABPP and acyl-RAC proteomic experiments, cells were incubated with HDFP for 3 hours. After incubation, 20 µM 17-ODYA (Cayman) was added. At different time points, cells were washed with cold DPBS (Invitrogen) and scraped off the plate. The cell pellets were washed with DPBS and stored at -80 °C.

17-ODYA click chemistry and enrichment

17-ODYA detection in cell homogenates was performed as previously described[28]. Frozen cell-pellets were resuspended in DPBS and lysed by sonication. For in-gel fluorescence analysis, 50 µg of protein (quantified using the BCA protein assay kit; Bio-Rad) was incubated with 1 mM tris(2-carboxyethyl)phosphine (TCEP;Sigma), 20 µM TAMRA azide (Click Chemistry Tools), 1 mM $CuSO_4$, and 100 µM Tris((1-benzyl-1H-1,2,3-triazol-4-yl)methyl)amine (TBTA; Cayman) for 1 hour at room temperature. The samples were resolved by 12 % SDS-PAGE (180 V;1 hr) and imaged using Azure C600 (Azure Biosystems). Samples prepared for mass spectrometry analysis included 1 biological replicate per time point (palmitic acid as time 0) for each condition (DMSO or 1 µM HDFP). The sonicated homogenate was separated into soluble (S100) and insoluble (P100) fractions by ultracentrifugation at 100,000g for 45 min. 1 mg of the P100 fraction was incubated with the click chemistry reagents listed above, except Biotin PEG3 Azide (500 µM; Click Chemistry Tools) was substituted for TAMRA azide. After 1 hour, proteins were extracted with methanol and chloroform (4 eq. aqueous, 4 eq. methanol, 1 eq. chloroform). The insoluble pellet was washed with methanol and resuspended in 6 M urea / 2% SDS in PBS. Protein concentrations normalized again across all samples. Samples were then incubated with 5 mM TCEP (pH 7) for 30 min, followed by addition of 20 mM iodoacetamide for 1 hour in dark. The samples were diluted 3-fold and the same amount of protein was added to 75 µL of pre-washed Streptavidin beads (Thermo) for 90 minutes. The beads were washed 5 times with PBS

containing 2 M urea and 0.2 % SDS and 5 more times in PBS. Finally, the beads were resuspended in 100 µL of 50 mM triethylammonium bicarbonate (TEAB) and 1.3 µg of mass spectrometry-grade Trypsin/Lys C mix (Promega). After overnight digestion at 37 °C, the eluted peptides were incubated with TMT 6plex (Thermo) reagents according to the manufacturer's protocols. The samples were mixed into 1 tube, desalted with an Oasis PRIME HLB µElution Plate (Waters), dried using a Thermo Savant SpeedVac, and stored at -80 °C.

Serine Hydrolase Activity-based Profiling

Cells were incubated with inhibitors in culture, the harvested and lysed by sonication. For fluorescent gel-based analysis, 50 µg of protein was incubated with 2 µM fluorophosphonate (FP)-TAMRA [161] for 30 minutes. For the proteomic analysis, 4 biological replicates per condition (20 µM HDFP, 1 µM HDFP, DMSO) were used and 2 of each condition was combined into 1 TMT 6plex run. 1 mg of whole cell lysate was incubated with 5 µM FP-biotin for 1 hour at room temperature. The streptavidin enrichment and mass spectrometry sample preparation procedures are identical to the 17-ODYA enrichment sample preparation.

Acyl-RAC

The cell pellets were resuspended in Buffer 1 (50 mM HEPES pH 7.4, 1 mM EDTA, 100 mM NaCl), sonicated, and fractionated by centrifugation at 100,000g for 45 minutes at 4 °C. The insoluble fraction was resuspended in Buffer 2 (50 mM HEPES pH 7.4, 2 % SDS) and quantified with BCA protein assay kit. 1~2 mg of protein was diluted in 1 mL of Buffer 3 (50 mM HEPES pH 7.4, 6 M urea, 1 mM EDTA, 2 % SDS) and incubated with 10 mM TCEP for 30 minutes at room temperature, followed by 50 mM iodoacetamide for 1 hour in dark. The proteins were precipitated by chloroform / methanol extraction (as above) and resuspended in Buffer 2 and re-quantified. For the hydroxylamine-switch gel-based analysis, 0.5 M neutralized hydroxylamine was added to each sample and incubated for 15 minutes, followed by 1 µM Tetramethylrhodamine-5-Iodoacetamide Dihydroiodide (5-TMRIA (noted IAM-TAMRA); Thermo) for 30 minutes. For the enrichment analysis, the reduced and alkylated proteins (>1 mg) were added to the 100 µL of water-activated, pre-washed Thiopropyl-Sepharose 6B beads (Sigma) in Buffer 3, followed by the addition of 0.5 M hydroxylamine. The samples were

incubated for 2 hours at room temperature and washed 5 times with Buffer 2 and washed 5 more times in 50 mM HEPES. For the western-blot analysis, beads were resuspended in the 1X loading buffer (10% glycerol, 62.5 mM tris pH 6.8, 1% 2-mercaptoethanol, 0.05% bromophenol blue, and 1% SDS) and heated for 5 minutes at 90 °C. The supernatant analyzed by SDS-PAGE. For the proteomic analysis, 4 biological replicates per condition (DMSO, +HDFP, +HDFP&17-ODYA) were used. Two of each condition were combined into one TMT 6plex run. The beads were resuspended in 50 mM TEAB and incubated with Trypsin/Lys C mix (Promega) at 37 °C overnight. The supernatants were TMT labeled and desalted as above. For the mouse brain samples, 3 experimental replicates per condition (WT or APTs KO) was combined into one TMT 6plex run. Tissue was washed in Buffer 1, then dounce homogenized at 4 °C. The lysate was briefly centrifuged at 1000g for 5 minutes to remove debris, fractionated and processed for the proteomic sample preparation as above.

Western blot

Gels were transferred to methanol-activated Immobilon-FL membrane (Millipore) in the transfer buffer (25 mM Tris-base,192 mM glycine, 10 % methanol) at 75 V for 2 hours. Proteins were probed with anti-alpha tubulin (1:1000; Sigma #T6074), anti-APT1 (1:500; Millipore; #MABS166), anti-APT2 (1:500; Thermo; #PA-527653), anti-Pan Ras (1:1000; Millipore; #05-516), or anti-Scrib (1:1000; Millipore; #MAB1820) for 16 hours at 4 °C and then incubated with secondary anti-mouse horseradish peroxidase (HRP;1:1000; Thermo; #32430) for 1 hour at room temperature. Blots were developed by West Pico Chemiluminescent Substrate (Thermo) and then the chemiluminescence was detected by Azure c600 imager (Azure Biosystems).

Mass spectrometry and data analysis

In order to obtain superior quantitation accuracy, multinotch-MS3 methods were used to reduce reporter ion interference[162]. Analysis was performed using an Orbitrap Fusion (Thermo Fisher Scientific) and RSLC Ultimate 3000 nano-UPLC (Dionex). Samples were resuspended in 9 μl of 0.1% formic / acetonitrile and 2 μl of each sample was resolved using a nano-capillary reverse phase column (Acclaim PepMap C18, 2 micron, 75 μm i.d. x 50 cm, Thermo Scientific). A 0.1% formic / acetonitrile gradient was used with 300 nl / min flow (2-22% acetonitrile in 150 min; 22-32% acetonitrile in 40 min; 20

min wash at 90% followed by 50 min re-equilibration) and directly sprayed on to Orbitrap Fusion using EasySpray source (ThermoFisher Scientific). The mass spectrometer was programmed to collect one MS1 scan (Orbitrap; 120K resolution; AGC target $2x10^5$; max IT 100 ms) followed by data-dependent, "Top Speed" (3 seconds) MS2 scans (collision induced dissociation; ion trap; NCD 35; AGC $5x10^3$; max IT 100 ms). For multinotch-MS3, top 10 precursors from each MS2 were fragmented by HCD followed by Orbitrap analysis (NCE 55; 60K resolution; AGC $5x10^4$; max IT 120 ms, 100-500 m/z scan range). Proteome Discoverer (PDv2.1; Thermo Fisher) was used for data analysis, except in HAP1 dataset where the raw abundances were used. MS2 spectra were searched against either Uniprot human protein database (release 08/02/2017) or SwissProt mouse protein database (release 04/13/2016) using the following search parameters: MS1 and MS2 tolerance were set to 10 ppm and 0.6 Da, respectively; carbamidomethylation of cysteines (57.02146 Da) and TMT labeling of lysine and N-termini of peptides (229.16293 Da) were considered static modifications; oxidation of methionine (15.9949 Da) and deamidation of asparagine and glutamine (0.98401 Da) were considered variable; maximum missed cleavage was set to 2. During the search, parsimony principle (unique+razor peptides) was applied. Identified proteins and peptides were filtered to retain only those that passed ≤1% FDR threshold. Quantitation was performed using high-quality MS3 spectra (Average signal-to-noise ratio of 6 and <40% isolation interference). For all biotin-streptavidin enrichment samples, data are normalized to Pyruvate carboxylase, an endogenously biotinylated protein. For the acyl-RAC samples, data were normalized to all proteins using the PDv2.1. For the 17-ODYA time course data, threshold was set to >2 PSMs, >2-fold ratio enrichment during the last 3 time points (compared to the palmitic acid control) to be considered as significant. The hierarchical clustering was performed with Cluster 3.0,[163] with the averaged linkage method selecting the Pearson correlation coefficient as the similarity metric. For the acyl-RAC data, threshold was set to >2 PSMs, >2 fold change, and multiple identifications in the SwissPalm[30] database. Statistical analysis was performed in Excel. Graphs were generated using the Graphpad Prism 7 (Graphpad Software), PyCharm (JetBrains), and Anaconda (Anaconda).

Quantification and statistical analysis

All protein quantitation from the mass spectrometry experiments were performed by Proteome Discoverer v.2.1 (Thermo) and further processed by Excel, Graphpad Prism 7, and PyCharm, as described above. Protein band densitometry analyses were quantified using ImageJ software (NIH). Statistical details of experiments and the sample size can be found in the figure legend and the supplemental tables.

Individual Contributions

Sang Joon Won performed all experiments. Sang Joon Won and Brent Martin designed all experiments and wrote the manuscript.

Acknowledgments

We would like to thank Abide Therapeutics for generously providing APT1$^{-/-}$/APT2$^{-/-}$ mouse tissues, Gisou van der Goot (EPFL) for providing HAP1 cells, Venkatesha Basrur (University of Michigan) for assistance with mass spectrometry, and Sarah Haynes (University of Michigan) for bioinformatics support. Financial support was provided by the National Institutes of Health DP2 GM114848 and the University of Michigan.

Table 4.1 Temporal profiling of 17-ODYA labeling in 293T cells., related to figure 4.6

Uniprot Accession	Description	# Peptides	# PSMs	# Unique Peptides	cluster #	17ODYA incorporation rate	# of palmitome studies
P08754	Guanine nucleotide-binding protein G(k) subunit alpha	5	7	2	1	Fast	21
P24539	ATP synthase F(0) complex subunit B1, mitochondrial	3	4	3	1	Fast	4
Q969X5	Endoplasmic reticulum-Golgi intermediate compartment protein 1	3	3	3	1	Fast	9
Q7Z434	Mitochondrial antiviral-signaling protein	2	4	2	1	Fast	2
P01111	GTPase NRas	3	5	3	1	Fast	19
Q5JWF2	Guanine nucleotide-binding protein G(s) subunit alpha isoforms XLas	7	12	6	1	Fast	9
Q86UE4	Protein LYRIC	12	16	12	1	Fast	23
P43304	Glycerol-3-phosphate dehydrogenase, mitochondrial	7	14	7	2	slow	4
O00161	Synaptosomal-associated protein 23	4	6	4	2	slow	23
P61586	Transforming protein RhoA	3	4	2	2	Fast	9
Q00765	Receptor expression-enhancing protein 5	4	6	4	2	slow	14
O95831	Apoptosis-inducing factor 1, mitochondrial	10	15	10	2	medium	4
O14880	Microsomal glutathione S-transferase 3	4	8	4	2	slow	7
Q02978	Mitochondrial 2-oxoglutarate/malate carrier protein	5	8	5	2	slow	7
P61586	Transforming protein RhoA	3	4	2	2	Fast	9
Q14254	Flotillin-2	4	5	4	3	Fast	18
P62873	Guanine nucleotide-binding protein G(I)/G(S)/G(T) subunit beta-1	3	6	3	3	Fast	7
P20073	Annexin A7	2	4	2	3	Fast	3
P61026	Ras-related protein Rab-10	6	13	3	3	Fast	10
Q14160	Protein scribble homolog	3	5	3	3	Fast	15
P35610	Sterol O-acyltransferase 1	3	4	3	3	Fast	3
P12235	ADP/ATP translocase 1	15	25	2	4	slow	12
P12236	ADP/ATP translocase 3	18	32	2	4	slow	13
O43169	Cytochrome b5 type B	3	6	3	4	slow	16

Temporal profiling of 17-ODYA labeling in 293T cells. Cells were incubated with cycloheximide and HDFP or DMSO. Then incubated with 17-ODYA for varying amounts of time. Enriched proteins from each time point were labeled with 6plex TMT then combined into 1 sample. Protein abundances are normalized to pyruvate carboxylase. PSM= peptide spectrum matches. Ratio=relative enrichment compared to palmitic acid control (t=0) in each condition. Normalized ratio refers to the raw ratio normalized to the highest enrichment ratio across all time points and conditions (+/- HDFP), which was used in the paired-clustering analysis to generate cluster # as described in the main figure (Figure 2a). "17ODYA incorporation rate without HDFP" (related to Figure S3b) refers to the overall rate of 17ODYA incorporation within the DMSO conditions after a separate hierachical clustering analysis.

Table 4.2 Temporal profiling of 17-ODYA labeling in HAP1 cells, related to figure 4.7

Uniprot Accession	Description	# Peptides	# PSMs	# Unique Peptides	Cluster #	# of palmitome studies
Q86UE4	protein LYRIC	19	44	19	1&2	23
P57088	Transmembrane protein 33	4	7	4	1&2	6
Q9Y277	Isoform 2 of Voltage-dependent anion-selective channel protein 3	10	25	9	1&2	10
P61009	Signal peptidase complex subunit 3	2	5	2	1&2	3
P61586	Transforming protein RhoA	2	5	2	1&2	9
Q9H3N1	Thioredoxin-related transmembrane protein 1	9	21	9	1&2	22
P61619	Protein transport protein Sec61 subunit alpha isoform 1	6	12	6	1&2	4
Q9Y6C9	Mitochondrial carrier homolog 2	3	7	3	1&2	6
Q9UHG3	prenylcysteine oxidase 1	4	5	4	1&2	3
Q99536	Synaptic vesicle membrane protein VAT-1 homolog	8	14	8	1&2	6
O75844	caax prenyl protease 1 homolog	8	17	8	1&2	4
O00161	Synaptosomal-associated protein 23	5	11	5	1&2	23
P29966	Myristoylated alanine-rich C-kinase substrate	8	17	7	3	4
P46977	Dolichyl-diphosphooligosaccharide--protein glycosyltransferase subunit STT3A	4	8	3	3	5
P49006	MARCKS-related protein	7	15	6	3	3
Q16891	Isoform 2 of MICOS complex subunit MIC60	20	39	1	3	5
Q14254	Flotillin-2	8	11	8	3	18
Q01650	large neutral amino acids transporter small subunit 1	4	10	4	3	3
Q9UL46	proteasome activator complex subunit 2	3	5	3	3	6
P31930	Cytochrome b-c1 complex subunit 1, mitochondrial	4	5	4	3	6
P60953	Cell division control protein 42 homolog	3	6	3	3	10
Q9UJS0	Isoform 2 of Calcium-binding mitochondrial carrier protein Aralar2	10	18	10	3	2
Q9Y5M8	signal recognition particle receptor subunit beta	5	10	5	3	7
Q5JWF2	Guanine nucleotide-binding protein G(S) subunit alpha isoforms XLas	8	19	7	3	9

Representative proteins from each cluster are shown.

Table 4.3 HDFP and 17-ODYA do not change steady-state S-palmitoylation in 293T cells, related to figure 4.8

Uniprot Accession	Description	# Peptides	# PSMs	# Unique Peptides	Ratio (HDFP/Vehicle)	Ratio (HDFP_17OD/Vehicle)	p-value (HDFP/Vehicle)	p-value (HDFP+7ODYA)/(Vehicle)	# of palmitome studies
P01111	GTPase NRas	6	8	6	1.06	1.10	0.58	0.36	19
Q14254	Flotillin-2	4	6	4	1.06	1.04	0.91	0.95	18
Q5JWF2	Guanine nucleotide-binding protein G(s) subunit alpha isoforms XLas	3	8	2	1.05	1.06	0.53	0.51	9
P61586	Transforming protein RhoA	5	11	5	1.02	1.08	0.86	0.44	9
P04075	Fructose-bisphosphate aldolase A	23	161	23	0.99	0.96	0.91	0.64	10
P13639	Elongation factor 2	41	142	40	0.98	1.00	0.45	0.93	11
P68104	Elongation factor 1-alpha 1	18	113	9	0.97	0.94	0.56	0.25	11
P11142	Heat shock cognate 71 kDa protein	27	110	21	1.00	0.97	0.99	0.60	10
P07437	Tubulin beta chain	18	86	3	0.98	0.98	0.84	0.82	7
P60709	Actin, cytoplasmic 1	16	80	7	1.00	0.97	0.95	0.28	8
P09874	Poly [ADP-ribose] polymerase 1	38	78	38	1.00	1.00	1.00	0.98	3
P14618	Pyruvate kinase PKM	29	78	29	0.99	1.01	0.92	0.94	8
P49327	Fatty acid synthase	40	78	40	0.99	0.98	0.89	0.85	12
P68371	Tubulin beta-4B chain	18	78	3	0.98	0.98	0.75	0.60	8
P06733	Alpha-enolase	22	77	22	0.99	0.97	0.73	0.36	10
P04406	Glyceraldehyde-3-phosphate dehydrogenase	18	75	18	0.93	0.91	0.16	0.03	13
Q71U36	Tubulin alpha-1A chain	22	74	1	1.02	1.06	0.97	0.89	5
P34932	Heat shock 70 kDa protein 4	32	69	29	1.01	0.97	0.82	0.30	6
P00338	L-lactate dehydrogenase A chain	18	67	17	0.96	0.95	0.76	0.75	8
P08238	Heat shock protein HSP 90-beta	26	66	12	1.00	0.98	0.99	0.93	6
P07900	Heat shock protein HSP 90-alpha	24	64	12	0.99	0.99	0.94	0.89	6
P22314	Ubiquitin-like modifier-activating enzyme 1	24	62	24	1.01	0.98	0.93	0.85	9
Q00839	Heterogeneous nuclear ribonucleoprotein U	27	61	27	1.00	0.99	0.93	0.89	5
Q9H3N1	Thioredoxin-related transmembrane protein 1	8	13	8	0.97	1.08	0.90	0.67	22

Representative proteins are shown. HDFP and 17-ODYA do not change steady-state S-palmitoylation levels in 293T cells. Cells are treated with HDFP or HDFP and 17-ODYA for 3 hours, followed by acyl-RAC enrichment and TMT quantitative proteomics. All conditions are treated with hydroxylamine (HA). PSM= peptide spectrum matches, N=4 biological replicates.

Table 4.4 HAP1 cell steady-state S-palmitoylation, related to figure 4.9

Uniprot Accession	Description	# Peptides	# PSMs	# Unique Peptides	Ratio_raw abundance (HA/Vehicle)	Ratio_raw abundance (HA+HDFP/Vehicle)	log 2 Ratio (HA/Vehicle)	log 2 Ratio (HA+HDFP/Vehicle)	p-value (HA/Vehicle)	p-value (HA+HDFP/Vehicle)	# of palmitome studies
P01111	GTPase NRas	9	20	3	19.46	20.59	4.28	4.36	4.91E-05	6.43E-04	19
P01112	GTPase HRas	8	19	2	12.68	14.13	3.66	3.82	2.24E-02	2.62E-02	18
Q86UE4	protein LYRIC	6	9	6	15.22	14.56	3.93	3.86	5.64E-06	3.84E-04	23
Q14160	Isoform 3 of Protein scribble homolog	5	8	4	6.73	7.61	2.75	2.93	1.70E-02	3.22E-02	15
P61586	Transforming protein RhoA	5	14	2	4.36	4.01	2.13	2.00	7.17E-04	5.27E-04	9
O00161	Synaptosomal-associated protein 23	8	24	8	141.91	142.97	7.15	7.16	8.22E-05	1.19E-03	23
Q86UE4	protein LYRIC	6	9	6	15.22	14.56	3.93	3.86	5.64E-06	3.84E-04	23
Q14254	Flotillin-2	19	48	19	32.49	34.33	5.02	5.10	1.43E-04	1.26E-03	18
P61225	ras-related protein Rap-2b	5	15	3	327.99	344.31	8.36	8.43	5.98E-04	4.44E-04	23
P10114	Ras-related protein Rap-2a	3	10	1	310.61	316.96	8.28	8.31	3.97E-04	2.19E-04	19
Q8NHG7	Small VCP/p97-interacting protein	2	4	2	204.42	188.07	7.68	7.56	2.01E-03	3.39E-04	7
O00161	Synaptosomal-associated protein 23	8	24	8	141.91	142.97	7.15	7.16	8.22E-05	1.19E-03	23
Q5871 9	vesicle transport protein SFT2C	1	4	1	96.41	93.86	6.59	6.55	1.53E-03	5.53E-03	10
Q03135	Caveolin-1	4	12	4	78.78	83.37	6.30	6.38	6.13E-03	1.13E-02	8
P52815	39S ribosomal protein L12, mitochondrial	4	18	4	74.90	91.21	6.23	6.51	2.12E-04	6.66E-04	3
P78368	casein kinase I isoform gamma-2	5	9	2	74.04	72.25	6.21	6.17	9.01E-04	4.86E-04	12
Q6IAA8	ragulator complex protein LAMTOR1	4	15	4	68.49	69.42	6.10	6.12	9.40E-03	5.01E-03	18
Q9NRR3	CDC42 small effector protein 2	1	6	1	64.61	67.09	6.01	6.07	1.36E-02	2.26E-02	11
Q01628	Interferon-induced transmembrane protein 3	1	4	1	55.49	59.77	5.79	5.90	1.59E-03	1.78E-04	12
O15162	phospholipid scramblase 1	4	8	4	54.98	56.47	5.78	5.82	8.65E-05	2.19E-03	15
P29992	guanine nucleotide-binding protein subunit alpha-11	11	25	6	54.46	54.39	5.77	5.77	1.27E-04	1.79E-04	19
P15151	Poliovirus receptor	2	4	2	50.69	55.33	5.66	5.79	1.17E-03	1.33E-04	9
P27105	erythrocyte band 7 integral membrane protein	5	11	5	46.32	46.14	5.53	5.53	9.40E-03	4.31E-03	15
P49795	Regulator of G-protein signaling 19	2	4	2	46.08	50.40	5.53	5.66	8.78E-02	5.56E-02	11

Representative proteins are shown. Cells are treated with HDFP for 3 hours in the indicated condition, and enriched by acyl-RAC methods. HA = 0.5 M hydroxylamine. N=4 biological replicates. In the vehicle conditions, no hydroxylamine (HA) was added during preparation.

Table 4.5 Steady-state S-palmitoylation profiling in APT1/APT2 knockout mouse brain, related to figure 4.10

Uniprot Accession	Description	# Peptides	# PSMs	# Unique Peptides	Ratio (KO/WT)	log2 Ratio	Negative log p-value	p-value	# of palmitome studies
P08556	GTPase NRas	10	17	2	0.99	-0.02	0.23	5.90E-01	19
P32883	Isoform 2B of GTPase KRas	9	13	3	0.96	-0.06	0.48	3.31E-01	
Q80WJ7	protein LYRIC	3	3	3	0.95	-0.07	0.38	4.21E-01	23
Q61411	GTPase HRas	11	21	3	0.89	-0.17	2.94	1.16E-03	
Q9QUI0	Transforming protein RhoA	9	20	7	0.94	-0.09	2.24	5.75E-03	9
Q7TSJ2	Microtubule-associated protein 6	33	44	33	2.23	1.16	3.35	4.49E-04	
Q9JIG8	PRA1 family protein 2	3	4	3	1.47	0.55	2.54	2.87E-03	12
Q9DBJ1	Phosphoglycerate mutase 1	2	3	2	1.44	0.53	2.17	6.69E-03	7
Q60634	Flotillin-2	16	24	1	0.97	-0.04	0.70	1.97E-01	
Q61171	Peroxiredoxin-2	2	4	2	1.28	0.35	2.91	1.22E-03	5
P18760	Cofilin-1	8	12	6	1.25	0.32	3.41	3.88E-04	8
P39053	Dynamin-1	21	29	1	1.23	0.30	1.61	2.44E-02	
Q9DCT8	Cysteine-rich protein 2	5	7	5	1.21	0.28	2.34	4.62E-03	
P49817	Caveolin-1	6	8	6	1.15	0.20	3.01	9.81E-04	8
P62962	profilin-1	6	10	6	1.15	0.20	2.12	7.58E-03	8
Q8K021	Secretory carrier-associated membrane protein 1	6	13	6	1.23	0.30	4.19	6.42E-05	23
O09044	Synaptosomal-associated protein 23	7	13	6	1.10	0.14	0.80	1.59E-01	23
P35564	Calnexin	1	1	1	1.06	0.09	0.47	3.39E-01	23
P08752	guanine nucleotide-binding protein G(i) subunit alpha-2	15	44	8	1.05	0.08	1.33	4.63E-02	23
O35609	Secretory carrier-associated membrane protein 3	5	7	5	0.96	-0.06	0.75	1.76E-01	22
P21278	guanine nucleotide-binding protein subunit alpha-11	14	23	9	0.91	-0.14	2.03	9.34E-03	22
P21279	Guanine nucleotide-binding protein G(Q) subunit alpha	13	25	8	0.89	-0.16	1.83	1.49E-02	22
P51912	Neutral amino acid transporter B(0)	1	1	1	1.11	0.16	0.80	1.60E-01	19
Q9ERN0	Secretory carrier-associated membrane protein 2	2	2	2	1.11	0.15	0.76	1.74E-01	19

Representative proteins are shown. N=3, experimental replicates. All conditions are treated with hydroxylamine.

Chapter 5 : Conclusions and Future Directions

Conclusions

Protein depalmitoylases are hypothesized to distinguish between different substrates, which together impact the global *S*-palmitoylation cycle. To test this hypothesis, my dissertation focuses the structure and function of the annotated depalmitoylases, APT1 and APT2. In order to reveal the mechanism of APT1 and APT2 orthogonality, I solved the co-crystal structures of these enzymes bound to their isoform-selective inhibitors. This analysis identified remarkably similar active sites while divergently conserved residues promoted inhibitor selectivity. Although the static crystal structures do not shed light on the molecular mechanism for the functional orthogonality of APT1 and APT2, we characterized acyl-binding channel to gain insight into their mode of action.[103]

Since ML349 can attenuate MAPK signaling in cells, I sought to confirm that APT2 was indeed the major cellular target in cells. To accomplish this, I profiled ML349 binding partners, and identified several low affinity-multimeric targets with no obvious biological significance to cellular growth signaling.[84] Based on these experiments, ML349 is a robust inhibitor of APT2 for selective analysis of APT2 function in cells. This analysis also highlights how multimeric proteins can emerge from affinity proteomics studies through avidity-driven interactions.

The development of alkynyl fatty acids coupled with advanced mass spectrometry have enabled proteome-wide analysis of *S*-palmitoylation. Despite our previous efforts,[28, 43] *S*-palmitoylation regulation remains poorly understood. For example, there is no broad understanding of the substrates of either zDHHC protein acyl transferases or APT enzymes. This is complicated by potentially redundant functions of these enzymes, which may lead to compensation in germline knockout organisms. In profiling experiments, cells may reach a steady state level of *S*-palmitoylation by the time of analysis, blinding the dynamic rate of turnover.

In order to profile enzymatic depalmitoylation, I developed a multiplexed proteomics analysis to assay hundreds of proteins over a series of timepoints following alkynyl fatty acid labeling. This analysis revealed different *S*-acylation kinetics across hundreds of proteins, and identified distinct acylation rates correlated with rapid depalmitoylation. Overall, this analysis confirms a significant role for protein depalmitoylases in regulating *S*-palmitoylation dynamics. Surprisingly, APTs had no significant impact in the overall steady-state *S*-palmitoylation in cells. Treatment with more selective inhibitors or analysis of APT1$^{-/-}$APT2$^{-/-}$ double knockout mouse showed no major effects on steady-state *S*-palmitoylation, suggesting dynamics may be more challenging to analyze than previously imagined. Nonetheless, I established a new method to profile depalmitoylase-dependent dynamic changes in protein *S*-palmitoylation.

Although palmitoylation on proteins were discovered 40 years ago, the mechanistic understanding of this modification is just beginning to emerge. In my thesis, used structural biology, inhibitors, and chemical proteomic approaches to enhance understanding of the depalmitoylation events. While these efforts were mainly focused on APTs, other emerging depalmitoylases such as ABHD17s or other unidentified enzymes still require biochemical and cellular functional studies.

Future directions to analyze APT function

What would explain the differential functions of APTs? Some studies have proposed that their localization and expression levels may give a clue.[75, 164] Although APT1 and APT2 show varying expression levels depending on the cell line or disease models,[165] the most convincing explanation comes from the differential localization of APTs. For example, while previous studies reported golgi and cytoplasmic localization of APT1,[20, 61] a recent report showed that APT1 is primarily localized and active in mitochondria while APT2 is mainly found in cytoplasm.[164] However, it is unclear how cells deliver APT1 (and not APT2) to mitochondria, since there is no mitochondrial targeting sequence.

Given this critical information, the next step would be to characterize mitochondrial function of APT1. Since mitochondria are enriched unique lipid classes,

APT1 could potentially regulate lipid homeostasis and also depalmitoylate proteins. To test this hypothesis, one could perform an in-depth metabolomics experiment with purified mitochondria after knockdown or knockout of APT1. Perhaps APT1 acts on palmitoyl carnitine, which cells use to transfer palmitoyl moieties from cytoplasm to the mitochondrial matrix. Since APT1 was originally identified as a lysophospholipase, it could easily be carrying out esterase activity with various substrates in mitochondria. Similarly, one could perform APT1 substrate profiling experiment with purified mitochondrial proteome. Nonetheless, it is intriguing to find that a number of mitochondrial proteins are constantly enriched in palmitoylome data sets. It would be interesting to study which enzymes, if any, catalyze palmitoylation in mitochondria, especially since there are no reported mitochondrial zDHHCs enzymes. Overall, APT1 localization in mitochondria disputes numerous reports claiming that APT1 is a major depalmitoylase for a protein of interest. Perhaps the apparent depalmitoylase activity of APT1 could be due to altered lipid metabolic pathways induced from knockdown or inhibition of APT1. A series of future experiments mentioned above would address this hypothesis.

Once any substrates of APT1 are identified in mitochondria, another series of future studies should address regulatory factors affecting the localization or activity of the APTs. In our affinity proteomics experiments (Chapter 3), we did not identify any stable APT interacting proteins, suggesting any mitochondrial import mechanism may occur through transient, low affinity interactions. To overcome this obstacle, I propose to employ unnatural amino acid photo-crosslinking strategies, followed by mass spectrometry to identify the interacting proteins upon perturbations. Here we could use the crystal structures as a guide to genetically engineer APTs to incorporate unnatural amino acids such as *p*-benzoyl-L-phenylalanine in proximity to the active sites or potential binding sites without affecting the catalytic activity. This may include b4-b5 motif, which is proximal to both the active site and candidate substrate groove (**Figure 1.5 and 5.1**). This motif is unique to APTs and shows a varying degree of conservation between the two enzymes. Furthermore, this motif is in proximity to the lipidated N-terminus, thus potentially interacts with substrates near the membrane. A high throughput *in vitro* screening may be necessary to show that such modification does not

significantly alter the activity of the enzyme. Another point of interest is the groove spanning from the active site of each enzyme (**Figures 2.15 and 5.1**), which may accommodate the peptide portion of acylated substrates.

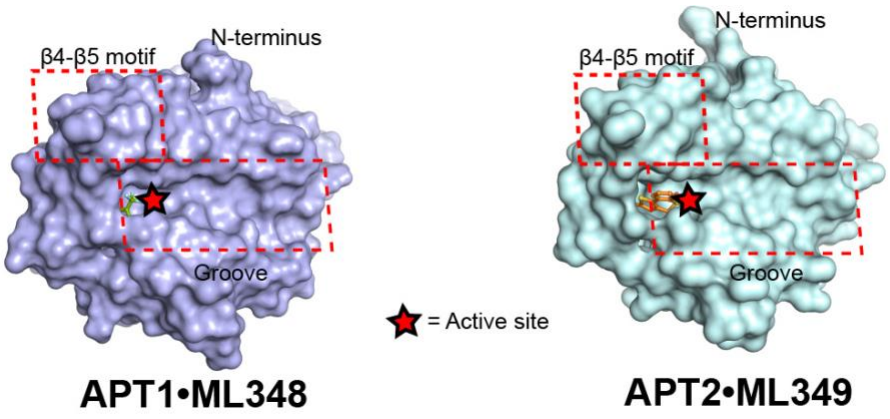

Figure 5.1 Proposed areas of unnatural amino acid incorporation for protein-protein interaction studies.

The red boxes indicate potential sites of mutagenesis for the photo-crosslinking studies.

It would also be useful to solve crystal structures of APTs bound to 16-carbon fluorophosphonate derivatives. This would confirm structural effects imparted by lipid engagement, and potentially help determine the exact site of protein-substrate binding. Additionally, it would be useful to get a better understanding of APT substrates. To accomplish this, I propose synthesis of acylfluorophosphonate derivatives linked to a series of different peptide sequences attached to the fluorophosphonate ethoxy group (**Figure 1.3**). Optimal sequences will react faster, and can be deconvoluted by mass spectrometry of purified APT enzyme. This would allow us to assay substrate selectivity across different enzymes. This library may include partial sequences of reported substrates of APTs such as Scrib or any other top hits from the photo-crosslinking enrichment assays. Alternatively, it may have C-terminus region of NRas as a negative control. Through activity-based high-throughput screening, we may also identify differential sequences preferred by APT1 and APT2, respectively. Overall, these strategies have potential to highlight molecular mechanism for distinct function of APT1 and APT2. The photo-crosslinking method may also highlight how APT1 is transferred to mitochondria if we identify mitochondrial protein translocation machinery.

Furthermore, we cannot rule out the possibility that APTs may be regulated themselves by posttranslational modifications, including *S*-palmitoylation. For example, Cys2 of APTs have been reported to be palmitoylated.[60] This modification likely enhances localization to the periphery of the membrane compartments to engage different substrates. If so, it would be interesting to study which zDHHCs catalyze APT *S*-palmitoylation and test if same zDHHCs process both APT1 and APT2. If different zDHHCs catalyze *S*-acylation on APT1 and APT2, it might suggest different lengths of acyl modifications, which might alter subcellular distribution and function. Also, one could address why only a fraction of APTs are *S*-palmitoylated. This N-terminally proximal *S*-palmitoylation is not critical for the catalytic activity, but may impart select localization that mediates responses to signaling events or potentially differentiates substrates. For instance, a number of studies suggest an increased level of depalmitoylation upon extracellular signaling activity.[25, 48, 76] Although it is possible that this could be due to conformational change in the substrate (exposing thioester), such complexity is unlikely to rise if APTs were not regulated.

To test this hypothesis, we could develop selective activity-based probes of APT1 and APT2. This approach maybe analogous to the proposed photo-crosslinking experiments, but it would enable precise localization studies. Through ML349 profiling experiment, I showed that isoform-selective APT inhibitors can be functionalized and optimized. Therefore, further development of functional and selective chemical probes of both APTs may help interrogate biological functions. This would enable the capture of APTs *in situ* upon various signaling changes as studies have suggested. For instance, one study saw APT activity increase upon EGF stimulation with the activity-based fluorescence probe.[102] While this probe is useful to capture the live cell images, it is still promiscuous, especially with a fractional sensitivity to APT knockdowns. The next generation of probe could include a reactive carbamate group or triazole urea and with a clickable handle on the other end (methoxy group for ML349 and furanyl group for ML348) to be conjugated with a fluorescent moiety. The design of the probe could be structure guided, mimicking ML348/349 in order to increase the selectivity. If such probe could be made, it may answer the remaining questions such as where are the APTs activated? Are they constitutively active? How is APT1 transported to mitochondria?

Altogether, these probes could dissect the differential function of APTs through visualizing spatiotemporal localization of active APTs, which would also significantly corroborate protein-protein interaction study described above.

Overall, any future studies of APTs should be directed towards investigating the cellular function of these enzymes. Clearly APTs have some functional effect in signaling pathway models (EGFR, Scrib etc.). The biochemical analysis is limited due to redundant functions of multiple serine hydrolases and it may be very time consuming to develop a probe that are only selective for the APTs. To get a big picture of the role of these enzymes, one could study protein-protein interaction experiments to characterize which proteins have affinity for APTs upon perturbations. This approach could potentially layout a cellular map of how these enzymes are able to respond to various cellular signaling events, if any, and the regulatory mechanism for their functional orthogonality.

Future directions towards understanding dynamic *S*-palmitoylation

In Chapter 4, I present a temporal pulse labeling strategy to reveal proteins with various rates of acylation. This data suggests some proteins are more efficiently *S*-palmitoylated than others, presumably since they are better substrates for select zDHHC enzymes. Both acyl-RAC and 17-ODYA profiling have not yielded conclusive profiles of select zDHHC substrates, perhaps due to compensatory activity of other closely related DHHCs. Many reports identify 2 or more zDHHCs as candidate acyltransferases for a protein of interest.[6, 142] Therefore, in single zDHHC knockout studies, temporal pulse labeling may overcome compensatory effects from other zDHHC enzymes, providing a kinetic approach to map select substrates. One caveat remains that DHHCs have different acyl chain length preferences[4], which could bias the overall results. To overcome this, one would repeat the experiments with varying chain lengths of the alkynyl fatty acids.

Alternatively, one could adapt strategies like bump-hole pairs to design a probe unique to an engineered zDHHC of interest.[166] Then the probe would be incorporated into various substrates or interaction partners, which can be enriched and identified. This engineering process could be guided by the crystal structures of DHHCs as recent

crystal structure of zDHHC20 and zDHHC15 revealed determinant of acyl-chain length selectivity.[166] Collectively, a future study could incorporate acyl-CoA probe with a photo-crosslinking moiety that would selectively fit in the engineered zDHHC to profile and enrich novel interacting partners in an analogous fashion to the temporal pulse labeling strategy (**Figure 5.2**). For instance, bulky residues lining the acyl-channel such as W158, F174, or F220 in zDHHC20 could be replaced by alanine or glycine to accommodate diazirine moiety. One potential pitfall of this approach is that the designed probe could still be promiscuous. To increase selectivity, non-conserved residues could be mutated and the probe could include bulkier functional handles such as cyclooctyne derivatives or other polar handles to promote unique interaction with the soluble domain of the zDHHC. Any optimization would require an *in vitro* assay for zDHHC acyl transferase activity. This may include competitive enzymatic assay with a native substrate, palmitoyl-CoA, followed by a conjugation with a fluorescent dye upon denaturation of the enzyme. Overall, this strategy would not only identify substrates of zDHHCs but also reveal the molecular network of enzyme-substrate interactions.

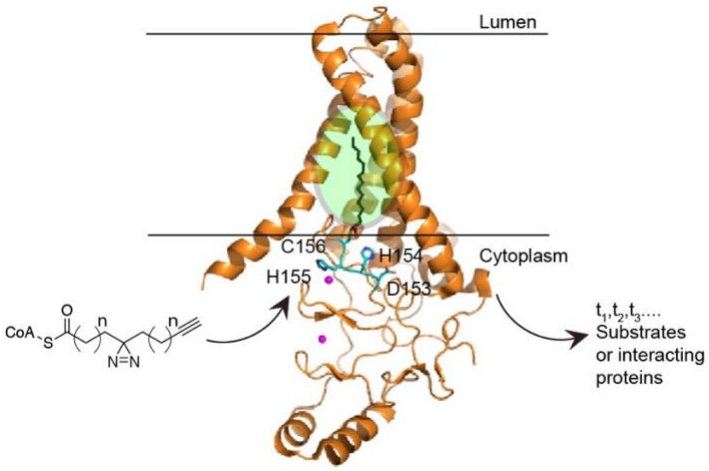

Figure 5.2 Schematic of temporal pulse labeling to profile substrates of zDHHCs

Crystal structure of hDHHC20. The catalytic residues are highlighted in cyan and 2-bromopalmitate (black) is covalently linked to catalytic Cys156 to mimic palmitate binding. The structural zinc molecules are shown as pink spheres. Green circle indicates potential sites of mutagenesis to uniquely fit engineered Acyl-CoA probe with a photo-crosslinking potential. Adapted from PDB:6BML

In the current study, we did not address which enzymes are responsible for the significant boost in *S*-acylation levels in the HDFP treated cells. The most likely candidates are ABHD17 enzymes since they are highly potent targets of HDFP and

multiple inhibition of other serine hydrolases did not reproduce HDFP-dependent results. However, since there are no selective inhibitors of ABHD17s we could not test this hypothesis. ABHD17s are worth deeper investigation, because they are more likely to be the major depalmitoylases than APTs for two major reasons. First, unlike APTs, these are known to be predominantly plasma membrane associated just like the majority of palmitoylated substrates. Second, genetic knockout of these enzymes has been reported to reduce the viability of cancer cells, indicating that they are likely to participate in regulation of key pathways for survival. Since these enzymes are reported to be Ras depalmitoylases, developing selective inhibitors would be therapeutically valuable in addition to studying the overall function.

However, any effort to develop ABHD17 inhibitors will be hampered in the absence of any structure. Thus, to gain deeper mechanistic understanding of these enzymes, a future study could solve crystal structures of ABHD17s bound to HDFP. Not only would these structures highlight acyl-binding channel but also residues or motifs critical for the activity. Since ABHD17 enzymes harbor multiple S-palmitoylation sites in their N-terminal domain, they are challenging to express in bacterial recombinant expression systems. In order to purify fully S-palmitoylated enzyme, it might be better to optimize expression in the eukaryotic cell lines with detergents. Nonetheless, it is unclear whether the palmitoylated N-terminus region is critical for the overall function of the enzyme. One could validate this by purifying the truncated versions or alanine mutants within the cysteine-rich domain. Meanwhile, activity-based high-throughput screening assays against a library of compounds would enable search for the lead inhibitors. Altogether, studying molecular details of ABHD17s would provide direct evidence for the substrate preferences as well as an opportunity to chemically modulate the activity of the enzyme.

To unravel global contribution of ABHD17s as depalmitoylases, a future study might use an inducible knock-down system to target ABHD17s, followed by temporal metabolic pulse profiling with 17-ODYA. However, one issue of temporal profiling analysis is that the method heavily relies on isobaric tag labeling and lacks biological replicates of samples. Therefore, a significant number of kinetic profiles are prone to human errors and instrumental errors due to increased complexity. To overcome these,

a future study should validate kinetic profiles of interest with [^{3}H]-palmitate temporal pulse labeling. If ABHD17 knock-down experiment mimics the results from the HDFP treated cells, it is a possibility that these enzymes could be regulating acyl-CoA levels in cells, thus globally contributing to the overall *S*-acylation status. To test this hypothesis, a future study could purify ABHD17s and carry out an *in vitro* enzymatic assay with palmitoyl-CoA. This study could build up to a metabolomics experiment, where we test the global level of palmitoyl-CoA upon knock-down of ABHD17s over a time course. Furthermore, it would be worthy to identify DHHC enzymes that palmitoylate ABHD17s. It may identify potential regulatory or trafficking mechanism of these major depalmitoylating enzymes, completing an overall picture of how cells establish dynamic *S*-acylation and *S*-deacylation cycle.

Ultimately, what fraction of proteins in the palmitoylome are actually palmitoylated at a given time? If there are multiple palmitoylation in a single protein, are they all dynamically regulated? If these questions can be addressed, it would provide the most detailed global map of regulatory dynamic *S*-palmitoylation. Any future study should focus on profiling the exact sites of *S*-palmitoylation. However, the reported sites of labeling methods rely on acyl-RAC, where cleaved thioesters are captured on bead and eluted from the beads after washing out the majority tryptic peptides. This method may lead to a significant number of false positives and any dynamic changes could be hindered by abundant steady state pool of palmitoylated sites. To overcome these difficulties, one could first label cells with 17-ODYA, then click with azido-diazo-biotin to enrich proteins with 17-ODYA incorporation. The captured peptides would be eluted by cleavage of the diazo moiety[33], leaving unique signatures on the captured peptides, which would represent the dynamic sites of palmitoylation. However, there would be a lot of steps involved in the procedure and the recovery or the coverage in the proteome could be very poor. Ultimately, it would be beneficial to develop liquid chromatography and mass spectrometry techniques to directly detect palmitoylation. The challenge here is that most of the hydrophobic peptides are lost during the sample purification procedure and the standard columns coupled to mass spectrometer are not optimized for the separation of hydrophobic moieties. Furthermore, since palmitoylation represents only minor fraction of proteome, in-depth software analyses are needed to precisely

quantify modifications. If these difficulties can be overcome, this approach would directly bypass chemical labeling procedures, which could potentially perturb native biological environment, as well as any loss of proteins during long procedures of sample preparation. Our lab is currently developing this technique and it would be beneficial to the field.

Overall, temporal pulse labeling revealed dynamic acylation rate of various proteins. The acylation rate is amplified following thioesterase inhibition, and highlights proteins with accelerated dynamics. This pulse-labeling approach has potential for direct analysis of acylation kinetic profiles following selective knockout or through incorporation of unique acyl-CoA derivatives. These approaches overcome inherent limitations in previous methods to identify the most likely physiological substrates. Similarly, gaining mechanistic insight of ABHD17s and their substrate profiles would provide a detailed molecular map of how cells modulate *S*-palmitoylation to regulate essential biological processes. Collectively, proposed future studies here will establish the most quantitative profiles of dynamic *S*-palmitoylation and identify potential therapeutic targets implicated in disease models.

Appendices

Appendix A: Synthesis and Purification Procedure of Chemicals Presented in Chapter 2

General chemical synthesis and purification procedure.

Compounds were purified by normal phase silica-gel flash column chromatography or Waters High Performance Liquid Chromatography system using a 1525 Binary Pump coupled to an Atlantis T13 C18 column and 2988 Photodiode Array detector. NMR spectra were acquired on a Varian 400 MHz instrument and processed using Mestrenova software. High-resolution mass spectrometry (HRMS) analysis was performed using Agilent Q-TOF mass spectrometer. Synthetic schemes are shown in **Figure A.1** and **A.2**.

Synthesis of ML348. *N*-(2-chloro-5-(trifluoromethyl)phenyl)-2-(4-(furan-2-carbonyl)piperazin-1-yl)acetamide. Synthesized as described previously[83]. 250 mg, 86% yield. ^{1}H NMR (400 MHz, Chloroform-*d*) δ 9.99 (s, 1H), 8.75 (s, 1H), 7.42 (t, *J* = 4.2 Hz, 2H), 7.21 (d, *J* = 8.2 Hz, 1H), 6.94 (d, *J* = 3.5 Hz, 1H), 6.41 (dd, *J* = 3.5, 1.8 Hz, 1H), 3.84 (s, 4H), 3.19 (s, 2H), 2.66 (s, 4H). HRMS (ESI positive): Calculated m/z $[M+H]^+$ = 416.0983, observed m/z $[M+H]^+$= 416.0989

Synthesis of ML349, ML349-sulfoxide, ML349-thioether.

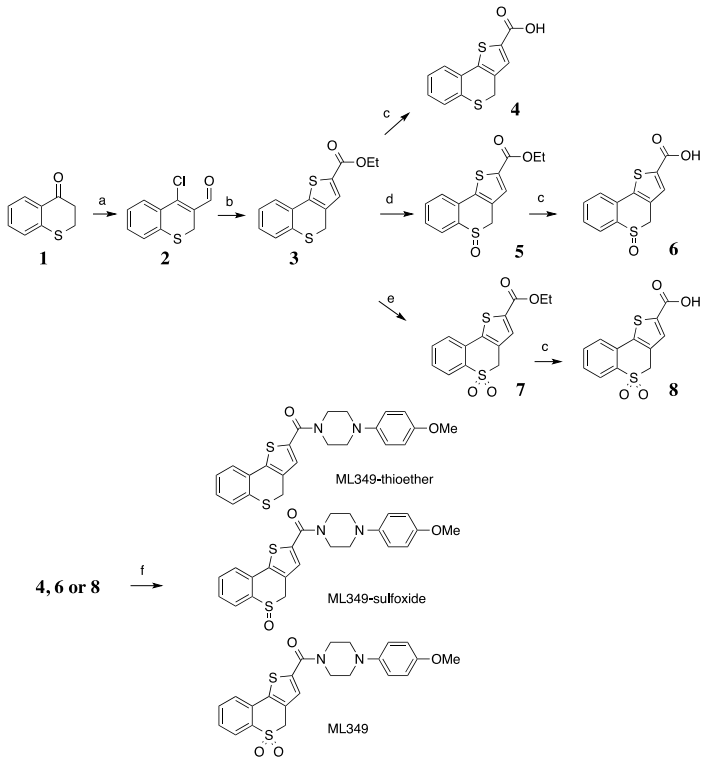

Figure A.1 General synthetic scheme of ML349 derivatives

Synthesized as described previously with modifications[83, 167]. (a) Phosphorous oxychloride ($POCl_3$), dimethylformide (DMF), 30 min 5 °C then 2 hours at 80 °C, sodium acetate. (b) sodium ethanolate, ethanol, 0 °C then room temperature 16 hours. (c) Sodium hydroxide, methanol, 60 °C, 16 hours. (d) *m*-CPBA, dichloromethane (DCM), room temperature, 3 hours. (e) peracetic acid, 1 hour. (f) 1-(4-methoxyphenyl)piperazine, HBTU, DIPEA, DCM, 16 hours, room temperature.

Synthesis of ML349-thioether. (4-(4-methoxyphenyl)piperazin-1-yl)(4*H*-thieno[3,2-*c*]thiochromen-2-yl)methanone. $POCl_3$ (0.8 mL, 1.14 eq.) was added drop-wise to ice-cold anhydrous DMF (5 mL), followed by drop-wise addition of **1** (0.8 mL, 1 eq.). The reaction mixture was stirred for 30 minutes on ice, heated to 80 °C for 2 hours, and quenched with 3 mL of ice-cold aqueous sodium acetate (25%). The crude sample was extracted twice with diethyl ether, and the organic fractions were pooled, washed with brine, dried over sodium sulfate, and concentrated to yield compound **2** (brown oily liquid). This compound was slowly added to a mixture of ice-cold ethylthioglycolate (0.2 mL, 1 eq.), sodium ethoxide (1.5 mL, 2 eq.) and anhydrous ethanol. The reaction mixture was stirred for 16 hours at room temperature and then heated to 80 °C for 2 hours. The crude sample was extracted with ethyl acetate several times, washed with brine, and dried over sodium sulfate. The crude mixture was purified by flash column chromatography (20% ethyl acetate : 80% hexanes), yielding compound **3** (300 mg,

54% yield). Next, compound **3** (92 mg, 1 eq.) was saponified with sodium hydroxide (24 mg, 2 eq.) in methanol overnight at 60 °C. After removing the solvent with a rotary evaporator, the concentrate was extracted with ethyl acetate to remove any starting material. 6 N HCl was then added to the aqueous mixture, precipitating a white solid. The solid was extracted with ethyl acetate, washed with brine, dried under sodium sulfate, and concentrated using a rotary evaporator to yield compound **4** (60 mg, 81% yield). Compound **4** (20 mg, 1 eq.) was mixed with HBTU (100 mg, 3 eq.), DIPEA (0.03 mL, 2 eq.), 1-(4-methoxyphenyl)piperazine (Sigma, 14 mg, 1 eq.) in DCM for 16 hours at room temperature. The solvent was evaporated and the crude mixture was extracted with dichloromethane (DCM). The organic portion was pooled, washed with brine and dried under sodium sulfate. The sample was purified using flash column chromatography (5% methanol: 95% DCM) to yield ML349-thioether (25 mg, 69% yield). ^{1}H NMR (401 MHz, Chloroform-d) δ 7.46 – 7.41 (m, 1H), 7.35 – 7.32 (m, 1H), 7.17 – 7.13 (m, 2H), 7.11 (s, 1H), 6.94 (d, J = 8.6 Hz, 2H), 6.87 – 6.82 (m, 2H), 3.93 (d, J = 9.6 Hz, 6H), 3.76 (s, 3H), 3.12 (t, J = 5.0 Hz, 4H). HRMS (ESI positive): Calculated m/z $[M+H]^+$ 423.1195, observed m/z $[M+H]^+$= 423.1194

Synthesis of ML349-sulfoxide. (4-(4-methoxyphenyl)piperazin-1-yl)(5-oxido-4*H*-thieno[3,2-*c*]thiochromen-2-yl)methanone. Compound **3** (90 mg, 1 eq.) from ML349-thioether synthesis was treated with *m*-CPBA (1 eq. 78 mg) in 20 mL of DCM and stirred for 3 hours at room temperature. The reaction mixture was extracted with DCM, the organic layer was pooled, treated with similar procedures as above, and purified by flash column chromatography (5% methanol: 95 % DCM) to yield compound **5** (105 mg, 80% yield). This compound was saponified to yield compound **6** (20 mg, 23% yield) and coupled with 1-(4-methoxyphenyl)piperazine as described above to yield ML349-sulfoxide (11 mg, 37% yield). ^{1}H NMR (400 MHz, Chloroform-*d*) δ 7.45 – 7.24 (m, 4H), 7.18 – 7.07 (m, 1H), 6.95 – 6.78 (m, 4H), 3.90 (d, *J* = 6.2 Hz, 3H), 3.73 (s, 4H), 3.53 (s, 2H), 3.09 (t, *J* = 5.1 Hz, 4H). HRMS (ESI positive): Calculated m/z $[M+H]^+$ = 438.1072, observed m/z $[M+H]^+$= 438.1010.

Synthesis of ML349. (5,5-dioxido-4*H*-thieno[3,2-*c*]thiochromen-2-yl)(4-(4-methoxyphenyl)piperazin-1-yl)methanone. Compound **3** (90 mg, 1 eq.) from ML349-thioether synthesis was treated with peracetic acid (0.7 mL, 1 eq.) in 10 mL of DCM for

1 hour at room temperature. The reaction mixture was quenched with dimethyl sulfide in drop-wise fashion. The crude mixture was extracted with DCM. The organic portion was pooled and purified using flash column chromatography (5% methanol: 95% DCM) to yield compound **7** (70 mg, 70% yield). This compound was saponified to yield compound **8** (27 mg, 42% yield) and coupled with 1-(4-methoxyphenyl)piperazine as described above to yield the final product, ML349 (28 mg, 68% yield). ^{1}H NMR (400 MHz, Chloroform-*d*) δ 8.03 – 7.99 (m, 1H), 7.62 (dtd, *J* = 15.4, 7.8, 1.4 Hz, 2H), 7.55 – 7.47 (m, 1H), 7.20 (s, 1H), 6.92 (d, *J* = 9.0 Hz, 2H), 6.87 – 6.81 (m, 2H), 4.42 (s, 2H), 3.91 (t, *J* = 5.1 Hz, 3H), 3.11 (t, *J* = 5.1 Hz, 8H). ^{13}C NMR (100 MHz, $CDCl_3$) δ 162.11, 154.66, 137.27, 136.19, 133.93, 133.55, 130.02, 129.86, 129.23, 127.85, 125.82, 124.20, 119.09, 114.56, 55.54, 51.27, 51.15. HRMS (ESI positive): Calculated m/z $[M+H]^+$ = 455.1094, observed m/z $[M+H]^+$= 455.1097.

Synthesis of ML349-FL. 4-((2-(2-(2-(2-(2-(4-((4-(4-(5,5-dioxido-4*H*-thieno[3,2-*c*]thiochromene-2-carbonyl)piperazin-1-yl)phenoxy)methyl)-1*H*-1,2,3-triazol-1-yl)ethoxy)ethoxy)ethoxy)ethyl)carbamoyl)-2-(6-hydroxy-3-oxo-9,9a-dihydro-3*H*-xanthen-9-yl)benzoic acid. Compound **9** (900 mg, 1 eq) was treated with di-tert-butyl dicarbamate (1.1 mL, 1 eq.) in methanol for 12 hours. The contents were extracted with ethyl acetate, washed with brine, and dried over sodium sulfate. The samples were concentrated under vacuum to yield compound **10** (1.3 g, 95% yield). Compound **10** (250 mg, 1eq.) was treated with propargyl bromide (0.2 mL, 2 eq.) and potassium carbonate (300 mg, 2 eq.) in dimethylformamide (DMF). The mixture was stirred for 16 hours at room temperature. The crude mixture was extracted with ethyl acetate several times before washing with brine and drying over sodium sulfate. The sample was further purified by flash column chromatography (1:1 ethyl acetate/hexanes) to yield compound **11** (250 mg, 88% yield). Compound **11** (250 mg, 1 eq.) was treated with trifluoroacetic acid (TFA, 2.5 eq.) in dichloromethane (DCM) for 5 hours at 60º C reflux. The residual TFA was boiled off and the sample was dried at high-vacuum and proceeded without further purification. The Boc-deprotected compound **11** was coupled with compound **8** (220 mg, 1 eq.) in the mixture of HBTU (910 mg, 3 eq.), DIPEA (0.1 mL, 2 eq.) in DCM for 16 hours. The crude reaction mixture was extracted with DCM several times and purified with flash column chromatography (3% methanol: 97% DCM to yield compound

12 (300 mg, 78% yield). This compound was conjugated with 11-azido-3,6,9-triozaunderdecan (Sigma, 0.013 mL, 1 eq.) in the presence of sodium ascorbate (3 mg, 0.2 eq.) and catalytic amount of $CuSO_4$ in DMSO for 16 hours. The crude mixture was subjected to HPLC to isolate compound **13** (100 mg, 22% yield). ^{1}H NMR (401 MHz, Methanol-d_4) δ 8.08 (s, 1H), 8.02 (d, *J* = 7.8 Hz, 1H), 7.80 – 7.74 (m, 2H), 7.63 (ddd, *J* = 8.3, 6.3, 2.4 Hz, 1H), 7.48 (s, 1H), 7.02 – 6.94 (m, 4H), 5.13 (s, 2H), 4.67 (d, *J* = 7.7 Hz, 2H), 4.61 (t, *J* = 5.0 Hz, 2H), 3.93 (dt, *J* = 13.3, 4.9 Hz, 6H), 3.68 – 3.56 (m, 12H), 3.16 (t, *J* = 5.2 Hz, 4H), 3.09 (t, *J* = 5.1 Hz, 2H). Compound **13** (20 mg, 1 eq.) was coupled with NHS-Fluorescein (Thermo) (13 mg, 1 eq.) in the mixture of DMSO and a few drops of DIPEA. The mixture was stirred for 3 hours and purified by HPLC to yield ML349-FL (10 mg, 31% yield). HRMS (ESI negative): Calculated m/z $[M-H]^-$ = 1053.3034, observed m/z $[M-H]^-$= 1053.2781

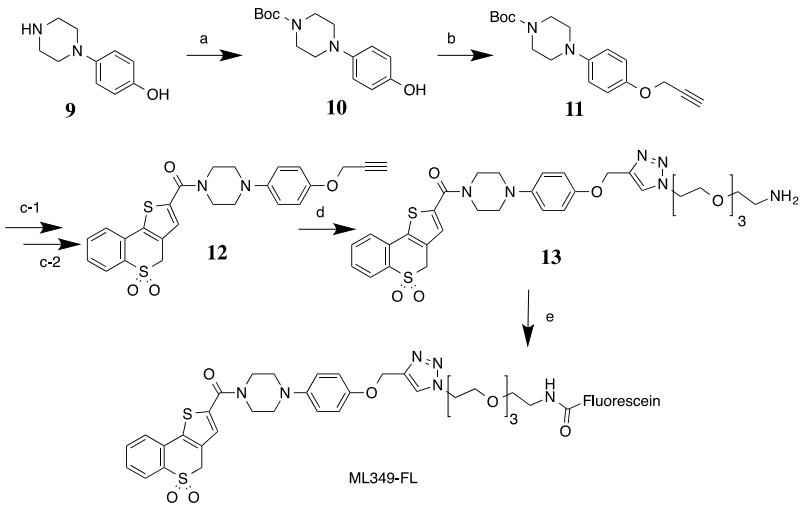

Figure A.2 Synthetic scheme of ML349-FL

(a) di-tert-butyl dicarbamate, methanol, 12 hours, room temperature. (b) propargyl bromide, potassium carbonate, DMF, 16 hours, room temperature. (c-1) TFA, DCM, 5 hours, 60 °C. (c-2) HBTU, DIPEA, DCM, 16 hours, room temperature. (d) 11-azido-3,6,9-triozaunderdecan, sodium ascorbate, $CuSO_4$, DMSO, 16 hours, room temperature. (e) NHS-Fluorescein, DMSO, DIPEA, room temperature, 3 hours.

Appendix B: Synthesis and Purification Procedure of Chemicals Presented in Chapter 3

General chemical synthesis and purification procedures. All compounds were purchased from Sigma-Aldrich, unless otherwise noted and were of the highest purity available. NMR analysis was performed using a Varian 400 MHz NMR instrument. NMR integrations and coupling constants were computed using MestreNova. Small molecule high-resolution mass spectrometry was performed using an electrospray Agilent Q-TOF mass spectrometer (accuracy 1-5 ppm) and analyzed using the Agilent MassHunter software suite. Low-resolution mass spectrometry was performed using an electrospray Micromass LCT time-of-flight mass coupled to a HPLC pump with a rheodyne loop injector. Compounds were purified by normal phase flash silica-gel column chromatography or by semi-prep High-Performance Column Chromatography (HPLC). HPLC purifications were performed using a Waters semi-preparative 1525 binary pump system coupled to a photodiode array detector, an autosampler, and an automatic fraction collector. Separations were carried out on using the Waters Atlantis prep T3 C18 column (10 x 250 mm), in 95/5 water/acetonitrile 0.1% formic acid for 2 minutes, followed by a 40 min gradient increasing the mobile phase to 5/95 water/acetonitrile with 0.1% formic acid. Data were analyzed using the Waters Empower software. Resulting HPLC fractions were lyophilized using a Labconco FreeZone2.5-Plus freeze-drying system. In-gel fluorescence was imaged using the GE Typhoon scanner. General synthetic scheme is shown in **Figure B.1.**

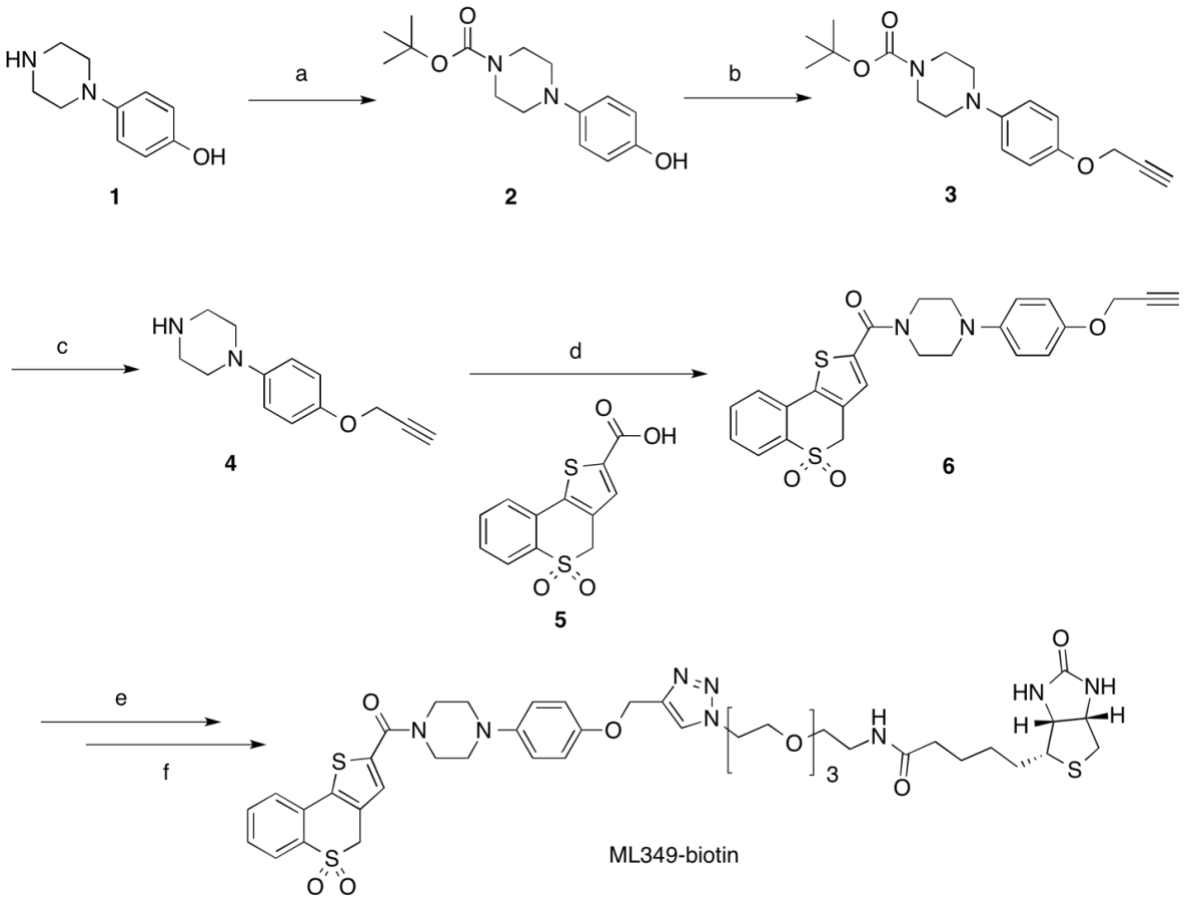

Figure B.1 ML349-Biotin synthesis scheme

(a) Di-*tert*-butyl dicarbonate, methanol, 12 hours, room temperature. 90-95% yield. (b) propargyl bromide, potassium carbonate, DMF, 16 hours, room temperature. 80-92% yield. (c) TFA, DCM, 5 hours, 60 °C. 60-90% yield. (d) Compound 5, HBTU, DIPEA, DCM, 16 hours, room temperature. 40-54% yield. (e) 11-Azido-3,6,9-trioxaunderdecan-1-amine, sodium ascorbate, $CuSO_4$, DMSO, 16 hours, room temperature. (f) NHS-Biotin, DMSO, DIPEA, room temperature, 3 hours. 52%- 60% yield.

Synthesis of ML349-biotin. N-(2-(2-(2-(2-(4-((4-(4-(5,5-dioxido-4H-thieno[3,2-c]thiochromene-2-carbonyl)piperazin-1-yl)phenoxy)methyl)-1H-1,2,3-triazol-1-yl)ethoxy)ethoxy)ethoxy)ethyl)-5-(2-oxohexahydro-1H-thieno[3,4-d]imidazol-4-yl)pentanamide. Compound 1 (Sigma, 900 mg, 1 eq) was treated with di-*tert*-butyl dicarbamate (1 eq.) in methanol for 12 hours. The contents were extracted with ethyl acetate, washed with brine, and then dried over sodium sulfate. The samples were concentrated under vacuum to yield compound 2, *tert*-butyl 4-(4-hydroxyphenyl)piperazine-1-carboxylate (1.3 g, 95 % yield) . ^{1}H NMR (400 MHz, $CDCl_3$) δ 6.82 (ddd, *J* = 36.0, 9.8, 3.0 Hz, 4H), 3.74 – 3.48 (m, 4H), 3.07 – 2.95 (m, 4H), 1.48 (s, 9H). ^{13}C NMR (100 MHz, $CDCl_3$) δ 155.0, 151.0, 119.4, 116.1, 80.3, 77.5, 77.2, 76.9, 51.4, 28.6. Compound 2 (125 mg) was treated with propargyl bromide (2 eq.) and

potassium carbonate (2 eq.) in dimethylformamide (DMF). The mixture was stirred for 16 hours at room temperature. The crude mixture was extracted with ethyl acetate several times before washing with brine and drying over sodium sulfate. The sample was further purified by flash column chromatography (1:1 ethyl acetate/hexanes) to yield compound 3, *tert*-butyl 4-(4-(prop-2-yn-1-yloxy)phenyl)piperazine-1-carboxylate (130 mg, 92 % yield) ^{1}H NMR (400 MHz, $CDCl_3$) δ 6.83 – 6.73 (m, 4H), 4.50 (d, *J* = 2.5 Hz, 2H), 3.50 – 3.42 (m, 4H), 2.93 – 2.85 (m, 4H), 2.47 (t, *J* = 2.4 Hz, 1H), 1.39 (s, 9H). ^{13}C NMR (100 MHz, $CDCl_3$) δ 154.2, 151.7, 146.0, 118.2, 115.4, 79.3, 56.0, 50.2, 28.1. The compound 3 (1 eq.) was treated with trifluoroacetic acid (TFA, 2.5 eq.) in dichloromethane (DCM) for 5 hours at 60 ºC reflux. The residual TFA was boiled off and the sample was dried at high-vacuum to yield compound 4 (87 mg, 90 % yield) and continued without further purification. Synthesis of compound 5 was previously described[103], and an aliquot of the characterized product was used here. Compound 4 (50 mg, 1 eq.) was coupled with compound 5 (1 eq.) by using HBTU (Sigma, 3 eq.), DIPEA (Sigma, 2 eq.), and DMF as solvent. The reaction mixture was stirred for 16 hours at room temperature and the crude mixture was extracted with DCM several times, followed by a brine wash and sodium sulfate treatment to remove excess polar materials. The sample was further purified by flash column chromatography (40 % ethyl acetate: 60 % hexanes) to yield compound 6, (5,5-dioxido-4*H*-thieno[3,2-*c*]thiochromen-2-yl)(4-(4-(prop-2-yn-1-yloxy)phenyl)piperazin-1-yl)methanone (46 mg, 54 % yield) ^{1}H NMR (400 MHz, $CDCl_3$) δ 8.05 (d, *J* = 7.8 Hz, 1H), 7.72 – 7.49 (m, 3H), 7.23 (s, 1H), 6.97 (t, *J* = 10.9 Hz, 4H), 4.66 (d, *J* = 2.4 Hz, 2H), 4.45 (s, 2H), 3.99 (s, 4H), 3.19 (s, 4H), 2.52 (t, *J* = 2.4 Hz, 1H). ^{13}C NMR (100 MHz, $CDCl_3$) δ 162.2, 134.0, 133.6, 130.0, 129.3, 127.9, 125.8, 124.2, 115.9, 56.3, 51.2. The alkynyl portion of compound 6 (30 mg, 1 eq.) was conjugated with 11-Azido-3,6,9-trioxaundecan-1-amine (Sigma, 1 eq.) via Copper(I)-Catalyzed Azide-Alkyne Cycloaddition (CuAAC) with $CuSO_4$ (catalytic amount) and sodium ascorbate (0.2 eq.) in DMSO for 16 hours at 50 °C. The crude mixture was purified by HPLC and then lyophilized to yield the intermediate product with free amine at the end of the linker, (4-(4-((1-(2-(2-(2-(2-aminoethoxy)ethoxy)ethoxy)ethyl)-1*H*-1,2,3-triazol-4-yl)methoxy)phenyl)piperazin-1-yl)(5,5-dioxido-4*H*-thieno[3,2-*c*]thiochromen-2-yl)methanone, (31 mg, 70% yield) ^{1}H

NMR (401 MHz, Methanol-d_4) δ 8.08 (s, 1H), 8.01 (d, *J* = 7.8 Hz, 1H), 7.80 – 7.73 (m, 2H), 7.62 (ddd, *J* = 8.3, 6.3, 2.4 Hz, 1H), 7.47 (s, 1H), 7.04 – 6.92 (m, 4H), 5.12 (s, 2H), 4.67 (d, *J* = 7.7 Hz, 2H), 4.60 (t, *J* = 5.0 Hz, 2H), 3.92 (dt, *J* = 13.3, 4.9 Hz, 5H), 3.71 – 3.54 (m, 11H), 3.12 (dt, *J* = 24.8, 5.1 Hz, 6H). This product was treated with Biotin-NHS ester (15 mg, Click Chemistry Tools), DIPEA (2 eq.) in DMSO for 16 hours at room temperature. The resulting crude mixture was purified by HPLC to yield ML349-biotin (22 mg, 52 % yield).

Final Product (**Figure B.2**): ^{1}H NMR (400 MHz, Chloroform-d) δ 8.02 (d, *J* = 7.8 Hz, 1H), 7.85 (s, 1H), 7.64 (dt, *J* = 15.7, 7.6 Hz, 2H), 7.53 (t, *J* = 7.5 Hz, 1H), 7.28 (s, 1H), 6.94 (s, 4H), 5.14 (s, 2H), 4.54 (t, *J* = 4.9 Hz, 2H), 4.47 (s, 2H), 4.26 (d, *J* = 6.1 Hz, 1H), 4.02 – 3.82 (m, 6H), 3.67 – 3.45 (m, 11H), 3.37 (q, *J* = 5.2 Hz, 2H), 3.12 (d, *J* = 20.1 Hz, 5H), 2.91 – 2.78 (m, 1H), 2.16 (t, *J* = 7.5 Hz, 2H), 1.58 (ddt, *J* = 31.9, 11.7, 6.5 Hz, 5H), 1.40 (dt, *J* = 15.0, 7.0 Hz, 2H). ^{13}C NMR (100 MHz, $CDCl_3$) δ 173.3, 164.1, 162.2, 136.3, 134.0, 133.6, 130.1, 130.1, 130.1, 129.3, 128.1, 125.9, 124.2, 115.7, 77.2, 70.5, 70.4, 70.1, 69.9, 69.4, 62.4, 61.8, 60.2, 55.6, 51.2, 50.4, 40.6, 39.1, 35.9, 28.3, 28.1, 25.6. $C_{43}H_{54}N_8O_9S_3$, HRMS (ESI positive), [M+H] predicted m/z: 923.3249, found 923.3232. HPLC purity: 99% (**Figure B.3**).

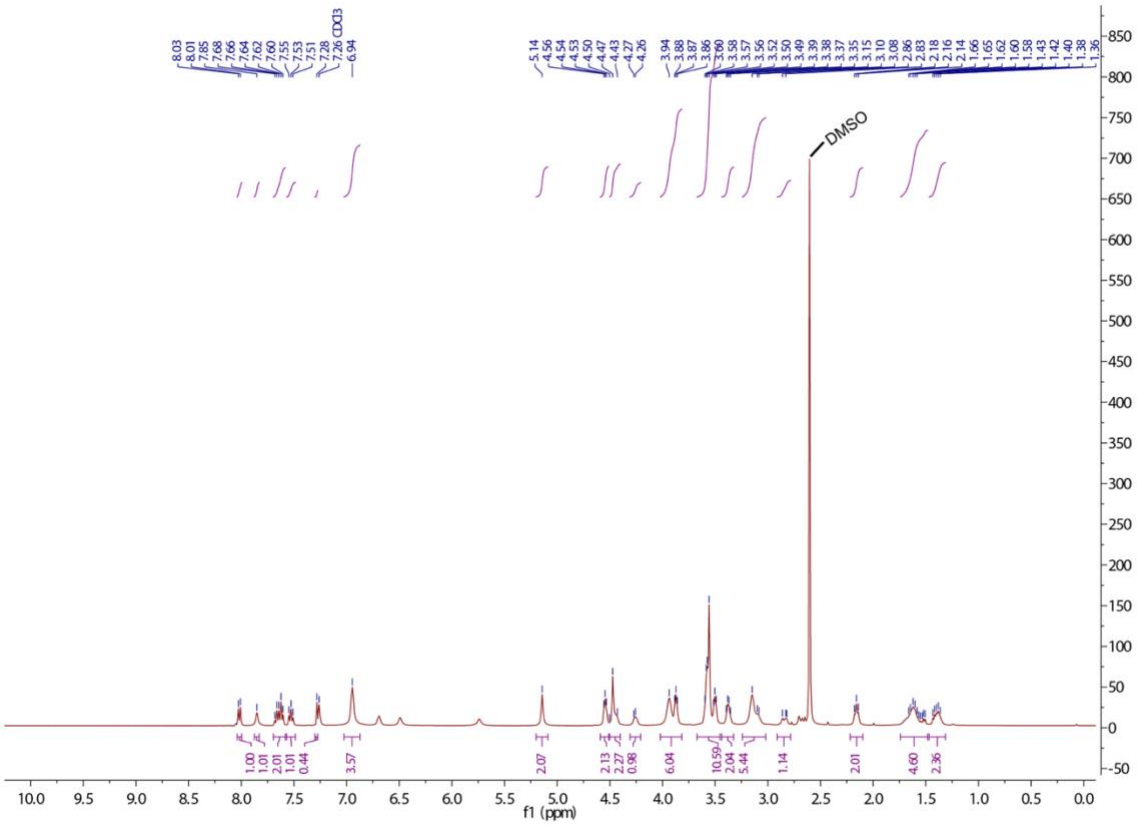

Figure B.2 ^{1}H NMR of Ml349-Biotin

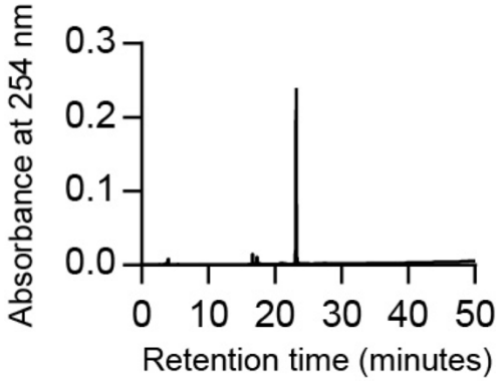

Figure B.3 HPLC analysis of ML349-Biotin

Synthesis of *ortho*-ML349-biotin. **N-(2-(2-(2-(2-(4-(2-(4-(5,5-dioxido-4H-thieno[3,2-c]thiochromene-2-carbonyl)piperazin-1-yl)phenoxy)-1H-1,2,3-triazol-1-yl)ethoxy)ethoxy)ethoxy)ethyl)-5-(2-oxohexahydro-1H-thieno[3,4-d]imidazol-4-yl)pentanamide**. Synthesized as described above but used 2-(piperazin-1-yl)phenol (50 mg) during step (a). Intermediate compound 2, *tert*-butyl 4-(2-hydroxyphenyl)piperazine-1-carboxylate, (60 mg, 90% yield) ^{1}H NMR (400 MHz, $CDCl_3$) δ 7.10 – 6.96 (m, 2H),

6.89 (dd, *J* = 8.0, 1.5 Hz, 1H), 6.78 (td, *J* = 7.6, 1.5 Hz, 1H), 3.52 (t, *J* = 5.0 Hz, 4H), 2.75 (t, *J* = 5.0 Hz, 4H), 1.45 (s, 9H). ^{13}C NMR (100 MHz, $CDCl_3$) δ 154.6, 151.2, 138.7, 126.3, 121.1, 120.0, 114.4, 79.8, 52.2, 44.3, 28.4. Intermediate compound 3, *tert*-butyl 4-(2-(prop-2-yn-1-yloxy)phenyl)piperazine-1-carboxylate, (20 mg, 60% yield) ^{1}H NMR (400 MHz, $CDCl_3$) δ 6.99 – 6.87 (m, 4H), 4.72 (d, *J* = 2.4 Hz, 2H), 3.57 (t, *J* = 5.0 Hz, 4H), 2.98 (t, *J* = 5.0 Hz, 4H), 2.50 (t, *J* = 2.4 Hz, 1H), 1.46 (s, 9H). Intermediate compound 6, (5,5-dioxido-4*H*-thieno[3,2-*c*]thiochromen-2-yl)(4-(2-(prop-2-yn-1-yloxy)phenyl)piperazin-1-yl)methanone,(13 mg, 40% yield)^{1}H NMR (400 MHz, $CDCl_3$) δ 8.04 (dt, *J* = 8.2, 2.4 Hz, 1H), 7.65 (dtd, *J* = 15.0, 7.8, 1.3 Hz, 2H), 7.54 (td, *J* = 7.6, 1.5 Hz, 1H), 7.23 (s, 1H), 7.15 – 6.97 (m, 4H), 4.79 (d, *J* = 2.4 Hz, 2H), 4.44 (d, *J* = 5.2 Hz, 2H), 4.14 – 3.91 (m, 4H), 3.25 (d, *J* = 23.1 Hz, 4H), 2.54 (t, *J* = 2.4 Hz, 1H). Intermediate compound before coupling with NHS-biotin, (4-(2-((1-(2-(2-(2-(2-aminoethoxy)ethoxy)ethoxy)ethyl)-1*H*-1,2,3-triazol-4-yl)methoxy)phenyl)piperazin-1-yl)(5,5-dioxido-4*H*-thieno[3,2-*c*]thiochromen-2-yl)methanone, (12 mg, 65% yield) ^{1}H NMR (400 MHz, Methanol-d_4) δ 8.03 (t, *J* = 8.0 Hz, 1H), 7.94 (s, 1H), 7.70 – 7.59 (m, 2H), 7.52 (t, *J* = 7.2 Hz, 1H), 7.31 (s, 1H), 7.09 – 6.88 (m, 4H), 5.26 (d, *J* = 3.7 Hz, 2H), 4.69 – 4.43 (m, 4H), 3.91 (p, *J* = 5.0 Hz, 6H), 3.79 – 3.46 (m, 9H), 3.37 (p, *J* = 5.1 Hz, 2H), 3.14 (d, *J* = 5.8 Hz, 5H).

Final product (Figure B.4): (9 mg, 60% yield). ^{1}H NMR (400 MHz, Chloroform-*d*) δ 8.18 – 7.98 (m, 2H), 7.85 (m, *J* = 20.2 Hz, 1H), 7.72 – 7.51 (m, 3H), 7.05 (m, *J* = 34.3 Hz, 4H), 5.28 (s, 2H), 4.67 – 4.21 (m, 6H), 3.93 (m, *J* = 36.5 Hz, 6H), 3.71 – 3.06 (m, 17H), 2.93 – 2.58 (m, 3H), 2.17 (s, 1H), 1.53 (d, *J* = 90.0 Hz, 6H). $C_{43}H_{54}N_8O_9S_3$, HRMS (ESI positive), [M+H] predicted m/z: 923.3249, found 923.3242. HPLC purity: 99% (**Figure B.5**).

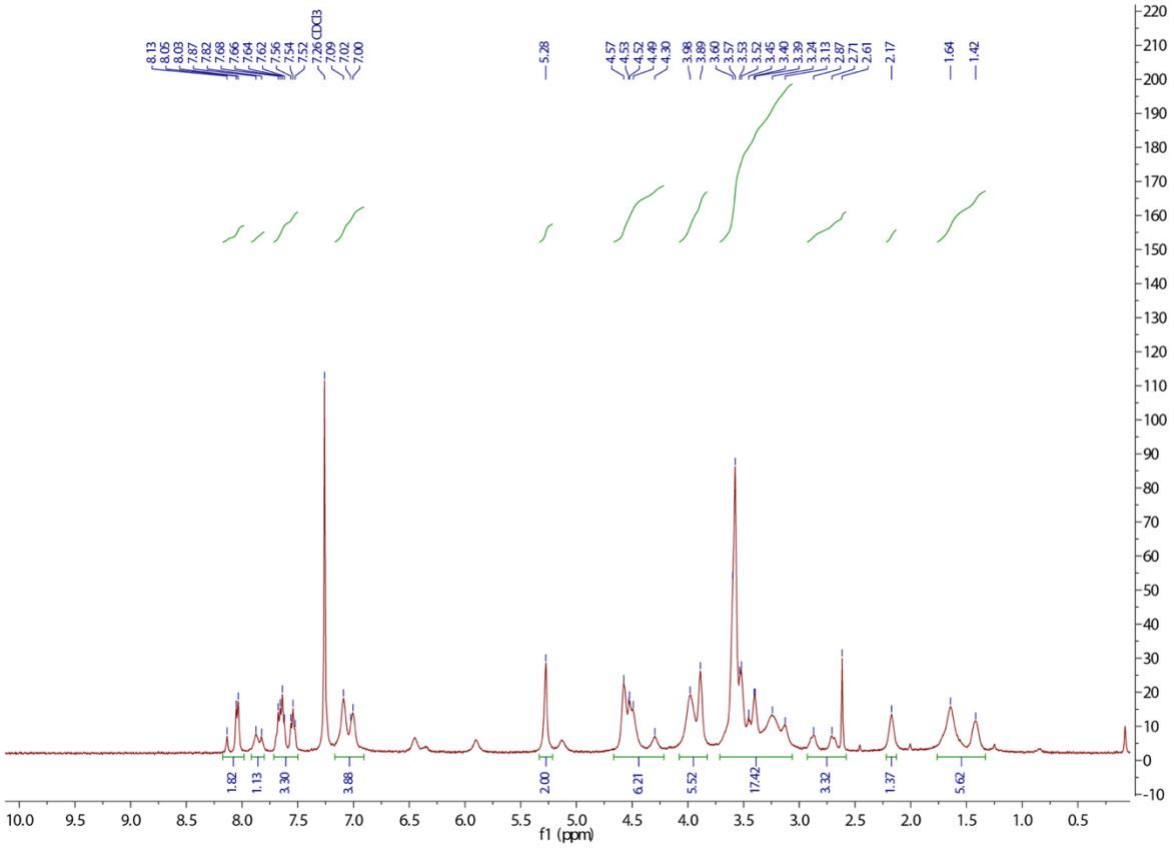

Figure B.4 ^{1}H NMR analysis of *ortho*-ML349-biotin

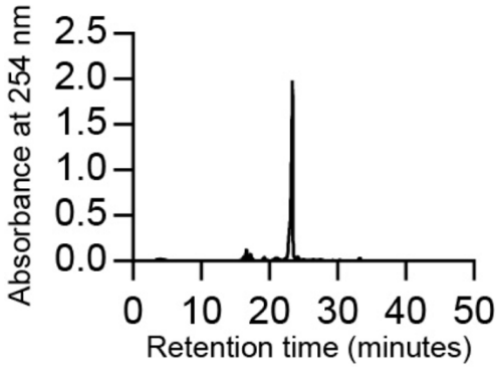

Figure B.5 HPLC analysis of *ortho*-ML349-biotin

References

1. Tom, C. T.; Martin, B. R., Fat chance! Getting a grip on a slippery modification. *ACS Chem Biol* **2013,** *8* (1), 46-57.
2. Liang, X.; Nazarian, A.; Erdjument-Bromage, H.; Bornmann, W.; Tempst, P.; Resh, M. D., Heterogeneous fatty acylation of Src family kinases with polyunsaturated fatty acids regulates raft localization and signal transduction. *J Biol Chem* **2001,** *276* (33), 30987-94.
3. Thinon, E.; Percher, A.; Hang, H. C., Bioorthogonal Chemical Reporters for Monitoring Unsaturated Fatty-Acylated Proteins. *Chembiochem* **2016,** *17* (19), 1800-1803.
4. Greaves, J.; Munro, K. R.; Davidson, S. C.; Riviere, M.; Wojno, J.; Smith, T. K.; Tomkinson, N. C.; Chamberlain, L. H., Molecular basis of fatty acid selectivity in the zDHHC family of S-acyltransferases revealed by click chemistry. *Proc Natl Acad Sci U S A* **2017,** *114* (8), E1365-E1374.
5. Lobo, S.; Greentree, W. K.; Linder, M. E.; Deschenes, R. J., Identification of a Ras palmitoyltransferase in Saccharomyces cerevisiae. *J Biol Chem* **2002,** *277* (43), 41268-73.
6. Fukata, M.; Fukata, Y.; Adesnik, H.; Nicoll, R. A.; Bredt, D. S., Identification of PSD-95 palmitoylating enzymes. *Neuron* **2004,** *44* (6), 987-96.
7. Gottlieb, C. D.; Zhang, S.; Linder, M. E., The Cysteine-rich Domain of the DHHC3 Palmitoyltransferase Is Palmitoylated and Contains Tightly Bound Zinc. *J Biol Chem* **2015,** *290* (49), 29259-69.
8. Li, Y.; Martin, B. R.; Cravatt, B. F.; Hofmann, S. L., DHHC5 protein palmitoylates flotillin-2 and is rapidly degraded on induction of neuronal differentiation in cultured cells. *J Biol Chem* **2012,** *287* (1), 523-30.
9. Thomas, G. M.; Hayashi, T.; Chiu, S. L.; Chen, C. M.; Huganir, R. L., Palmitoylation by DHHC5/8 targets GRIP1 to dendritic endosomes to regulate AMPA-R trafficking. *Neuron* **2012,** *73* (3), 482-96.
10. Brigidi, G. S.; Santyr, B.; Shimell, J.; Jovellar, B.; Bamji, S. X., Activity-regulated trafficking of the palmitoyl-acyl transferase DHHC5. *Nat Commun* **2015,** *6*, 8200.
11. Zeidman, R.; Buckland, G.; Cebecauer, M.; Eissmann, P.; Davis, D. M.; Magee, A. I., DHHC2 is a protein S-acyltransferase for Lck. *Mol Membr Biol* **2011,** *28* (7-8), 473-86.
12. Runkle, K. B.; Kharbanda, A.; Stypulkowski, E.; Cao, X. J.; Wang, W.; Garcia, B. A.; Witze, E. S., Inhibition of DHHC20-Mediated EGFR Palmitoylation Creates a Dependence on EGFR Signaling. *Mol Cell* **2016,** *62* (3), 385-96.
13. Chai, S.; Cambronne, X. A.; Eichhorn, S. W.; Goodman, R. H., MicroRNA-134 activity in somatostatin interneurons regulates H-Ras localization by repressing the palmitoylation enzyme, DHHC9. *Proc Natl Acad Sci U S A* **2013,** *110* (44), 17898-903.

14. Swarthout, J. T.; Lobo, S.; Farh, L.; Croke, M. R.; Greentree, W. K.; Deschenes, R. J.; Linder, M. E., DHHC9 and GCP16 constitute a human protein fatty acyltransferase with specificity for H- and N-Ras. *J Biol Chem* **2005,** *280* (35), 31141-8.
15. Raymond, F. L.; Tarpey, P. S.; Edkins, S.; Tofts, C.; O'Meara, S.; Teague, J.; Butler, A.; Stevens, C.; Barthorpe, S.; Buck, G.; Cole, J.; Dicks, E.; Gray, K.; Halliday, K.; Hills, K.; Hinton, J.; Jones, D.; Menzies, A.; Perry, J.; Raine, K.; Shepherd, R.; Small, A.; Varian, J.; Widaa, S.; Mallya, U.; Moon, J.; Luo, Y.; Shaw, M.; Boyle, J.; Kerr, B.; Turner, G.; Quarrell, O.; Cole, T.; Easton, D. F.; Wooster, R.; Bobrow, M.; Schwartz, C. E.; Gecz, J.; Stratton, M. R.; Futreal, P. A., Mutations in ZDHHC9, which encodes a palmitoyltransferase of NRAS and HRAS, cause X-linked mental retardation associated with a Marfanoid habitus. *Am J Hum Genet* **2007,** *80* (5), 982-7.
16. Lemonidis, K.; Werno, M. W.; Greaves, J.; Diez-Ardanuy, C.; Sanchez-Perez, M. C.; Salaun, C.; Thomson, D. M.; Chamberlain, L. H., The zDHHC family of S-acyltransferases. *Biochem Soc Trans* **2015,** *43* (2), 217-21.
17. Buss, J. E.; Sefton, B. M., Direct Identification of Palmitic Acid as the Lipid Attached to P21ras. *Molecular and Cellular Biology* **1986,** *6* (1), 116-122.
18. Hancock, J. F.; Magee, A. I.; Childs, J. E.; Marshall, C. J., All Ras Proteins Are Polyisoprenylated but Only Some Are Palmitoylated. *Cell* **1989,** *57* (7), 1167-1177.
19. Linder, M. E.; Middleton, P.; Hepler, J. R.; Taussig, R.; Gilman, A. G.; Mumby, S. M., Lipid modifications of G proteins: alpha subunits are palmitoylated. *Proc Natl Acad Sci U S A* **1993,** *90* (8), 3675-9.
20. Rocks, O.; Gerauer, M.; Vartak, N.; Koch, S.; Huang, Z. P.; Pechlivanis, M.; Kuhlmann, J.; Brunsveld, L.; Chandra, A.; Ellinger, B.; Waldmann, H.; Bastiaens, P. I., The palmitoylation machinery is a spatially organizing system for peripheral membrane proteins. *Cell* **2010,** *141* (3), 458-71.
21. Rocks, O.; Peyker, A.; Kahms, M.; Verveer, P. J.; Koerner, C.; Lumbierres, M.; Kuhlmann, J.; Waldmann, H.; Wittinghofer, A.; Bastiaens, P. I., An acylation cycle regulates localization and activity of palmitoylated Ras isoforms. *Science* **2005,** *307* (5716), 1746-52.
22. Webb, Y.; Hermida-Matsumoto, L.; Resh, M. D., Inhibition of protein palmitoylation, raft localization, and T cell signaling by 2-bromopalmitate and polyunsaturated fatty acids. *J Biol Chem* **2000,** *275* (1), 261-70.
23. Martin, B. R.; Lambert, N. A., Activated G Protein Galphas Samples Multiple Endomembrane Compartments. *J Biol Chem* **2016,** *291* (39), 20295-20302.
24. Mumby, S. M.; Kleuss, C.; Gilman, A. G., Receptor regulation of G-protein palmitoylation. *Proc Natl Acad Sci U S A* **1994,** *91* (7), 2800-4.
25. Wedegaertner, P. B.; Bourne, H. R., Activation and depalmitoylation of Gs alpha. *Cell* **1994,** *77* (7), 1063-70.
26. Willumsen, B. M.; Cox, A. D.; Solski, P. A.; Der, C. J.; Buss, J. E., Novel determinants of H-Ras plasma membrane localization and transformation. *Oncogene* **1996,** *13* (9), 1901-9.
27. James, G.; Olson, E. N., Identification of a novel fatty acylated protein that partitions between the plasma membrane and cytosol and is deacylated in response to serum and growth factor stimulation. *J Biol Chem* **1989,** *264* (35), 20998-1006.
28. Martin, B. R.; Wang, C.; Adibekian, A.; Tully, S. E.; Cravatt, B. F., Global profiling of dynamic protein palmitoylation. *Nat Methods* **2011,** *9* (1), 84-9.

29. Wan, L.; Kang, Y., Pleiotropic roles of AEG-1/MTDH/LYRIC in breast cancer. *Adv Cancer Res* **2013,** *120*, 113-34.
30. Blanc, M.; David, F.; Abrami, L.; Migliozzi, D.; Armand, F.; B¸rgi, J.; van der Goot, F., *SwissPalm: Protein Palmitoylation database*.
, 2015; Vol. 4.
31. Schlesinger, M. J.; Magee, A. I.; Schmidt, M. F., Fatty acid acylation of proteins in cultured cells. *J Biol Chem* **1980,** *255* (21), 10021-4.
32. Tsai, F. D.; Wynne, J. P.; Ahearn, I. M.; Philips, M. R., Metabolic labeling of Ras with tritiated palmitate to monitor palmitoylation and depalmitoylation. *Methods Mol Biol* **2014,** *1120*, 33-41.
33. Hang, H. C.; Geutjes, E. J.; Grotenbreg, G.; Pollington, A. M.; Bijlmakers, M. J.; Ploegh, H. L., Chemical probes for the rapid detection of Fatty-acylated proteins in Mammalian cells. *J Am Chem Soc* **2007,** *129* (10), 2744-5.
34. Martin, B. R.; Cravatt, B. F., Large-scale profiling of protein palmitoylation in mammalian cells. *Nat Methods* **2009,** *6* (2), 135-8.
35. Drisdel, R. C.; Green, W. N., Labeling and quantifying sites of protein palmitoylation. *Biotechniques* **2004,** *36* (2), 276-85.
36. Kang, R.; Wan, J.; Arstikaitis, P.; Takahashi, H.; Huang, K.; Bailey, A. O.; Thompson, J. X.; Roth, A. F.; Drisdel, R. C.; Mastro, R.; Green, W. N.; Yates, J. R., 3rd; Davis, N. G.; El-Husseini, A., Neural palmitoyl-proteomics reveals dynamic synaptic palmitoylation. *Nature* **2008,** *456* (7224), 904-9.
37. Wan, J.; Roth, A. F.; Bailey, A. O.; Davis, N. G., Palmitoylated proteins: purification and identification. *Nat Protoc* **2007,** *2* (7), 1573-84.
38. Forrester, M. T.; Hess, D. T.; Thompson, J. W.; Hultman, R.; Moseley, M. A.; Stamler, J. S.; Casey, P. J., Site-specific analysis of protein S-acylation by resin-assisted capture. *J Lipid Res* **2011,** *52* (2), 393-8.
39. Hernandez, J. L.; Majmudar, J. D.; Martin, B. R., Profiling and inhibiting reversible palmitoylation. *Curr Opin Chem Biol* **2013,** *17* (1), 20-6.
40. Charron, G.; Zhang, M. M.; Yount, J. S.; Wilson, J.; Raghavan, A. S.; Shamir, E.; Hang, H. C., Robust fluorescent detection of protein fatty-acylation with chemical reporters. *J Am Chem Soc* **2009,** *131* (13), 4967-75.
41. Martin, B. R., Nonradioactive analysis of dynamic protein palmitoylation. *Curr Protoc Protein Sci* **2013,** *73*, Unit 14 15.
42. Yount, J. S.; Moltedo, B.; Yang, Y. Y.; Charron, G.; Moran, T. M.; Lopez, C. B.; Hang, H. C., Palmitoylome profiling reveals S-palmitoylation-dependent antiviral activity of IFITM3. *Nat Chem Biol* **2010,** *6* (8), 610-4.
43. Hernandez, J. L.; Davda, D.; Majmudar, J. D.; Won, S. J.; Prakash, A.; Choi, A. I.; Martin, B. R., Correlated S-palmitoylation profiling of Snail-induced epithelial to mesenchymal transition. *Mol Biosyst* **2016,** *12* (6), 1799-808.
44. Foe, I. T.; Child, M. A.; Majmudar, J. D.; Krishnamurthy, S.; van der Linden, W. A.; Ward, G. E.; Martin, B. R.; Bogyo, M., Global Analysis of Palmitoylated Proteins in Toxoplasma gondii. *Cell Host Microbe* **2015,** *18* (4), 501-11.
45. Jones, M. L.; Collins, M. O.; Goulding, D.; Choudhary, J. S.; Rayner, J. C., Analysis of protein palmitoylation reveals a pervasive role in Plasmodium development and pathogenesis. *Cell Host Microbe* **2012,** *12* (2), 246-58.

46. Zhang, M. M.; Tsou, L. K.; Charron, G.; Raghavan, A. S.; Hang, H. C., Tandem fluorescence imaging of dynamic S-acylation and protein turnover. *Proc Natl Acad Sci U S A* **2010,** *107* (19), 8627-32.
47. Thiele, C.; Papan, C.; Hoelper, D.; Kusserow, K.; Gaebler, A.; Schoene, M.; Piotrowitz, K.; Lohmann, D.; Spandl, J.; Stevanovic, A.; Shevchenko, A.; Kuerschner, L., Tracing fatty acid metabolism by click chemistry. *ACS Chem Biol* **2012,** *7* (12), 2004-11.
48. Chen, S.; Zhu, B.; Yin, C.; Liu, W.; Han, C.; Chen, B.; Liu, T.; Li, X.; Chen, X.; Li, C.; Hu, L.; Zhou, J.; Xu, Z. X.; Gao, X.; Wu, X.; Goding, C. R.; Cui, R., Palmitoylation-dependent activation of MC1R prevents melanomagenesis. *Nature* **2017,** *549* (7672), 399-403.
49. Davda, D.; El Azzouny, M. A.; Tom, C. T.; Hernandez, J. L.; Majmudar, J. D.; Kennedy, R. T.; Martin, B. R., Profiling targets of the irreversible palmitoylation inhibitor 2-bromopalmitate. *ACS Chem Biol* **2013,** *8* (9), 1912-7.
50. Xu, S.; Nam, S. M.; Kim, J. H.; Das, R.; Choi, S. K.; Nguyen, T. T.; Quan, X.; Choi, S. J.; Chung, C. H.; Lee, E. Y.; Lee, I. K.; Wiederkehr, A.; Wollheim, C. B.; Cha, S. K.; Park, K. S., Palmitate induces ER calcium depletion and apoptosis in mouse podocytes subsequent to mitochondrial oxidative stress. *Cell Death Dis* **2015,** *6*, e1976.
51. Wang, W.; Runkle, K. B.; Terkowski, S. M.; Ekaireb, R. I.; Witze, E. S., Protein Depalmitoylation Is Induced by Wnt5a and Promotes Polarized Cell Behavior. *J Biol Chem* **2015,** *290* (25), 15707-16.
52. Camp, L. A.; Hofmann, S. L., Purification and properties of a palmitoyl-protein thioesterase that cleaves palmitate from H-Ras. *J Biol Chem* **1993,** *268* (30), 22566-74.
53. Duncan, J. A.; Gilman, A. G., A Cytoplasmic Acyl-Protein Thioesterase That Removes Palmitate from G Protein α Subunits and p21RAS. *Journal of Biological Chemistry* **1998,** *273* (25), 15830-15837.
54. Verkruyse, L. A.; Hofmann, S. L., Lysosomal targeting of palmitoyl-protein thioesterase. *J Biol Chem* **1996,** *271* (26), 15831-6.
55. Vesa, J.; Hellsten, E.; Verkruyse, L. A.; Camp, L. A.; Rapola, J.; Santavuori, P.; Hofmann, S. L.; Peltonen, L., Mutations in the palmitoyl protein thioesterase gene causing infantile neuronal ceroid lipofuscinosis. *Nature* **1995,** *376* (6541), 584-7.
56. Greaves, J.; Lemonidis, K.; Gorleku, O. A.; Cruchaga, C.; Grefen, C.; Chamberlain, L. H., Palmitoylation-induced aggregation of cysteine-string protein mutants that cause neuronal ceroid lipofuscinosis. *J Biol Chem* **2012,** *287* (44), 37330-9.
57. Henderson, M. X.; Wirak, G. S.; Zhang, Y. Q.; Dai, F.; Ginsberg, S. D.; Dolzhanskaya, N.; Staropoli, J. F.; Nijssen, P. C.; Lam, T. T.; Roth, A. F.; Davis, N. G.; Dawson, G.; Velinov, M.; Chandra, S. S., Neuronal ceroid lipofuscinosis with DNAJC5/CSPalpha mutation has PPT1 pathology and exhibit aberrant protein palmitoylation. *Acta Neuropathol* **2016,** *131* (4), 621-37.
58. Sugimoto, H.; Hayashi, H.; Yamashita, S., Purification, cDNA cloning, and regulation of lysophospholipase from rat liver. *J Biol Chem* **1996,** *271* (13), 7705-11.
59. Hedberg, C.; Dekker, F. J.; Rusch, M.; Renner, S.; Wetzel, S.; Vartak, N.; Gerding-Reimers, C.; Bon, R. S.; Bastiaens, P. I.; Waldmann, H., Development of highly potent inhibitors of the Ras-targeting human acyl protein thioesterases based on substrate similarity design. *Angew Chem Int Ed Engl* **2011,** *50* (42), 9832-7.

60. Kong, E.; Peng, S.; Chandra, G.; Sarkar, C.; Zhang, Z.; Bagh, M. B.; Mukherjee, A. B., Dynamic palmitoylation links cytosol-membrane shuttling of acyl-protein thioesterase-1 and acyl-protein thioesterase-2 with that of proto-oncogene H-ras product and growth-associated protein-43. *J Biol Chem* **2013,** *288* (13), 9112-25.
61. Dekker, F. J.; Rocks, O.; Vartak, N.; Menninger, S.; Hedberg, C.; Balamurugan, R.; Wetzel, S.; Renner, S.; Gerauer, M.; Scholermann, B.; Rusch, M.; Kramer, J. W.; Rauh, D.; Coates, G. W.; Brunsveld, L.; Bastiaens, P. I.; Waldmann, H., Small-molecule inhibition of APT1 affects Ras localization and signaling. *Nat Chem Biol* **2010,** *6* (6), 449-56.
62. Yeh, D. C.; Duncan, J. A.; Yamashita, S.; Michel, T., Depalmitoylation of endothelial nitric-oxide synthase by acyl-protein thioesterase 1 is potentiated by Ca(2+)-calmodulin. *J Biol Chem* **1999,** *274* (46), 33148-54.
63. Siegel, G.; Obernosterer, G.; Fiore, R.; Oehmen, M.; Bicker, S.; Christensen, M.; Khudayberdiev, S.; Leuschner, P. F.; Busch, C. J.; Kane, C.; Hubel, K.; Dekker, F.; Hedberg, C.; Rengarajan, B.; Drepper, C.; Waldmann, H.; Kauppinen, S.; Greenberg, M. E.; Draguhn, A.; Rehmsmeier, M.; Martinez, J.; Schratt, G. M., A functional screen implicates microRNA-138-dependent regulation of the depalmitoylation enzyme APT1 in dendritic spine morphogenesis. *Nat Cell Biol* **2009,** *11* (6), 705-16.
64. Toyoda, T.; Sugimoto, H.; Yamashita, S., Sequence, expression in Escherichia coli, and characterization of lysophospholipase II. *Biochim Biophys Acta* **1999,** *1437* (2), 182-93.
65. Manna, J. D.; Wepy, J. A.; Hsu, K. L.; Chang, J. W.; Cravatt, B. F.; Marnett, L. J., Identification of the major prostaglandin glycerol ester hydrolase in human cancer cells. *J Biol Chem* **2014,** *289* (49), 33741-53.
66. Vartak, N.; Papke, B.; Grecco, H. E.; Rossmannek, L.; Waldmann, H.; Hedberg, C.; Bastiaens, P. I., The autodepalmitoylating activity of APT maintains the spatial organization of palmitoylated membrane proteins. *Biophys J* **2014,** *106* (1), 93-105.
67. Adachi, N.; Hess, D. T.; McLaughlin, P.; Stamler, J. S., S-Palmitoylation of a Novel Site in the beta2-Adrenergic Receptor Associated with a Novel Intracellular Itinerary. *J Biol Chem* **2016,** *291* (38), 20232-46.
68. Yang, W.; Di Vizio, D.; Kirchner, M.; Steen, H.; Freeman, M. R., Proteome scale characterization of human S-acylated proteins in lipid raft-enriched and non-raft membranes. *Mol Cell Proteomics* **2010,** *9* (1), 54-70.
69. Bachovchin, D. A.; Ji, T.; Li, W.; Simon, G. M.; Blankman, J. L.; Adibekian, A.; Hoover, H.; Niessen, S.; Cravatt, B. F., Superfamily-wide portrait of serine hydrolase inhibition achieved by library-versus-library screening. *Proc Natl Acad Sci U S A* **2010,** *107* (49), 20941-6.
70. Abrami, L.; Dallavilla, T.; Sandoz, P. A.; Demir, M.; Kunz, B.; Savoglidis, G.; Hatzimanikatis, V.; van der Goot, F. G., Identification and dynamics of the human ZDHHC16-ZDHHC6 palmitoylation cascade. *Elife* **2017,** *6*.
71. Deck, P.; Pendzialek, D.; Biel, M.; Wagner, M.; Popkirova, B.; Ludolph, B.; Kragol, G.; Kuhlmann, J.; Giannis, A.; Waldmann, H., Development and biological evaluation of acyl protein thioesterase 1 (APT1) inhibitors. *Angew Chem Int Ed Engl* **2005,** *44* (31), 4975-80.
72. Xu, J.; Hedberg, C.; Dekker, F. J.; Li, Q.; Haigis, K. M.; Hwang, E.; Waldmann, H.; Shannon, K., Inhibiting the palmitoylation/depalmitoylation cycle selectively reduces

the growth of hematopoietic cells expressing oncogenic Nras. *Blood* **2012,** *119* (4), 1032-5.
73. Grecco, H. E.; Schmick, M.; Bastiaens, P. I., Signaling from the living plasma membrane. *Cell* **2011,** *144* (6), 897-909.
74. Yokoi, N.; Fukata, Y.; Sekiya, A.; Murakami, T.; Kobayashi, K.; Fukata, M., Identification of PSD-95 Depalmitoylating Enzymes. *J Neurosci* **2016,** *36* (24), 6431-44.
75. Hernandez, J. L.; Davda, D.; Cheung See Kit, M.; Majmudar, J. D.; Won, S. J.; Gang, M.; Pasupuleti, S. C.; Choi, A. I.; Bartkowiak, C. M.; Martin, B. R., APT2 Inhibition Restores Scribble Localization and S-Palmitoylation in Snail-Transformed Cells. *Cell Chem Biol* **2017,** *24* (1), 87-97.
76. Akimzhanov, A. M.; Boehning, D., Rapid and transient palmitoylation of the tyrosine kinase Lck mediates Fas signaling. *Proc Natl Acad Sci U S A* **2015,** *112* (38), 11876-80.
77. Jia, L.; Chisari, M.; Maktabi, M. H.; Sobieski, C.; Zhou, H.; Konopko, A. M.; Martin, B. R.; Mennerick, S. J.; Blumer, K. J., A mechanism regulating G protein-coupled receptor signaling that requires cycles of protein palmitoylation and depalmitoylation. *J Biol Chem* **2014,** *289* (9), 6249-57.
78. Berg, V.; Rusch, M.; Vartak, N.; Jungst, C.; Schauss, A.; Waldmann, H.; Hedberg, C.; Pallasch, C. P.; Bastiaens, P. I.; Hallek, M.; Wendtner, C. M.; Frenzel, L. P., miRs-138 and -424 control palmitoylation-dependent CD95-mediated cell death by targeting acyl protein thioesterases 1 and 2 in CLL. *Blood* **2015,** *125* (19), 2948-57.
79. Lin, D. T.; Conibear, E., ABHD17 proteins are novel protein depalmitoylases that regulate N-Ras palmitate turnover and subcellular localization. *Elife* **2015,** *4*, e11306.
80. Vujic, I.; Sanlorenzo, M.; Esteve-Puig, R.; Vujic, M.; Kwong, A.; Tsumura, A.; Murphy, R.; Moy, A.; Posch, C.; Monshi, B.; Rappersberger, K.; Ortiz-Urda, S., Acyl protein thioesterase 1 and 2 (APT-1, APT-2) inhibitors palmostatin B, ML348 and ML349 have different effects on NRAS mutant melanoma cells. *Oncotarget* **2016,** *7* (6), 7297-306.
81. Adibekian, A.; Martin, B. R.; Chang, J. W.; Hsu, K. L.; Tsuboi, K.; Bachovchin, D. A.; Speers, A. E.; Brown, S. J.; Spicer, T.; Fernandez-Vega, V.; Ferguson, J.; Cravatt, B. F.; Hodder, P.; Rosen, H., Characterization of a Selective, Reversible Inhibitor of Lysophospholipase 2 (LYPLA2). In *Probe Reports from the NIH Molecular Libraries Program*, Bethesda (MD), 2010.
82. Adibekian, A.; Martin, B. R.; Chang, J. W.; Hsu, K. L.; Tsuboi, K.; Bachovchin, D. A.; Speers, A. E.; Brown, S. J.; Spicer, T.; Fernandez-Vega, V.; Ferguson, J.; Cravatt, B. F.; Hodder, P.; Rosen, H., Characterization of a Selective, Reversible Inhibitor of Lysophospholipase 1 (LYPLA1). In *Probe Reports from the NIH Molecular Libraries Program*, National Center for Biotechnology Information (US): Bethesda (MD), 2010.
83. Adibekian, A.; Martin, B. R.; Chang, J. W.; Hsu, K. L.; Tsuboi, K.; Bachovchin, D. A.; Speers, A. E.; Brown, S. J.; Spicer, T.; Fernandez-Vega, V.; Ferguson, J.; Hodder, P. S.; Rosen, H.; Cravatt, B. F., Confirming target engagement for reversible inhibitors in vivo by kinetically tuned activity-based probes. *J Am Chem Soc* **2012,** *134* (25), 10345-8.
84. Won, S. J.; Eschweiler, J. D.; Majmudar, J. D.; Chong, F. S.; Hwang, S. Y.; Ruotolo, B. T.; Martin, B. R., Affinity-Based Selectivity Profiling of an In-Class Selective

Competitive Inhibitor of Acyl Protein Thioesterase 2. *ACS Med Chem Lett* **2017,** *8* (2), 215-220.
85. Adibekian, A.; Martin, B. R.; Speers, A. E.; Brown, S. J.; Spicer, T.; Fernandez-Vega, V.; Ferguson, J.; Cravatt, B. F.; Hodder, P.; Rosen, H., Optimization and characterization of a triazole urea dual inhibitor for lysophospholipase 1 (LYPLA1) and lysophospholipase 2 (LYPLA2). In *Probe Reports from the NIH Molecular Libraries Program*, Bethesda (MD), 2010.
86. Adibekian, A.; Martin, B. R.; Wang, C.; Hsu, K. L.; Bachovchin, D. A.; Niessen, S.; Hoover, H.; Cravatt, B. F., Click-generated triazole ureas as ultrapotent in vivo-active serine hydrolase inhibitors. *Nat Chem Biol* **2011,** *7* (7), 469-78.
87. Cognetta, A. B., 3rd; Niphakis, M. J.; Lee, H. C.; Martini, M. L.; Hulce, J. J.; Cravatt, B. F., Selective N-Hydroxyhydantoin Carbamate Inhibitors of Mammalian Serine Hydrolases. *Chem Biol* **2015,** *22* (7), 928-37.
88. Hulce, J. J.; Joslyn, C.; Speers, A. E.; Brown, S. J.; Spicer, T.; Fernandez-Vega, V.; Ferguson, J.; Cravatt, B. F.; Hodder, P.; Rosen, H., An in Vivo Active Carbamate-based Dual Inhibitor of Lysophospholipase 1 (LYPLA1) and Lysophospholipase 2 (LYPLA2). In *Probe Reports from the NIH Molecular Libraries Program*, Bethesda (MD), 2010.
89. Bilder, D.; Perrimon, N., Localization of apical epithelial determinants by the basolateral PDZ protein Scribble. *Nature* **2000,** *403* (6770), 676-80.
90. Dow, L. E.; Brumby, A. M.; Muratore, R.; Coombe, M. L.; Sedelies, K. A.; Trapani, J. A.; Russell, S. M.; Richardson, H. E.; Humbert, P. O., hScrib is a functional homologue of the Drosophila tumour suppressor Scribble. *Oncogene* **2003,** *22* (58), 9225-30.
91. Feigin, M. E.; Akshinthala, S. D.; Araki, K.; Rosenberg, A. Z.; Muthuswamy, L. B.; Martin, B.; Lehmann, B. D.; Berman, H. K.; Pietenpol, J. A.; Cardiff, R. D.; Muthuswamy, S. K., Mislocalization of the cell polarity protein scribble promotes mammary tumorigenesis and is associated with basal breast cancer. *Cancer research* **2014,** *74* (11), 3180-94.
92. Nakagawa, S.; Huibregtse, J. M., Human scribble (Vartul) is targeted for ubiquitin-mediated degradation by the high-risk papillomavirus E6 proteins and the E6AP ubiquitin-protein ligase. *Mol Cell Biol* **2000,** *20* (21), 8244-53.
93. Nakagawa, S.; Yano, T.; Nakagawa, K.; Takizawa, S.; Suzuki, Y.; Yasugi, T.; Huibregtse, J. M.; Taketani, Y., Analysis of the expression and localisation of a LAP protein, human scribble, in the normal and neoplastic epithelium of uterine cervix. *Br J Cancer* **2004,** *90* (1), 194-9.
94. Gardiol, D.; Zacchi, A.; Petrera, F.; Stanta, G.; Banks, L., Human discs large and scrib are localized at the same regions in colon mucosa and changes in their expression patterns are correlated with loss of tissue architecture during malignant progression. *Int J Cancer* **2006,** *119* (6), 1285-90.
95. Pearson, H. B.; Perez-Mancera, P. A.; Dow, L. E.; Ryan, A.; Tennstedt, P.; Bogani, D.; Elsum, I.; Greenfield, A.; Tuveson, D. A.; Simon, R.; Humbert, P. O., SCRIB expression is deregulated in human prostate cancer, and its deficiency in mice promotes prostate neoplasia. *Journal of Clinical Investigation* **2011,** *121* (11), 4257-4267.

96. Zhan, L.; Rosenberg, A.; Bergami, K. C.; Yu, M.; Xuan, Z.; Jaffe, A. B.; Allred, C.; Muthuswamy, S. K., Deregulation of scribble promotes mammary tumorigenesis and reveals a role for cell polarity in carcinoma. *Cell* **2008,** *135* (5), 865-78.
97. Vaira, V.; Faversani, A.; Dohi, T.; Maggioni, M.; Nosotti, M.; Tosi, D.; Altieri, D. C.; Bosari, S., Aberrant overexpression of the cell polarity module scribble in human cancer. *Am J Pathol* **2011,** *178* (6), 2478-83.
98. Cordenonsi, M.; Zanconato, F.; Azzolin, L.; Forcato, M.; Rosato, A.; Frasson, C.; Inui, M.; Montagner, M.; Parenti, A. R.; Poletti, A.; Daidone, M. G.; Dupont, S.; Basso, G.; Bicciato, S.; Piccolo, S., The Hippo transducer TAZ confers cancer stem cell-related traits on breast cancer cells. *Cell* **2011,** *147* (4), 759-72.
99. Elsum, I. A.; Humbert, P. O., Localization, not important in all tumor-suppressing properties: a lesson learnt from scribble. *Cells Tissues Organs* **2013,** *198* (1), 1-11.
100. Davda, D.; Martin, B. R., Acyl protein thioesterase inhibitors as probes of dynamic S-palmitoylation. *Medchemcomm* **2014,** *5* (3), 268-276.
101. Satou, M.; Nishi, Y.; Yoh, J.; Hattori, Y.; Sugimoto, H., Identification and characterization of acyl-protein thioesterase 1/lysophospholipase I as a ghrelin deacylation/lysophospholipid hydrolyzing enzyme in fetal bovine serum and conditioned medium. *Endocrinology* **2010,** *151* (10), 4765-75.
102. Kathayat, R. S.; Elvira, P. D.; Dickinson, B. C., A fluorescent probe for cysteine depalmitoylation reveals dynamic APT signaling. *Nat Chem Biol* **2017,** *13* (2), 150-152.
103. Won, S. J.; Davda, D.; Labby, K. J.; Hwang, S. Y.; Pricer, R.; Majmudar, J. D.; Armacost, K. A.; Rodriguez, L. A.; Rodriguez, C. L.; Chong, F. S.; Torossian, K. A.; Palakurthi, J.; Hur, E. S.; Meagher, J. L.; Brooks, C. L., 3rd; Stuckey, J. A.; Martin, B. R., Molecular Mechanism for Isoform-Selective Inhibition of Acyl Protein Thioesterases 1 and 2 (APT1 and APT2). *ACS Chem Biol* **2016,** *11* (12), 3374-3382.
104. Devedjiev, Y.; Dauter, Z.; Kuznetsov, S. R.; Jones, T. L.; Derewenda, Z. S., Crystal structure of the human acyl protein thioesterase I from a single X-ray data set to 1.5 A. *Structure* **2000,** *8* (11), 1137-46.
105. Ahearn, I. M.; Tsai, F. D.; Court, H.; Zhou, M.; Jennings, B. C.; Ahmed, M.; Fehrenbacher, N.; Linder, M. E.; Philips, M. R., FKBP12 binds to acylated H-ras and promotes depalmitoylation. *Mol Cell* **2011,** *41* (2), 173-85.
106. Tortosa, E.; Adolfs, Y.; Fukata, M.; Pasterkamp, R. J.; Kapitein, L. C.; Hoogenraad, C. C., Dynamic Palmitoylation Targets MAP6 to the Axon to Promote Microtubule Stabilization during Neuronal Polarization. *Neuron* **2017,** *94* (4), 809-825 e7.
107. van der Weyden, L.; Arends, M. J.; Campbell, A. D.; Bald, T.; Wardle-Jones, H.; Griggs, N.; Velasco-Herrera, M. D.; Tuting, T.; Sansom, O. J.; Karp, N. A.; Clare, S.; Gleeson, D.; Ryder, E.; Galli, A.; Tuck, E.; Cambridge, E. L.; Voet, T.; Macaulay, I. C.; Wong, K.; Sanger Mouse Genetics, P.; Spiegel, S.; Speak, A. O.; Adams, D. J., Genome-wide in vivo screen identifies novel host regulators of metastatic colonization. *Nature* **2017,** *541* (7636), 233-236.
108. Savinainen, J. R.; Patel, J. Z.; Parkkari, T.; Navia-Paldanius, D.; Marjamaa, J. J.; Laitinen, T.; Nevalainen, T.; Laitinen, J. T., Biochemical and pharmacological characterization of the human lymphocyte antigen B-associated transcript 5 (BAT5/ABHD16A). *PLoS One* **2014,** *9* (10), e109869.

109. Yuan, B. Z.; Miller, M. J.; Keck, C. L.; Zimonjic, D. B.; Thorgeirsson, S. S.; Popescu, N. C., Cloning, characterization, and chromosomal localization of a gene frequently deleted in human liver cancer (DLC-1) homologous to rat RhoGAP. *Cancer Res* **1998,** *58* (10), 2196-9.
110. Duncan, J. A.; Gilman, A. G., A cytoplasmic acyl-protein thioesterase that removes palmitate from G protein alpha subunits and p21(RAS). *J Biol Chem* **1998,** *273* (25), 15830-7.
111. Duncan, J. A.; Gilman, A. G., Characterization of Saccharomyces cerevisiae acyl-protein thioesterase 1, the enzyme responsible for G protein alpha subunit deacylation in vivo. *J Biol Chem* **2002,** *277* (35), 31740-52.
112. Tomatis, V. M.; Trenchi, A.; Gomez, G. A.; Daniotti, J. L., Acyl-protein thioesterase 2 catalyzes the deacylation of peripheral membrane-associated GAP-43. *PLoS One* **2010,** *5* (11), e15045.
113. Tian, L.; McClafferty, H.; Knaus, H. G.; Ruth, P.; Shipston, M. J., Distinct acyl protein transferases and thioesterases control surface expression of calcium-activated potassium channels. *J Biol Chem* **2012,** *287* (18), 14718-25.
114. Martinez Molina, D.; Jafari, R.; Ignatushchenko, M.; Seki, T.; Larsson, E. A.; Dan, C.; Sreekumar, L.; Cao, Y.; Nordlund, P., Monitoring drug target engagement in cells and tissues using the cellular thermal shift assay. *Science* **2013,** *341* (6141), 84-7.
115. Filippova, E. V.; Weston, L. A.; Kuhn, M. L.; Geissler, B.; Gehring, A. M.; Armoush, N.; Adkins, C. T.; Minasov, G.; Dubrovska, I.; Shuvalova, L.; Winsor, J. R.; Lavis, L. D.; Satchell, K. J.; Becker, D. P.; Anderson, W. F.; Johnson, R. J., Large scale structural rearrangement of a serine hydrolase from Francisella tularensis facilitates catalysis. *J Biol Chem* **2013,** *288* (15), 10522-35.
116. Kakugawa, S.; Langton, P. F.; Zebisch, M.; Howell, S. A.; Chang, T. H.; Liu, Y.; Feizi, T.; Bineva, G.; O'Reilly, N.; Snijders, A. P.; Jones, E. Y.; Vincent, J. P., Notum deacylates Wnt proteins to suppress signalling activity. *Nature* **2015,** *519* (7542), 187-92.
117. Davis, B. M.; Richens, J. L.; O'Shea, P., Label-free critical micelle concentration determination of bacterial quorum sensing molecules. *Biophys J* **2011,** *101* (1), 245-54.
118. Thumser, A. E.; Storch, J., Characterization of a BODIPY-labeled fluorescent fatty acid analogue. Binding to fatty acid-binding proteins, intracellular localization, and metabolism. *Mol Cell Biochem* **2007,** *299* (1-2), 67-73.
119. The CCP4 suite: programs for protein crystallography. *Acta Crystallogr D Biol Crystallogr* **1994,** *50* (Pt 5), 760-3.
120. Evans, P. R., An introduction to data reduction: space-group determination, scaling and intensity statistics. *Acta Crystallogr D Biol Crystallogr* **2011,** *67* (Pt 4), 282-92.
121. Vagin, A.; Teplyakov, A., Molecular replacement with MOLREP. *Acta Crystallogr D Biol Crystallogr* **2010,** *66* (Pt 1), 22-5.
122. Long, F.; Vagin, A. A.; Young, P.; Murshudov, G. N., BALBES: a molecular-replacement pipeline. *Acta Crystallogr D Biol Crystallogr* **2008,** *64* (Pt 1), 125-32.
123. Emsley, P.; Cowtan, K., Coot: model-building tools for molecular graphics. *Acta Crystallogr D Biol Crystallogr* **2004,** *60* (Pt 12 Pt 1), 2126-32.

124. Bricogne, G.; Blanc, E.; Brandl, M.; Flensburg, C.; Keller, P.; Paciorek, W.; Roversi, P.; Shariff, A.; Smart, O.; Vonrhein, C.; Womack, T., BUSTER version 2.11.2. Global Phasing Ltd: Cambridge, UK, 2011.
125. Brooks, B. R.; Brooks, C. L., 3rd; Mackerell, A. D., Jr.; Nilsson, L.; Petrella, R. J.; Roux, B.; Won, Y.; Archontis, G.; Bartels, C.; Boresch, S.; Caflisch, A.; Caves, L.; Cui, Q.; Dinner, A. R.; Feig, M.; Fischer, S.; Gao, J.; Hodoscek, M.; Im, W.; Kuczera, K.; Lazaridis, T.; Ma, J.; Ovchinnikov, V.; Paci, E.; Pastor, R. W.; Post, C. B.; Pu, J. Z.; Schaefer, M.; Tidor, B.; Venable, R. M.; Woodcock, H. L.; Wu, X.; Yang, W.; York, D. M.; Karplus, M., CHARMM: the biomolecular simulation program. *J Comput Chem* **2009,** *30* (10), 1545-614.
126. Darden, T.; York, D.; Pedersen, L., Particle mesh Ewald: An N · log(N) method for Ewald sums in large systems. *The Journal of Chemical Physics* **1993,** *98* (12), 10089-10092.
127. Buck, M.; Bouguet-Bonnet, S.; Pastor, R. W.; MacKerell, A. D., Jr., Importance of the CMAP correction to the CHARMM22 protein force field: dynamics of hen lysozyme. In *Biophys J*, United States, 2006; Vol. 90, pp L36-8.
128. Jorgensen, W. L.; Chandrasekhar, J.; Madura, J. D.; Impey, R. W.; Klein, M. L., Comparison of simple potential functions for simulating liquid water. *The Journal of Chemical Physics* **1983,** *79* (2), 926-935.
129. Vanommeslaeghe, K.; Hatcher, E.; Acharya, C.; Kundu, S.; Zhong, S.; Shim, J.; Darian, E.; Guvench, O.; Lopes, P.; Vorobyov, I.; Mackerell, A. D., Jr., CHARMM general force field: A force field for drug-like molecules compatible with the CHARMM all-atom additive biological force fields. *J Comput Chem* **2010,** *31* (4), 671-90.
130. Vanommeslaeghe, K.; MacKerell, A. D., Jr., Automation of the CHARMM General Force Field (CGenFF) I: bond perception and atom typing. *J Chem Inf Model* **2012,** *52* (12), 3144-54.
131. Yu, W.; He, X.; Vanommeslaeghe, K.; MacKerell, A. D., Jr., Extension of the CHARMM General Force Field to sulfonyl-containing compounds and its utility in biomolecular simulations. *J Comput Chem* **2012,** *33* (31), 2451-68.
132. Vanommeslaeghe, K.; Raman, E. P.; MacKerell, A. D., Jr., Automation of the CHARMM General Force Field (CGenFF) II: assignment of bonded parameters and partial atomic charges. *J Chem Inf Model* **2012,** *52* (12), 3155-68.
133. Humphrey, W.; Dalke, A.; Schulten, K., VMD: visual molecular dynamics. *J Mol Graph* **1996,** *14* (1), 33-8, 27-8.
134. Nikolovska-Coleska, Z.; Wang, R.; Fang, X.; Pan, H.; Tomita, Y.; Li, P.; Roller, P. P.; Krajewski, K.; Saito, N. G.; Stuckey, J. A.; Wang, S., Development and optimization of a binding assay for the XIAP BIR3 domain using fluorescence polarization. *Anal Biochem* **2004,** *332* (2), 261-73.
135. Niphakis, M. J.; Cravatt, B. F., Enzyme inhibitor discovery by activity-based protein profiling. *Annu Rev Biochem* **2014,** *83*, 341-77.
136. Li, W.; Blankman, J. L.; Cravatt, B. F., A functional proteomic strategy to discover inhibitors for uncharacterized hydrolases. *J Am Chem Soc* **2007,** *129* (31), 9594-5.
137. Chang, J. W.; Cognetta, A. B., 3rd; Niphakis, M. J.; Cravatt, B. F., Proteome-wide reactivity profiling identifies diverse carbamate chemotypes tuned for serine hydrolase inhibition. *ACS Chem Biol* **2013,** *8* (7), 1590-9.

138. Bantscheff, M.; Eberhard, D.; Abraham, Y.; Bastuck, S.; Boesche, M.; Hobson, S.; Mathieson, T.; Perrin, J.; Raida, M.; Rau, C.; Reader, V.; Sweetman, G.; Bauer, A.; Bouwmeester, T.; Hopf, C.; Kruse, U.; Neubauer, G.; Ramsden, N.; Rick, J.; Kuster, B.; Drewes, G., Quantitative chemical proteomics reveals mechanisms of action of clinical ABL kinase inhibitors. *Nat Biotechnol* **2007,** *25* (9), 1035-44.
139. Winger, J. A.; Hantschel, O.; Superti-Furga, G.; Kuriyan, J., The structure of the leukemia drug imatinib bound to human quinone reductase 2 (NQO2). *BMC Struct Biol* **2009,** *9*, 7.
140. Lomenick, B.; Jung, G.; Wohlschlegel, J. A.; Huang, J., Target identification using drug affinity responsive target stability (DARTS). *Curr Protoc Chem Biol* **2011,** *3* (4), 163-180.
141. Shalem, O.; Sanjana, N. E.; Hartenian, E.; Shi, X.; Scott, D. A.; Mikkelson, T.; Heckl, D.; Ebert, B. L.; Root, D. E.; Doench, J. G.; Zhang, F., Genome-scale CRISPR-Cas9 knockout screening in human cells. *Science* **2014,** *343* (6166), 84-87.
142. Chen, B.; Zheng, B.; DeRan, M.; Jarugumilli, G. K.; Fu, J.; Brooks, Y. S.; Wu, X., ZDHHC7-mediated S-palmitoylation of Scribble regulates cell polarity. *Nat Chem Biol* **2016,** *12* (9), 686-93.
143. Hofstadler, S. A.; Sannes-Lowery, K. A., Applications of ESI-MS in drug discovery: interrogation of noncovalent complexes. *Nat Rev Drug Discov* **2006,** *5* (7), 585-95.
144. Distler, U.; Kuharev, J.; Navarro, P.; Levin, Y.; Schild, H.; Tenzer, S., Drift time-specific collision energies enable deep-coverage data-independent acquisition proteomics. *Nat Methods* **2014,** *11* (2), 167-70.
145. Huber, K. V.; Salah, E.; Radic, B.; Gridling, M.; Elkins, J. M.; Stukalov, A.; Jemth, A. S.; Gokturk, C.; Sanjiv, K.; Stromberg, K.; Pham, T.; Berglund, U. W.; Colinge, J.; Bennett, K. L.; Loizou, J. I.; Helleday, T.; Knapp, S.; Superti-Furga, G., Stereospecific targeting of MTH1 by (S)-crizotinib as an anticancer strategy. *Nature* **2014,** *508* (7495), 222-7.
146. Knezevic, C. E.; Wright, G.; Rix, L. L. R.; Kim, W.; Kuenzi, B. M.; Luo, Y.; Watters, J. M.; Koomen, J. M.; Haura, E. B.; Monteiro, A. N.; Radu, C.; Lawrence, H. R.; Rix, U., Proteome-wide Profiling of Clinical PARP Inhibitors Reveals Compound-Specific Secondary Targets. *Cell Chem Biol* **2016,** *23* (12), 1490-1503.
147. Jecklin, M. C.; Touboul, D.; Jain, R.; Toole, E. N.; Tallarico, J.; Drueckes, P.; Ramage, P.; Zenobi, R., Affinity classification of kinase inhibitors by mass spectrometric methods and validation using standard IC(50) measurements. *Anal Chem* **2009,** *81* (1), 408-19.
148. Shi, H.; Zhang, C. J.; Chen, G. Y.; Yao, S. Q., Cell-based proteome profiling of potential dasatinib targets by use of affinity-based probes. *J Am Chem Soc* **2012,** *134* (6), 3001-14.
149. Li, Z.; Wang, D.; Li, L.; Pan, S.; Na, Z.; Tan, C. Y.; Yao, S. Q., "Minimalist" cyclopropene-containing photo-cross-linkers suitable for live-cell imaging and affinity-based protein labeling. *J Am Chem Soc* **2014,** *136* (28), 9990-8.
150. Silva, J. C.; Gorenstein, M. V.; Li, G. Z.; Vissers, J. P.; Geromanos, S. J., Absolute quantification of proteins by LCMSE: a virtue of parallel MS acquisition. *Mol Cell Proteomics* **2006,** *5* (1), 144-56.

151. Zhong, Y.; Hyung, S. J.; Ruotolo, B. T., Characterizing the resolution and accuracy of a second-generation traveling-wave ion mobility separator for biomolecular ions. *Analyst* **2011,** *136* (17), 3534-41.
152. Marty, M. T.; Baldwin, A. J.; Marklund, E. G.; Hochberg, G. K.; Benesch, J. L.; Robinson, C. V., Bayesian deconvolution of mass and ion mobility spectra: from binary interactions to polydisperse ensembles. *Anal Chem* **2015,** *87* (8), 4370-6.
153. Strohalm, M.; Kavan, D.; Novak, P.; Volny, M.; Havlicek, V., mMass 3: a cross-platform software environment for precise analysis of mass spectrometric data. *Anal Chem* **2010,** *82* (11), 4648-51.
154. Won, S. J.; Cheung See Kit, M.; Martin, B. R., Protein depalmitoylases. *Crit Rev Biochem Mol Biol* **2018,** *53* (1), 83-98.
155. Gao, X.; Hannoush, R. N., A Decade of Click Chemistry in Protein Palmitoylation: Impact on Discovery and New Biology. *Cell Chem Biol* **2017**.
156. Won, S. J.; Cheung See Kit, M.; Martin, B. R., Protein depalmitoylases. *Crit. Rev. Biochem. Mol. Biol.* **2018,** *53* (1), 83-98.
157. Zhang, J.; Huang, Y.; Chen, J.; Zhu, H.; Whiteheart, S. W., Dynamic Cycling of t-SNARE Acylation Regulates Platelet Exocytosis. *J. Biol. Chem.* **2018**.
158. Pedro, M. P.; Vilcaes, A. A.; Tomatis, V. M.; Oliveira, R. G.; Gomez, G. A.; Daniotti, J. L., 2-Bromopalmitate reduces protein deacylation by inhibition of acyl-protein thioesterase enzymatic activities. *PLoS One* **2013,** *8* (10), e75232.
159. Wang, T.; Yu, H.; Hughes, N. W.; Liu, B.; Kendirli, A.; Klein, K.; Chen, W. W.; Lander, E. S.; Sabatini, D. M., Gene Essentiality Profiling Reveals Gene Networks and Synthetic Lethal Interactions with Oncogenic Ras. *Cell* **2017,** *168* (5), 890-903.e15.
160. Stypulkowski, E.; Asangani, I. A.; Witze, E. S., The depalmitoylase APT1 directs the asymmetric partitioning of Notch and Wnt signaling during cell division. *Sci Signal* **2018,** *11* (511).
161. Xu, H.; Majmudar, J. D.; Davda, D.; Ghanakota, P.; Kim, K. H.; Carlson, H. A.; Showalter, H. D.; Martin, B. R.; Amidon, G. L., Substrate-Competitive Activity-Based Profiling of Ester Prodrug Activating Enzymes. *Mol. Pharmaceutics* **2015,** *12* (9), 3399-407.
162. McAlister, G. C.; Nusinow, D. P.; Jedrychowski, M. P.; Wuhr, M.; Huttlin, E. L.; Erickson, B. K.; Rad, R.; Haas, W.; Gygi, S. P., MultiNotch MS3 enables accurate, sensitive, and multiplexed detection of differential expression across cancer cell line proteomes. *Anal Chem* **2014,** *86* (14), 7150-8.
163. de Hoon, M. J.; Imoto, S.; Nolan, J.; Miyano, S., Open source clustering software. *Bioinformatics (Oxford, England)* **2004,** *20* (9), 1453-4.
164. Kathayat, R. S.; Cao, Y.; Elvira, P. D.; Sandoz, P. A.; Zaballa, M. E.; Springer, M. Z.; Drake, L. E.; Macleod, K. F.; van der Goot, F. G.; Dickinson, B. C., Active and dynamic mitochondrial S-depalmitoylation revealed by targeted fluorescent probes. *Nat Commun* **2018,** *9* (1), 334.
165. Gao, J.; Aksoy, B. A.; Dogrusoz, U.; Dresdner, G.; Gross, B.; Sumer, S. O.; Sun, Y.; Jacobsen, A.; Sinha, R.; Larsson, E.; Cerami, E.; Sander, C.; Schultz, N., Integrative analysis of complex cancer genomics and clinical profiles using the cBioPortal. *Sci Signal* **2013,** *6* (269), pl1.

166. Rana, M. S.; Kumar, P.; Lee, C. J.; Verardi, R.; Rajashankar, K. R.; Banerjee, A., Fatty acyl recognition and transfer by an integral membrane S-acyltransferase. *Science* **2018,** *359* (6372).
167. Han, Q.; Pabba, P. K.; Barbosa, J.; Mabon, R.; Healy, J. P.; Gardyan, M. W.; Terranova, K. M.; Brommage, R.; Thompson, A. Y.; Schmidt, J. M.; Wilson, A. G.; Xu, X.; Tarver, J. E., Jr.; Carson, K. G., 4H-Thieno[3,2-c]chromene based inhibitors of Notum Pectinacetylesterase. *Bioorg Med Chem Lett* **2016,** *26* (4), 1184-7.